UNIVERSITÀ DEGLI STUDI DI TRIESTE

XXIII CICLO
DEL DOTTORATO DI RICERCA IN
FISICA

Measurements of the transverse momentum dependent azimuthal asymmetries in SIDIS at COMPASS

Settore scientifico-disciplinare
FISICA NUCLEARE E SUBNUCLEARE (FIS/04)

Dottorando
Giulio Sbrizzai

Responsabile Dottorato di Ricerca
prof. Paolo Camerini

Relatore
prof.ssa Anna Martin, Università Degli Studi di Trieste

Tutore
prof.ssa Anna Martin, Università Degli Studi di Trieste

ANNO ACCADEMICO 2009/2010

Contents

Chapter 1

Introduction

The role of the quark intrinsic transverse momentum and spin in the description of the structure of the nucleon has become a topic of great interest in hadron physics. In particular it is now well established that they are fundamental in explaining the azimuthal asymmetries observed in the high-energy hadronic unpolarized and polarized reactions. The role of the intrinsic transverse momentum in the description of the structure of the nucleon has become crucial in explaining the azimuthal asymmetries observed in the high-energy hadronic unpolarized and polarized reactions. Many of them have been measured in the Drell-Yan processes, in semi-inclusive deeply inelastic scattering (SIDIS) and in correlated meson-pair production in unpolarized e^+e^- collisions. Within the framework of the so-called transverse momentum dependent (TMD) QCD approach a new class of leading-twist (un)polarized partonic distribution and fragmentation functions are introduced which play a fundamental role in the explanations of these phenomena. The TMD distributions are intimately related to several topics of increasing interest in hadronic physics like the parton orbital motion and angular momentum inside hadrons, the study of hadron structure in the impact parameter space or the nucleon generalized parton distributions and deeply virtual Compton scattering.

Of particular interest is the study of these effects in SIDIS off polarised and unpolarised targets at a small-intermediate energy scale, i.e. at transverse momenta of the observed hadrons of a few GeV at most. At this scale the produced hadron keeps memory of the intrinsic parton motion inside the target nucleon, and the generated asymmetries in the distribution of the azimuthal angle of produced hadrons around the direction of the virtual photon can be ascribed both to the TMD quark distribution functions and to possible higher-twist effects induced by the quark-gluon correlators. Also a fundamental QCD prediction links the TMD distributions which describe the correlation between the intrinsic transverse momentum of the quark and the transverse spin, as measured from SIDIS experiments with the corresponding ones measured in DY experiments.

The study of the amplitudes of the different azimuthal modulations predicted by the SIDIS cross section, extracted by the HERMES, COMPASS and CLAS experiments allows to quantify the contributions coming from the different effects and to add important pieces of information for the understanding of the internal structure of the nucleon.

This thesis is focused on the measurement of the hadron azimuthal asymmetries produced in the unpolarized and longitudinally polarized SIDIS in the COMPASS experiment. These results are the first ones of this kind extracted from the COMPASS data and allow to study the kinematical behaviour of the azimuthal asymmetries in the unique kinematical range accessed by the COMPASS experiment.

The thesis is organised as follows: chapter 2 is devoted to the present description of the nucleon structure and of the SIDIS process. In chapter 3 the experimental apparatus of the COMPASS experiment is presented. The data reconstruction and simulation are described in chapter 4. The measurement of the azimuthal asymmetries on the unpolarized deuteron target is described in chapter 5 and the results are presented and discussed in chapter 6, where also the comparison with the theoretical predictions and the results obtained from other experiments is presented. In chapter 7 the measurement of the azimuthal asymmetries on the longitudinally polarized deuteron target is described and the results are presented and discussed at the end of this chapter.

Chapter 2

Semi Inclusive Deep Inelastic Scattering

In Semi Inclusive Deep Inelastic Scattering (SIDIS)

$$\boldsymbol{l}(l) + \boldsymbol{N}(P) \rightarrow \boldsymbol{l}'(l') + \boldsymbol{h}(P_h) + \boldsymbol{X}(P_X) \tag{2.1}$$

a high energy lepton $\boldsymbol{l}$ scatters off the target nucleon $\boldsymbol{N}$ probing its inner structure. At least the scattered lepton $\boldsymbol{l}'$ and one hadron $\boldsymbol{h}$ are detected in the final states. The 4-vectors characterizing each particle are shown in parenthesis and $q = l - l'$ is the 4-momentum of the exchanged virtual photon and $Q^2 = -q^2$ its virtuality. The Bjorken scaling variable $x = Q^2/(2P \cdot q)$ can be identified with the longitudinal momentum fraction carried by the elementary constituent in the frame where the nucleon $\boldsymbol{N}$ has infinite momentum. The so called inelasticity $y = (P \cdot q)/(P \cdot k)$ calculated in the Laboratory System is the fraction of energy lost by the lepton. $W^2 = (P_X + P_h)^2 = (P + q)^2$ is the invariant mass of the hadronic final state $\boldsymbol{h} + \boldsymbol{X}$ and $z = (P \cdot P_h)/(P \cdot q)$ is the fraction of the available energy carried by the hadron, calculated in the Laboratory System. In the DIS regime ($Q^2 > 1$ GeV) the resolution of the exchanged photon is high enough to allow probing the single constituents of the nucleon and the time scale which characterizes the hard interaction is small enough that the constituents can be considered free from the binding nuclear force. In such a case, by detecting the products of the reaction, one can build a sort of instantaneous picture of the nucleon. In the Quark Parton Model the elementary constituent of the nucleon have been identified with the quarks binded together by the strong interaction described by the theory of the Quantum Chromo Dynamics (QCD) [1].

The kinematical variables are usually calculated in the "Gamma Nucleon System" [2] (GNS) which has the XZ plane defined by the lepton scattering plane and the directions of the virtual photon and of the target nucleon are parallel. The Z axis is defined by the photon direction, as shown in fig 2.1, and the Y axis is defined to have a right handed orthogonal system. The azimuthal angles of the final state hadrons ϕ_h and of the nucleon target polarization ϕ_S around the virtual photon direction are defined with respect to the scattering plane, as illustrated in fig 2.1.

Taking into account the helicity of the incoming lepton and the polarization of

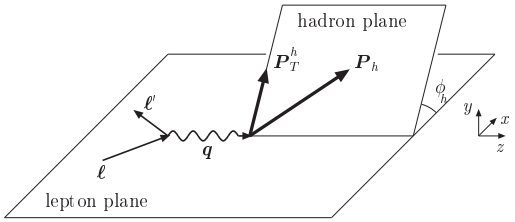

Figure 2.1: Definition of the Gamma Nucleon System (GNS).

the target nucleon the differential cross section can be written as [3, 4]

$$\frac{d\sigma}{dxdydzd\phi_h d\phi_S dP_T^{h^2}} = \frac{\pi\alpha^2 y}{Q^4} L_{\mu\nu} 2MW^{\mu\nu}(P, q, P_h, S). \tag{2.2}$$

$L_{\mu\nu}$ is the leptonic tensor, given by QED,

$$L_{\mu\nu} = 2 \cdot (l_\mu l'_\nu + l'_\mu l_\nu - l \cdot l' g_{\mu\nu}) + 2i\lambda_l \epsilon_{\mu\nu\rho\sigma} l^\rho l'^\sigma \tag{2.3}$$

where the mass of the lepton is neglected, λ_l is the helicity of the incoming lepton, $g_{\mu\nu}$ and $\epsilon_{\mu\nu\rho\sigma}$ are the symmetric and antisymmetric tensors and l_α, l'_β are the components of the 4-vectors of the incoming and scattered lepton. M is the target nucleon mass and $W^{\mu\nu}$ is the hadronic tensor defined as

$$2MW^{\mu\nu} \quad (2.4)$$
$$\frac{1}{2\pi^3} \sum_X \int \frac{d^3\mathbf{P}_X}{2P_X^0} \delta^{(4)}(q + P - P_X - P_h) \overset{1}{<} P, S|J^\mu(0)|h, X >< h, X|J^\nu(0)|P, S >,$$

where J^μ is the electromagnetic current divided by the elementary charge, S is the target nucleon polarization and there is an implicit sum over the polarizations of all the hadrons in the final state.

Combining the possible polarizations of the incoming lepton beam (unpolarized or longitudinally polarized) and target nucleon (unpolarized, with longitudinal polarization S_L or with transverse polarization S_T with respect to the virtual photon direction) the differential SIDIS cross section can be written as:

$$d\sigma = d\sigma_{00} + \lambda_l d\sigma_{L0} + S_L(d\sigma_{0L} + \lambda_l d\sigma_{LL}) + S_T(d\sigma_{0T} + \lambda_l d\sigma_{LT}), \tag{2.5}$$

where $d\sigma_{BT}$ indicates the differential cross section $d^6\sigma_{BT}$ / $dxdyd\phi_S dzd\phi_h dP_T^{h^2}$ and B and T define the beam and target polarizations.

The inner structure of the nucleon gives rise to many azimuthal modulations in the differential SIDIS cross section. These modulations are given by independent linear combinations of the angles ϕ_h and ϕ_S so their amplitudes can be extracted from the same experimental data. The full expression of the terms appearing in eq. 2.5 [6], [5] are

$$
\begin{aligned}
d\sigma_{00} &= \frac{\alpha^2}{xyQ^2}\frac{y^2}{2(1-\epsilon)}\cdot\left\{F_{UU}+\sqrt{2\epsilon(1+\epsilon)}\cos\phi_h F_{UU}^{\cos\phi_h}+\epsilon\cos(2\phi_h)F_{UU}^{\cos 2\phi_h}\right\}\\
d\sigma_{L0} &= \frac{\alpha^2}{xyQ^2}\frac{y^2}{2(1-\epsilon)}\cdot\left\{\sqrt{2\epsilon(1-\epsilon)}\sin\phi_h F_{LU}^{\sin\phi_h}\right\}\\
d\sigma_{0L} &= \frac{\alpha^2}{xyQ^2}\frac{y^2}{2(1-\epsilon)}\cdot\left\{\sqrt{2\epsilon(1+\epsilon)}\sin\phi_h F_{UL}^{\sin\phi_h}+\epsilon\sin(2\phi_h)F_{UL}^{\sin 2\phi_h}\right\}\\
d\sigma_{LL} &= \frac{\alpha^2}{xyQ^2}\frac{y^2}{2(1-\epsilon)}\cdot\left\{\sqrt{1-\epsilon^2}F_{LL}+\sqrt{2\epsilon(1-\epsilon)}\cos\phi_h F_{LL}^{\cos\phi_h}\right\}\\
d\sigma_{0T} &= \frac{\alpha^2}{xyQ^2}\frac{y^2}{2(1-\epsilon)}\cdot\left\{\sin(\phi_h-\phi_S)F_{UT}^{\sin(\phi_h-\phi_S)}+\epsilon\sin(\phi_h+\phi_S)F_{UT}^{\sin(\phi_h+\phi_S)}\right.\\
&\quad +\epsilon\sin(3\phi_h-\phi_S)F_{UT}^{\sin(3\phi_h-\phi_S)}+\sqrt{2\epsilon(1+\epsilon)}\sin(\phi_S)F_{UT}^{\sin\phi_S}\\
&\quad \left.+\sqrt{2\epsilon(1+\epsilon)}\sin(2\phi_h-\phi_S)F_{UT}^{\sin(2\phi_h-\phi_S)}\right\}\\
d\sigma_{LT} &= \frac{\alpha^2}{xyQ^2}\frac{y^2}{2(1-\epsilon)}\cdot\left\{\sqrt{1-\epsilon^2}\cos(\phi_h-\phi_S)F_{LT}^{\cos(\phi_h-\phi_S)}\right.\\
&\quad \left.+\sqrt{2\epsilon(1-\epsilon)}\cos\phi_S F_{LT}^{\cos\phi_S}+\sqrt{2\epsilon(1-\epsilon)}\cos(2\phi_h-\phi_S)F_{LT}^{\cos(2\phi_h-\phi_S)}\right\}
\end{aligned}
$$

In the F terms appearing in eq. 2.6 the subscript indexes refer to the beam and target polarization respectively and the superscript to the corresponding azimuthal modulation. The term F_{UU} gives the ϕ_h and ϕ_S integrated contribution to the cross section. It is given by $F_{UU,T}+\epsilon F_{UU,L}$ where

$$
\begin{aligned}
\epsilon &= \frac{1-y-\frac{1}{4}\gamma^2y^2}{1-y-\frac{1}{2}y^2+\frac{1}{4}\gamma^2y^2},\\
\gamma &= \frac{2Mx}{Q}.
\end{aligned}
$$

The third subscript states the polarization of the virtual photon. $F_{UU,T}$ is the dominant contribution to the unpolarized cross section being the only one allowed in the elementary interaction with a spin 1/2 particle such as the quark. In the kinematical region where the transverse momentum of the outgoing hadron P_T^h is low compared to Q the amplitudes of the azimuthal modulations of the SIDIS cross section can be expressed in terms of the Transverse Momentum Dependent (TMD) Parton Distribution Functions (PDFs) and the Fragmentation Functions (FFs). Three PDFs describe the momentum and spin structure of the nucleon in the collinear approximation at leading order [10]. The $f_1(x)$ (or $q(x)$) PDF gives the probability density of finding an unpolarized quark inside an unpolarized nucleon carrying a fraction x

of the nucleon's momentum [7]. The other two are the so called helicity distribution $g_1(x)$ (or $\Delta q(x)$) and the transversity distribution $h_1(x)$ [8,9] (or $\Delta_T q(x)$) and describe polarized quarks inside polarized nucleons.

The helicity distribution gives the difference of the number density of quarks, in an helicity eigenstate, polarized along or against the nucleon polarization

$$g_1^q(x) = q^{\rightarrow\Rightarrow}(x) - q^{\rightarrow\Leftarrow}(x). \tag{2.6}$$

Because of the helicity conservation in the DIS process the exchanged virtual photon inherits the incoming lepton polarization and can interact only with those quarks which have an opposite polarization. This PDF can be probed in a reaction where the lepton beam is longitudinally polarized with respect to its direction of motion ($\rightarrow$) and scatters off a longitudinally polarized nucleon ($\Rightarrow$ or $\Leftarrow$). Indeed the cross section measurements of leptons which have polarization parallel ($\rightarrow \Rightarrow$) or anti-parallel ($\rightarrow \Leftarrow$) to the nucleon polarization are sensitive to the number densities $q^{\rightarrow\Rightarrow}$ and $q^{\rightarrow\Leftarrow}$ respectively. Of course the sum $q^{\rightarrow\Rightarrow}(x) + q^{\rightarrow\Leftarrow}(x)$ gives the unpolarized PDF $f_1(x)$.

The transversity distribution gives the difference of the number densities of quarks polarized along ($\Uparrow$) or opposite ($\Downarrow$) to the nucleon polarization ($\uparrow$), when the nucleon is transversely polarized with respect to the beam direction

$$h_1^q(x) = q^{\uparrow\Uparrow}(x) - q^{\uparrow\Downarrow}(x). \tag{2.7}$$

The transversity PDF h_1 is different from the helicity function g_1 because of the rotational symmetry breaking due to the relativistic motion in the longitudinal direction. The eigenstates of the transverse polarization are orthogonal the helicity eigenstates which means that the struck quark must flip its helicity at the virtual photon vertex. To be the reaction observed the quark must flip again the helicity and this could happen in the fragmentation process, when a final hadron is observed. Thus the transversity distribution, which is chiral-odd, need to be coupled another chiral-odd object to be measured since the chirality, being the same as the helicity in the zero mass approximation, is conserved. Thus transversity can be measured in SIDIS, for instance coupled with the Collins Fragmentation Function described in the next section, but not in DIS.

2.1 Transverse Momentum Dependent functions

Taking into account the intrinsic transverse momentum and the polarization the leading twist [1] hadronic tensor is described by 5 more scalar functions [6, 12] built starting from the available vectors and pseudo-vectors which characterize the struck quark and the target nucleon: the nucleon polarization $\mathbf{S}$, the quark polarization $\mathbf{s}_q$, the nucleon momentum $\mathbf{P}$ and the intrinsic transverse momentum of the quark $\mathbf{k}_\perp$, defined with respect to the virtual photon direction. These PDFs vanish in the collinear approximation and are called Transverse Momentum Dependent Parton

[1] An operational definition of twist is given in [11]

Distribution Functions (TMD PDFs) and give the number density of a quark q, inside the nucleon, with longitudinal momentum fraction x and intrinsic momentum $\mathbf{k}_\perp$.

One of the most famous TMD PDF is the Boer-Mulders function $h_1^\perp$ [13] which gives the difference of the distributions of transversely polarized quarks inside an unpolarized nucleon

$$q^\uparrow(x,\mathbf{k}_\perp) - q^\downarrow(x,\mathbf{k}_\perp) = -\frac{(\hat{\mathbf{P}}\times\mathbf{k}_\perp)\cdot\mathbf{s}_T}{M} h_1^\perp(x,k_\perp^2), \tag{2.8}$$

where $\hat{\mathbf{P}} = \mathbf{P}/|\mathbf{P}|$ is the unit vector of the nucleon momentum and $\mathbf{s}_T$ is the vector of the transverse polarization of the struck quark. The Boer-Mulders function is associated with the time reversal (T) odd correlation (between the intrinsic transverse momentum $\mathbf{k}_\perp$ and the transverse quark polarization $\mathbf{s}_T$) $(\hat{\mathbf{P}}\times\mathbf{k}_\perp)\cdot\mathbf{s}_T$, allowed, for example, in case of final state interactions, like a gluon exchange between the struck quark and the target remnant [14]. An important prediction due to the T-oddity is that $h_1^\perp$ should have an opposite sign when measured in SIDIS and in Drell-Yan reactions, where final state interactions are replaced by initial state interactions [16]. Moreover, since it is related to the transverse polarization of the quark, is a chiral-odd function and cannot be observed in the inclusive DIS (like the transversity PDF h_1). This function is thought to give account to the large $cos2\phi_h$ azimuthal asymmetries observed in the unpolarized Drell-Yan reaction [15].

The chiral-even partner of the Boer-Mulders function is the Sivers TMD PDF $f_{1T}^\perp$ [17] which gives the difference of the distributions of unpolarized quarks inside a transversely polarized nucleon

$$q^\Uparrow(x,\mathbf{k}_\perp) - q^\Downarrow(x,\mathbf{k}_\perp) = -\frac{(\hat{\mathbf{P}}\times\mathbf{k}_\perp)\cdot\mathbf{S}_T}{M} f_{1T}^\perp(x,k_\perp^2). \tag{2.9}$$

It is similar to eq. 2.8 but with the quark spin replaced by the target polarization $\mathbf{S}_T$ in the correlated with the intrinsic transverse momentum of the quark. Thus $f_{1T}^\perp$ is also a T-odd function and have the same prediction for the change of sign from SIDIS to DY as $h_1^\perp$. After the first calculation of TMD distributions, performed in a quark-diquark spectator model [18–20, 45], the domain of the TMDs has been explored in many theoretical works. From the models emerges that the Sivers function is expected to be negative for the u quark and positive for the d quark, while the Boer-Mulders function is expected to be negative for both the u and the d quark.

The functions $h_{1L}^\perp$ and g_{1T} are also called "worm gear" because they describe the relation between transverse/longitudinal polarization of the quark with the longitudinal/transverse polarization of the nucleon. The "pretzelosity" $h_{1T}^\perp$ is the distribution of the transversely polarized quark in a transversely polarized nucleon. It can be interpreted as a measure of the relativistic effects in the nucleon [22], which are known to be responsible for the difference between the helicity and the transversity distributions [23]. In some models is strictly related to the angular orbital momentum of the quark.

The evolution of the TMD distributions has been unknown until very recently and is therefore usually neglected or approximated in current phenomenological analysis.

In the collinear case, the fragmentation of a quark q in a hadron h with a fraction z of the available energy, is described by the Fragmentation Functions FFs $D_q^h(z)$. They are usually divided into favoured and unfavoured depending on the flavour q of the fragmenting quark and of the quarks which build the resulting hadron h. They are called favoured FF when the same flavour is present in the valence region of the target nucleon and of the produced hadron. When transverse momenta are taken into account the fragmentation of the struck quark into unpolarized hadrons is presently described by 2 kinds of scalar FFs, which can be obtained combining the momentum of the fragmenting quark ($\mathbf{k}_q$) and its polarization and the transverse momentum of the produced hadron $\mathbf{p}_\perp$ with respect to the direction of the fragmenting quark. When integrating over $\mathbf{p}_\perp$, only the $D_{1q}^h(z, \mathbf{p}_\perp)$ are different from zero. The correlation between the transverse momentum in the hadronization $\mathbf{p}_\perp$ and the polarization of the fragmenting quark is described by the Collins FF $H_1^\perp$ [21]. This function describes the fragmentation of a transversely polarized quark into an unpolarized hadron and gives a left-right asymmetry in the azimuthal distribution of the final state hadrons

$$h^\uparrow(z, \mathbf{p}_\perp) - h^\uparrow(z, \text{-}\mathbf{p}_\perp) = 2 \cdot \frac{(\hat{\mathbf{k}} \times \mathbf{p}_\perp) \cdot \mathbf{s}_q^{'}}{z M_h} H_1^\perp(z, p_{perp}^2), \tag{2.10}$$

where $h^\uparrow$ is the number density of hadrons produced from the fragmentation of a transversely polarized quark and $\mathbf{s}_q^{'}$ is the transverse component of the polarization of the fragmenting quark. The Collins mechanism corresponds to a preference of the hadron to be emitted on the left side if the quark spin $\mathbf{s}_q$ points upward. This mechanism acts as quark polarimeter since it generates azimuthal asymmetries related to the quark spin. A simple qualitative explanation of the Collins effect is provided by the "recursive string model" [24]. Measurements of the Collins asymmetries in SIDIS have been done by both the HERMES (on polarized proton [25]) and the COMPASS (on both deuteron [26] and proton [27] polarized target) collaborations and a signal different from zero was measured on the transversely polarized proton target. The combined measurements of the Collins asymmetry in both proton and deuteron polarized target allowed a first extraction of the Collins function and of the transversity function [43].

A simple geometrical relation holds in SIDIS between the intrinsic transverse momentum, in the fragmentation process, and the transverse momentum of the hadron P_T^h calculated in GNS

$$\mathbf{P}_T^h = z\mathbf{k}_\perp + \mathbf{p}_\perp, \tag{2.11}$$

as illustrated in fig. 2.2. This relation is valid up to first order in $k_\perp/Q$ [75] when z can be identified with the longitudinal momentum fraction of the fragmenting quark carried by the hadron h.

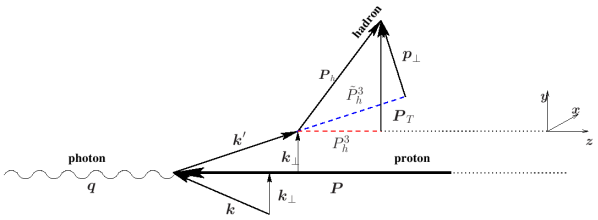

Figure 2.2: Kinematic of the fragmentation process.

2.2 The azimuthal asymmetries

The structure functions F appearing in the differential SIDIS cross section written in eq. 2.6 can be factorized [2] and written as the convolution over the transverse momenta of the TMD PDFs $f_q(x, \mathbf{k}_\perp)$ and the FFs $D_q^h(z, \mathbf{p}_\perp)$

$$C[wfD] = \sum_q e_q^2 x \int d^2\mathbf{k}_\perp d^2\mathbf{p}_\perp \delta^2(z\mathbf{k}_\perp - \mathbf{p}_\perp - \mathbf{P}_T^h) w(\mathbf{k}_\perp, \mathbf{p}_\perp) f^a(x, k_\perp^2) D_q(z, p_\perp), \tag{2.12}$$

where the sum runs over the flavour q of quarks and anti-quarks.

The non vanishing leading twist structure functions are [30]:

$$F_{UU,T} = C[f_1 D_1], \tag{2.13}$$

$$F_{UU}^{\cos 2\phi_h} = C\Big[- \frac{2(\hat{\mathbf{h}}\cdot\mathbf{k}_\perp)(\hat{\mathbf{h}}\cdot\mathbf{p}_\perp) - \hat{\mathbf{h}}\cdot\mathbf{k}_\perp \cdot \hat{\mathbf{h}}\cdot\mathbf{p}_\perp}{M M_h} h_1^\perp H_1^\perp \Big], \tag{2.14}$$

$$F_{UL}^{\sin 2\phi_h} = C\Big[- \frac{2(\hat{\mathbf{h}}\cdot\mathbf{k}_\perp)(\hat{\mathbf{h}}\cdot\mathbf{p}_\perp) - \hat{\mathbf{h}}\cdot\mathbf{k}_\perp \cdot \hat{\mathbf{h}}\cdot\mathbf{p}_\perp}{M M_h} h_{1L}^\perp H_1^\perp \Big], \tag{2.15}$$

$$F_{LL} = C[g_{1L} D_1], \tag{2.16}$$

$$F_{UT}^{\sin(\phi_h - \phi_S)} = C\Big[- \frac{\hat{\mathbf{h}}\cdot\mathbf{k}_\perp}{M} f_{1T} D_1 \Big], \tag{2.17}$$

$$F_{UT}^{\sin(\phi_h + \phi_S)} = C\Big[- \frac{\hat{\mathbf{h}}\cdot\mathbf{p}_\perp}{M_h} h_1 H_1^\perp \Big], \tag{2.18}$$

[2] When taking into account the intrinsic transverse momentum of the quark inside the nucleon the factorization of the SIDIS cross section has been proved [28,29]in the kinematical region where the transverse momentum of the outgoing hadron P_T^h is low compared to Q.

$$F_{UT}^{\sin(3\phi_h-\phi_S)} = C\Big[\frac{2(\hat{\mathbf{h}}\cdot\mathbf{p}_\perp)(\mathbf{k}_\perp\cdot\mathbf{p}_\perp)+k_\perp^2(\hat{\mathbf{h}}\mathbf{k}_\perp)-4(\hat{\mathbf{h}}\cdot\mathbf{k}_\perp)^2(\mathbf{h}\cdot\mathbf{p}_\perp)}{2M^2M_h}h_{1T}^\perp H_1^\perp\Big], \quad (2.19)$$

$$F_{LT}^{\cos(\phi_h-\phi_S)} = C\Big[\frac{\hat{\mathbf{h}}\cdot\mathbf{k}_\perp}{M}g_{1T}D_1\Big], \quad (2.20)$$

where $\hat{\mathbf{h}} = \mathbf{P}_T^h/|\mathbf{P}_T^h|$. The terms in eq. 2.17 and in eq. 2.18 gives the Sivers and Collins asymmetries respectively, and have been measured from SIDIS by COMPASS (as all the other transverse spin dependent asymmetries given by the F_{xT} terms).

The only leading twist term giving an azimuthal asymmetry in the unpolarized SIDIS is $F_{UU}^{\cos 2\phi_h}$ resulting from the convolution of the Boer-Mulders function $h_1^\perp$ with the Collins fragmentation function $H_1^\perp$. However, an azimuthal modulation in $\cos\phi$ is also expected in the unpolarized SIDIS cross section. It is given by a pure kinematical effect, which was suggested long time ago by Cahn [32], arising from the intrinsic transverse motion of quarks. It appears in the twist 3 (i.e. multiplied by a factor $1/Q$) term

$$F_{UU}^{\cos\phi_h} = \frac{2M}{Q}C\Big[-\frac{(\hat{\mathbf{h}}\cdot\mathbf{p}_\perp)k_\perp^2}{M_hM^2}h_1^\perp H_1^\perp - \frac{\hat{\mathbf{h}}\cdot\mathbf{k}_\perp}{M}f_1D_1\Big], \quad (2.21)$$

in the convolution of the unpolarized PDF f_1 and the unpolarized FF D_1. In the same term a contribution coming from the convolution of the Boer-Mulders function $h_1^\perp$ and the Collins function $H_1^\perp$ also appears. A kinematical contribution due to the Cahn effect emerges also (at twist 4, multiplied by a factor $1/Q^2$) in the $\cos 2\phi_h$ term

$$F_{UU,Cahn}^{\cos 2\phi_h} = \frac{M^2}{Q^2}C\Big[\frac{2(\hat{\mathbf{h}}\cdot\mathbf{k}_\perp)^2-k_\perp^2}{M^2}f_1D_1\Big], \quad (2.22)$$

thus generating the same asymmetry as the one given by the leading twist part of the $F_{UU}^{\cos 2\phi_h}$ structure function and given by the Bour-Mulders function.

The complete expression of all the structure functions appearing in eq. 2.6 including twist 3 effects (due to the quark-gluon-quark correlators and the kinematically suppressed component in the light-cone reference frame) is given in [5].

More on the Cahn effect

It is interesting to derive the azimuthal SIDIS cross section taking into account only the Chan effect and in the case of a longitudinally polarized target nucleon It has been already shown that this kinematical effect gives an azimuthal $\cos_{phi_h}$ modulation in the spin independent part of the elementary cross section. Other contributions can come also from the scattering between polarized beam and polarized quark [34]. Indeed, taking into account the intrinsic transverse momentum of the quarks and the polarizations of the incoming lepton and of the struck quark the elementary cross section can be written as

$$\frac{d\hat{\sigma}^{lq\to lq}}{dQ^2d\phi} \propto \frac{\hat{s}^2+\hat{u}^2+\lambda_l\lambda_q(\hat{s}^2-\hat{u}^2)}{\hat{t}^2}, \quad (2.23)$$

where ϕ is the azimuthal angle of the struck quark, i.e. before the fragmentation process, and λ_q is the quark helicity. Keeping terms up to order $k_\perp/Q$ and neglecting the masses the Mandelstam variables for the non-coplanar lepton quark scattering are expressed as:

$$\begin{aligned} \hat{s} &= xs\Big[1 - 2\sqrt{1-y}\frac{k_\perp}{Q}\cos\phi\Big], \qquad (2.24)\\ \hat{t} &= -xys, \\ \hat{u} &= xs(1-y)\Big[1 - 2\frac{k_\perp}{Q\sqrt{1-y}}\cos\phi\Big], \qquad (2.25) \end{aligned}$$

where the azimuthal modulations are proportional to the magnitude of the intrinsic transverse momentum of the quark $k_\perp$. The first part of the eq. 2.23 gives the Cahn effect for an unpolarized quark while the second part appears when the quark has a polarization S_L parallel to the virtual photon direction.

Taking into account only the effect given by the elastic lepton-quark polarized scattering, the differential SIDIS cross section can then be written as:

$$\begin{aligned} \frac{d^5\sigma}{dxdydzd\phi_h dP_T^{h^2}} &= \frac{\alpha^2}{xyQ^2}\frac{1+(1-y)^2}{2}\cdot\Bigg\{F_{UU} + \qquad (2.26)\\ &+\frac{2(2-y)\sqrt{1-y}}{1+(1-y)^2}F_{UU,Cahn}^{\cos\phi_h}\cos\phi_h + \\ &+\lambda_l P_L\frac{2y\sqrt{1-y}}{1+(1-y)^2}F_{LL,Cahn}^{\cos\phi_h}\cos\phi_h + \end{aligned}$$

where:

$$\begin{aligned} F_{UU} &= C[f_1\, D_1], \qquad (2.27)\\ F_{UU,Cahn}^{\cos\phi_h} &= \frac{2}{Q}C[-\hat{\mathbf{h}}\cdot\mathbf{k}_\perp\cdot f_1\, D_1], \\ F_{LL,Cahn}^{\cos\phi_h} &= \frac{2}{Q}C[-\hat{\mathbf{h}}\cdot\mathbf{k}_\perp\cdot g_1\, D_1], \end{aligned}$$

These structure functions are the same as the ones appearing in eq. 2.6 but considering only the Cahn effect contributions. They can be computed assuming a gaussian dependence on the distribution of the intrinsic transverse momentum $\mathbf{k}_\perp$ of the quark inside the nucleon and of the hadron produced in the fragmentation $\mathbf{p}_\perp$ and that the PDFs and FFs functions can be factorized in two pieces, one enclosing the dependence from x or z and the other having a gaussian dependence from the squared modulus of the transverse momentum

$$f_1^q(x,\mathbf{k}_\perp) = f_1^q(x)\frac{1}{\pi < k_\perp^2 >}e^{\left(-\frac{k_\perp^2}{<k_\perp^2>}\right)}, \qquad (2.28)$$

$$D_{1q}(z,\mathbf{p}_\perp) = D_{1q}^h(z)\frac{1}{\pi < p_\perp^2 >}e^{\left(-\frac{p_\perp^2}{<p_\perp^2>}\right)}. \qquad (2.29)$$

The function g_1 can be similarly written using the same parameter $< k_\perp^2 >$ to describe the width of the distributions of the intrinsic transverse momentum of the quark inside the nucleon. Thus the convolution over the transverse momenta leads to (as shown in appendix A):

$$F_{UU} = x \sum_q e_q^2 \, f_1^q(x) \, D_{1q}^h(z) \frac{1}{\pi(z^2 < k_\perp^2 > + < p_\perp^2 >)} e^{-\frac{P_T^{h\,2}}{z^2 < k_\perp^2 > + < p_\perp^2 >}} \quad (2.30)$$

$$F_{UU,Cahn}^{\cos\phi_h} = (-1)\frac{2}{Q} x \sum_q e_q^2 \, f_1^q(x) \, D_{1q}^h(z) \frac{z \, P_T^h \, < k_\perp^2 > e^{\frac{P_T^{h\,2}}{< P_T^{h\,2} >}}}{\pi < P_T^{h\,2} >^2} \quad (2.31)$$

$$F_{LL,Cahn}^{\cos\phi_h} = (-1)\frac{2}{Q} x \sum_q e_q^2 \, g_1^q(x) \, D_{1q}^h(z) \frac{z \, P_T^h \, < k_\perp^2 > e^{\frac{P_T^{h\,2}}{< P_T^{h\,2} >}}}{\pi < P_T^{h\,2} >^2} \quad (2.32)$$

$$(2.33)$$

All the structure functions which give the azimuthal dependence of the differential cross section in eq. 2.26 are thus proportional to the mean intrinsic transverse momentum squared $< k_\perp^2 >$ and have the same dependence on z and P_T^h. The amplitudes appearing in eq. 2.26 differ for the y dependence and the PDFs involved: the unpolarized PDF f_1, the helicity g_1, both well known.

2.3 Existing measurements

Important results on the Collins and Sivers asymmetries both on proton and on deuteron have been obtained from COMPASS. The outcome of global analysis performed on COMPASS data on deuteron, HERMES data on proton and BELLE data from e^+e^- collisions, tell that, assuming the quark u dominance, the Collins FF is not zero and favoured and unfavoured are roughly the same size but opposite in sign.

The first results on the unpolarized DIS hadron azimuthal asymmetries came from the European Muon Collaboration (EMC) [36]. In the kinematical range $Q^2 >$ 5 GeV^2 and $60 < W^2 < 360$ GeV^2 they measured a large amplitude $F_{UU}^{\cos\phi_h}/F_{UU}$ (about 10%) for the $\cos\phi_h$ modulation increasing with z and also with P_T^h. Most of their data are in the region $P_T^h < 3$ GeV and their conclusion was that the azimuthal asymmetries they observed were mostly due the non zero intrinsic transverse momentum of the quark as predicted by Cahn. They also measured a smaller amplitude $F_{UU}^{\cos 2\phi_h}/F_{UU}$ of the $\cos 2\phi$ modulation. In general the statistics was not high enough to measure separately positive and negative hadrons azimuthal asymmetries. EMC measured also the transverse momentum of charged hadrons observed in DIS and tested the relation between the mean values of the transverse momenta where, the transverse momentum calculated from the perturbative QCD has been added to the contribution coming from eq. 2.38. The results [35] confirmed that the main contribution to the mean value of transverse momentum of the hadron $< P_T^{h^2} >$ is given by the Cahn effect.

Later experiments like HERMES, COMPASS and now also CLAS have measured the azimuthal amplitudes expected on the unpolarized target with a much higher statistic and separately for positive and negative hadrons, since the Cahn effect is predicted to have no dependence on the charge of the produced hadron. On the contrary the contribution coming from the Boer-Mulders PDF, since it appears coupled with the Collins FF, allows for some dependence on the hadron's charge. Also it is interesting to measure the amplitude $F_{LU}^{\sin\phi_h}/F_{UU}$, which have been found different from zero at HERMES [47], to see if this sub-leading twist effect is suppressed in the COMPASS kinematics (which is characterized by higher Q^2).

An important part of this thesis is the measurement of the unpolarized SIDIS asymmetries from the COMPASS data on deuteron, described in chapter 5. The interpretation of the results, also in relation with a possible extraction of the intrinsic transverse momentum of the quark from the Cahn effect, and their comparison with results from other experiments are shown and discussed in chapter 6.

The second part of this work 7 is dedicated to the measurements of the azimuthal asymmetries in the hadrons produced in DIS extracted from the COMPASS data on the longitudinal polarized deuteron target. The contributions coming from the Cahn effect have been already calculated in section 2.2. Four independent azimuthal modulations can be measured: $\sin\phi_h$, $\sin 2\phi_h$, $\sin 3\phi_h$ and $\cos\phi_h$. It is interesting to measure the relevance of the higher twist effects appearing in those modulations at the COMPASS kinematics, they can be related to higher order terms related to the intrinsic transverse momentum, but also to a more complex dynamics possibly given by gluonic interactions [5].

APPENDIX A

$$
\begin{aligned}
F_{UU} &= x\sum_q e_q^2\, f_1^q(x)\, D_{1q}^h(z) \int d^2\mathbf{k}_\perp d^2\mathbf{p}_\perp \cdot \delta^2(z\mathbf{k}_\perp + \mathbf{p}_\perp - \mathbf{P}_T^h)\cdot \qquad (2.34)\\
&\quad \cdot \frac{1}{\pi < k_\perp^2 >} e^{-\frac{\mathbf{k}_\perp^2}{<k_\perp^2>}} \cdot \frac{1}{\pi < p_\perp^2 >}\; e^{-\frac{\mathbf{p}_\perp^2}{<p_\perp^2>}}\\
&= x\sum_q e_q^2\, f_1^q(x)\, D_{1q}^h(z) \int d^2\mathbf{k}_\perp \frac{1}{\pi < k_\perp^2 >} e^{\left(-\frac{\mathbf{k}_\perp^2}{<k_\perp^2>}\right)} \frac{1}{\pi < p_\perp^2 >} \cdot e^{(-\frac{(\mathbf{P}_T^h - z\mathbf{k}_\perp)^2}{<p_\perp^2>}}\\
&= x\sum_q e_q^2\, f_1^q(x)\, D_{1q}^h(z) \int d^2\mathbf{k}_\perp \frac{1}{\pi^2 < k_\perp^2 >< p_\perp^2 >} e^{-\left(\frac{\mathbf{k}_\perp^2}{<k_\perp^2>} + \frac{(\mathbf{P}_T^h - z\mathbf{k}_\perp)^2}{<p_\perp^2>}\right)}.
\end{aligned}
$$

Let now expand the exponent

$$
\begin{aligned}
&\frac{\mathbf{k}_\perp^2}{< k_\perp^2 >} + \frac{(\mathbf{P}_T^h - z\mathbf{k}_\perp)^2}{< p_\perp^2 >} = \frac{z^2 < k_\perp^2 > + < p_\perp^2 >}{< k_\perp^2 >< p_\perp^2 >}\mathbf{k}_\perp^2 + \frac{1}{< p_\perp^2 >}\mathbf{P}_T^{h^2} - 2z\frac{1}{< p_\perp^2 >}\mathbf{k}\cdot\mathbf{P}_T^h\\
&= \left(\frac{z^2 < k_\perp^2 > + < p_\perp^2 >}{< k_\perp^2 >< p_\perp^2 >}\right)\cdot\left(\mathbf{k}_\perp^2 + \frac{< k_\perp^2 >}{z^2 < k_\perp^2 > + < p_\perp^2 >}\mathbf{P}_T^{h^2} - 2\frac{z < k_\perp^2 >}{z^2 < k_\perp^2 > + < p_\perp^2 >}\mathbf{k}\cdot\mathbf{P}_T^h\right)\\
&= \left(\frac{z^2 < k_\perp^2 > + < p_\perp^2 >}{< k_\perp^2 >< p_\perp^2 >}\right)\left(\mathbf{k}_\perp - \frac{z < k_\perp^2 >}{z^2 < k_\perp^2 > + < p_\perp^2 >}\mathbf{P}_T^h\right)^2 + \frac{1}{z^2 < k_\perp^2 > + < p_\perp^2 >}\mathbf{P}_T^{h^2}.
\end{aligned}
$$

Defining

$$
\mathbf{t} = \sqrt{\frac{z^2 < k_\perp^2 > + < p_\perp^2 >}{< k_\perp^2 >< p_\perp^2 >}}\cdot\left(\mathbf{k}_\perp - \frac{z < k_\perp^2 >}{z^2 < k_\perp^2 > + < p_\perp^2 >}\mathbf{P}_T^h\right), \qquad (2.35)
$$

it is

$$
F_{UU} = x\sum_q e_q^2\, f_1^q(x)\, D_{1q}^h(z)\frac{1}{\pi^2 < k_\perp^2 >< p_\perp^2 >}\, e^{-\frac{P_T^{h^2}}{z^2 < k_\perp^2 > + < p_\perp^2 >}}\, \frac{< k_\perp^2 >< p_\perp^2 >}{z^2 < k_\perp^2 > + < p_\perp^2 >}\int d^2\mathbf{t} e^{-t^2}
$$

and finally

$$
F_{UU} = x\sum_q e_q^2\, f_1^q(x)\, D_{1q}^h(z)\frac{e^{-\frac{P_T^{h^2}}{z^2 < k_\perp^2 > + < p_\perp^2 >}}}{\pi(z^2 < k_\perp^2 > + < p_\perp^2 >)} \qquad (2.36)
$$

Using the relation of eq. 2.11 $\mathbf{P}_T^h = z\mathbf{k}_\perp + \mathbf{p}_\perp$ the mean of the squared transverse momentum of the hadron $< P_T^{h^2} >$ can be written as

$$
< P_T^{h^2} >= z^2 < k_\perp^2 > + < p_\perp^2 > + 2 < \mathbf{k}_\perp \cdot \mathbf{p}_\perp > \qquad (2.37)
$$

where the mean value of the scalar product between the transverse momenta $< \mathbf{k}_\perp \cdot \mathbf{p}_\perp >$ is zero since the intrinsic transverse momentum of the struck quark $\mathbf{k}_\perp$ is

not correlated to the transverse momentum of the hadron in the fragmentation $\mathbf{p}_\perp$. Then

$$< P_T^{h^2} >= z^2 < k_\perp^2 > + < p_\perp^2 >, \tag{2.38}$$

and, substituting $z^2 < k_\perp^2 > + < p_\perp^2 >$, eq. 2.36 can be written as

$$F_{UU} = x \sum_q e_q^2 \, f_1^q(x) \, D_{1q}^h(z) \frac{e^{-\frac{P_T^{h^2}}{< P_T^{h^2} >}}}{\pi < P_T^{h^2} >} \tag{2.39}$$

$F_{UU,Cahn}^{\cos\phi_h}$ has the scalar product $-\hat{\mathbf{h}} \cdot \mathbf{k}_\perp$ in the convolution over the transverse momenta

$$\begin{aligned} F_{UU,Cahn}^{\cos\phi_h} &= (-1) \frac{2}{Q} x \sum_q e_q^2 \, f_1^q(x) \, D_{1q}^h(z) \int d^2\mathbf{k}_\perp d^2\mathbf{p}_\perp \, \hat{\mathbf{h}} \cdot \mathbf{k}_\perp \delta^2(z\mathbf{k}_\perp - \mathbf{p}_\perp - \mathbf{P}_T^h) \cdot \\ &\cdot \frac{1}{\pi < k_\perp^2 >} e^{-\frac{\mathbf{k}_\perp^2}{< k_\perp^2 >}} \cdot \frac{1}{\pi < p_\perp^2 >} \, e^{-\frac{\mathbf{p}_\perp^2}{< p_\perp^2 >}} \end{aligned}$$

where the exponent is the same and, after the integration on $d^2\mathbf{p}_\perp$, the same change of variable of 2.35 can be done. Thus the integral:

$$\int d^2\mathbf{k}_\perp \, \hat{\mathbf{h}} \cdot \mathbf{k}_\perp \, e^{-\frac{z^2 < k_\perp^2 > + < p_\perp^2 >}{< k_\perp^2 >< p_\perp^2 >} \cdot \left(\mathbf{k}_\perp - \frac{z < k_\perp^2 >}{z^2 < k_\perp^2 > + < p_\perp^2 >} \mathbf{P}_T^h \right)^2}$$

can be written as

$$\left(\frac{z^2 < k_\perp^2 > + < p_\perp^2 >}{< k_\perp^2 >< p_\perp^2 >} \right)^{-3} \int d^2\mathbf{t} \, \hat{\mathbf{h}} \cdot \mathbf{t} e^{-t^2} \; + \; \frac{z < k_\perp^2 >< k_\perp^2 >< p_\perp^2 >}{(z^2 < k_\perp^2 > + < p_\perp^2 >)^2} \, P_T^h \int d^2\mathbf{t} e^{-t^2}$$

where the first term is an odd integral and it gives zero. Finally:

$$F_{UU,Cahn}^{\cos\phi_h} = (-1) \frac{2}{Q} x \sum_q e_q^2 \, f_1^q(x) \, D_{1q}^h(z) \frac{z \, P_T^h \, < k_\perp^2 > e^{\frac{P_T^{h^2}}{< P_T^{h^2} >}}}{\pi < P_T^{h^2} >^2} \tag{2.40}$$

Chapter 3

The COMPASS Experiment

COMPASS (COmmon Muon and Proton Apparatus for Structure and Spectroscopy) is a fixed target experiment installed in the M2 beam line at the CERN SPS. The experiment was approved in 1997 with a borad physics programme including the study of the spin structure of the nucleon, and in particular the direct measurement of ΔG, the gluon contribution to the nucleon spin, to be done using a high energy muon beam and polarized targets. The other important part of the COMPASS programme was hadron spectroscopy using high energy hadron beams and liquid hydrogen and nuclear targets.

The data taking started in 2002, with the study of the nucleon spin structure. In 2002, 2003, 2004 (apart from a short hadron beam test) and 2006 data were taken with a 160 GeV μ^+ beam longitudinally polarized and a ^{6}LiD polarized target. In the first three years the target was polarized transversely with respect to the beam direction during $\sim$ 20% of the time and longitudinally for $\sim$ 80% of the time. In 2006 data were only taken with longitudinally target polarization to conclude the measurement of ΔG. In 2007 a NH^3 target (transversely and longitudinally polarized $\sim$ 50% of the time) was used with the 160 GeV μ^+ beam. In 2008 and 2009 the data taking was devoted to hadron spectroscopy, while the muon programme restarted in 2010, with one one year of data taking with the NH^3 target transversely polarized, in order to improve the measurement performed in 2007. The measurement with the longitudinally polarized NH^3 target which will take place in 2011 will conclude the first phase of COMPASS. For the following years new Primakoff measurements and further studies of the nucleon structure via Drell-Yann with π beam and transversely polarized target and DVCS on LH_2 and μ beam, proposed by the COMPASS II Collaboration, have already been approved by the CERN RB.

This thesis is devoted to the study of the nucleon structure from the data collected with the ^{6}LiD target mainly in the years 2002-2004. In this chapter the experimental apparatus used in 2004 (slightly improved with respect to the previous years) is described. In 2005 the apparatus was upgraded in particular for the polarized target magnet, the RICH1, and the elctro-magnetic calorimeters.

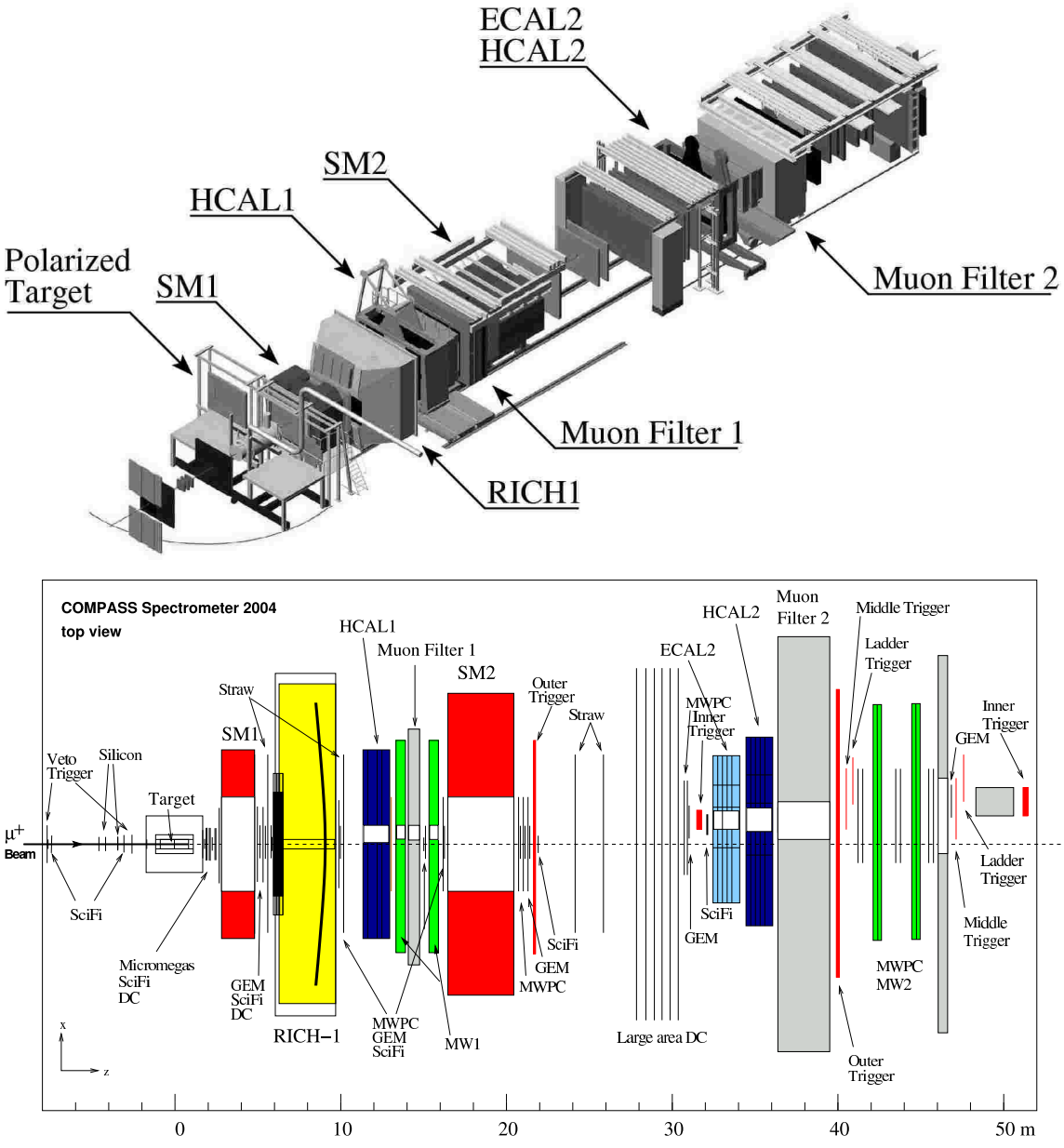

Figure 3.1: Compass 2004 muon setup (top) artistic view, (bottom) top view.

3.1 The COMPASS apparatus

The muon physics programme imposes specific requirements to the experimental setup. They are: large angle and momentum acceptance, including the request to track particles scattered at extremely small angles, precise kinematic reconstruction of the events together with efficient particle identification and good mass resolution. Operation at high luminosity imposes capabilities of high beam intensity and counting rates, high trigger rates and huge data flows.

The basic layout of the COMPASS spectrometer, as it was used in 2004, is shown in Fig. 3.1. Three parts can be distinguished. The first part includes the detectors upstream of the target, which measures the incoming beam particles. The second and the third part of the setup are located downstream of the target, and extend over a total length of 50 m. These are the Large Angle Spectrometer (LAS) and the Small Angle Spectrometer (SAS), respectively. The use of two spectrometers for the outgoing particles is a consequence of the large momentum range and the large angular acceptance requirements. Each of the two spectrometers is built around an analysing magnet, preceded and followed by telescopes of trackers and completed by a hadron calorimeter and by a muon filter station for high energy muon identification. The angular acceptance of the first analysing magnet (SM1) matches the required angular acceptance of 180 mRad. The two analysing magnet, SM1 and SM2, have different deflecting power (1 Tm for SM1 and 4.4 Tm for SM2) according to the characteristics of the particles they analyse: the mean momentum of the large angle particles, analysed by SM1, is lower. A RICH detector for hadron identification is part of the large angle spectrometer. The small angle spectrometer includes an electromagnetic calorimeter.

3.2 The muon beam

The beam line M2 provides high-intensity positive muon beam up to 190 GeV/c and is shown in fig. 3.2. It derives from a very intense primary proton beam, extracted from the CERN SPS at 400 GeV/c momentum, that impinges on a Beryllium target with 500 mm thickness (T6). Mainly pions (with a 3.6% of kaons contamination) are produced in the interaction and the particles with 225 GeV/c $\pm$10% momentum are selected by a sequence of dipole and quadrupole magnets and carried through a 600 m beam line where the pions decay in $\mu\,\nu$. The muon are selected by the Berillium absorber which stops the other, less penetrating particles. The COMPASS average longitudinal beam polarization, essential for the double spin asymmetries, is -80% and it is naturally given by the parity violating nature of the pion decay (it is -100% in the pion rest frame).

Before entering the experimental hall, the beam passes through a series of dipole and quadrupole magnets (for $\sim$ 400 m) where the charge is selected and the extension of the transverse section is reduced. In the hall the resulting beam has a section of 8×8 mm^2, a divergence of 0.4×0.8 mrad^2 and a momentum resolution of 5%. The high intensity of the beam ($2 \cdot 10^8$ μ/spill) translates into a rate of $\sim 4 \cdot 10^7$ μ/s for the duty cicle of 4.8 s/16.8 s.

The beam momentum is measured by the Beam Momentum Station (BMS),

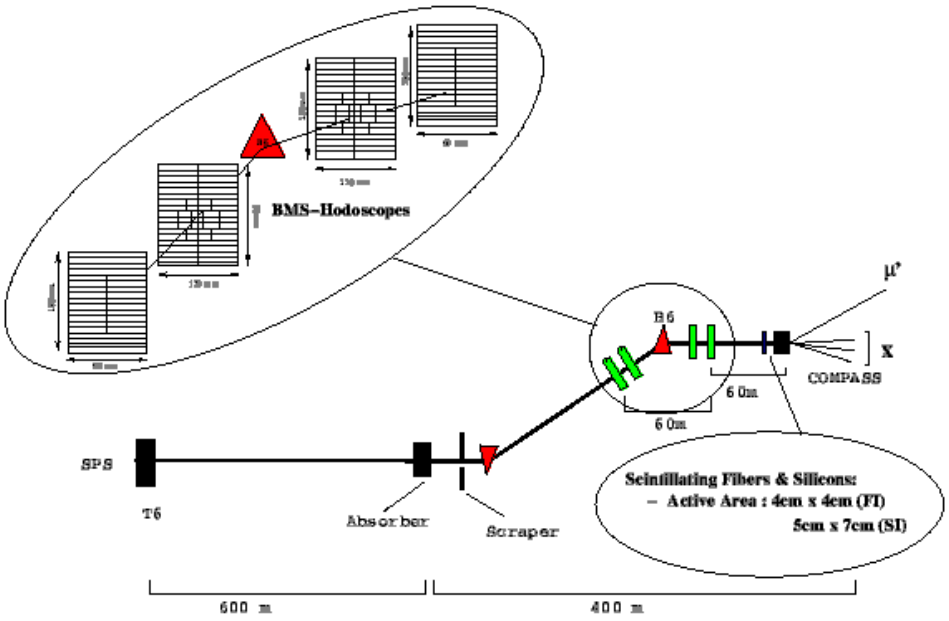

Figure 3.2: The M2 beam line.

located along the beam line about 60 m upstream of the experimental hall. As illustrated in fig. 3.2 the BMS includes an analysing magnet and two telescopes of tracking stations formed by scintillator hodoscopes and scintillating fibre (SciFi) detectors characterized by a good time resolution ($\sim$ 300 ps) resulting in a beam momentum resolution $\lesssim 3\%$.

A precise track reconstruction of the incident particle is provided by two stations of scintillating fibres and three stations of silicon microstrip detectors and the beam efficiency reconstruction is $\sim 93\%$.

Scintillator veto counters define the beam spot size and separate the beam from the "beam halo", particles which do not pass through the target but cross the spectrometer giving spurious trigger signals and interfering with the event reconstruction.

3.3 The polarized target

The COMPASS polarized target system is shown in fig. 3.3. The choice of a solid state polarised target has been driven by the high statistic required for the extraction of the spin asymmetries, thus a high luminosity is needed.

Deuterated lithium (^{6}LiD) has been chosen as isoscalar target material and it is contained in two 60 cm long cells placed along the nominal beam line and separated by 10 cm. This material allows to reach a high degree of deuteron polarisation ($> 40\%$) and has a very favourable composition as it can considered to a good approximation as a spin-0 ^{4}He nucleus and a deuteron [48]. The fraction of polarisable material f (dilution factor) is of the order of 0.35 and is given by the ratio of the absorption cross-sections on the deuteron to that of all nuclei in the target cells. It includes a correction for the relative polarisation of deuterons bound in ^{6}Li with

respect to free deuterons.

While electron spins can be aligned in a magnetic field and give rise to a large polarisation at equilibrium for a low enough temperature, only a negligible nuclear spin polarisation can be reached. Therefore, solid state polarised targets rely on dynamic nuclear polarisation (DNP) which transfers the electron polarisation to the nuclear spins by means of a microwave field [49]. This process requires a material containing some amount of paramagnetic centres, e.g. created by irradiation, a temperature below 1 K and a strong and homogeneous magnetic field. The COMPASS polarised target has been designed to meet these requirements. The superconducting solenoid produces a 2.5 T magnetic field along the beam direction. Sixteen corrections coils are used to obtain an axial homogeneity better than 20 ppm in a volume 1500 mm long, and 50 mm in diameter. A transverse holding field of 0.42 T is produced by a dipole coil and deviates at most by 10% from its nominal value inside the target volume. The very low temperature, obtained by the ^{3}He/^{4}He dilution refrigerator, is kept by the liquid helium which fills both the target and the space between the ^{6}LiD crystals.

The target cells can be polarized both along the nominal beam direction (longitudinal mode) and orthogonal to that direction (transverse mode). In both cases the target cells have opposite polarizations. When in longitudinal mode the polarization is coupled to the 2.5 T magnetic field and the polarization is reversed every ~ 8 hours by rotating the solenoid field. Every ~ 3 weeks the coupling of the polarizations to the solenoid field is reversed by exchanging the microwave frequencies of the two cells. During data taking in transverse mode, the target material is kept in frozen spin mode below 90 mK and the spin direction is maintained by the 0.42 T transverse dipole field. The polarisation is reversed, via microwave reversal, usually every 5 days of data taking. The fig. 3.4 shows the trend of the measured polarization for both the target cells during part of the 2004 data taking.

The fact that the data are simultaneously taken with the two oppositely polarized target cells and the polarizations are periodically inverted allow to minimize the systematic effects, due to the different acceptance of the two cells and to the time instability of the spectrometer, in the measurement of the spin dependent asymmetries.

In 2005 [51] the large acceptance COMPASS solenoid was installed to the previously used SMC magnet. Also the target material was distributed in 3 cells 15, 30, 15 cm long, with the middle cell oppositey polarized with respect to the other two, in order to have the same mean acceptance between the two spin configuration.

3.4 The tracking detectors

The tracking system of COMPASS comprises many tracking stations, distributed over the entire length of the spectrometer. Each tracking station consists of a set of detectors of the same type, located at approximately the same Z-coordinate along the beam. In a station, the trajectory of a charged particle is measured in several projections transverse to the beam direction in order to reduce ambiguities. Many different detector technologies of varying rate capability, resolution, and active area

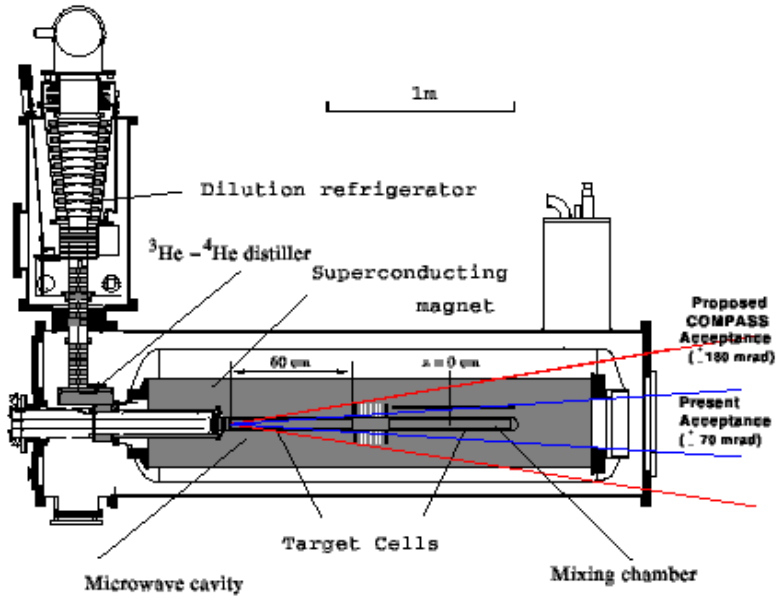

Figure 3.3: The COMPASS polarized target system. The angular acceptances of the magnet used up to 2004 and of the proposed magnet, installed in 2005, are also shown.

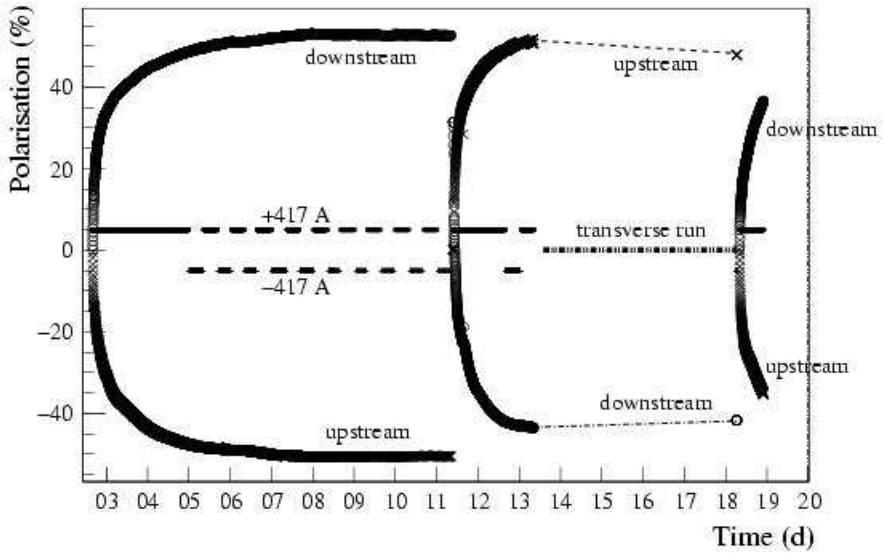

Figure 3.4: Average polarisations in the upstream and downstream target cells during 20 days of the 2004 run. The polarisations in the target cells are reversed by changing the microwave frequencies after day 11. Data are taken in transverse mode from day 13 to day 18 and a new field reversal by microwaves is performed at the end of the period. The current of ±417 A corresponds to the axial field of 2.5 T.

are in use, dictated by the increasing particle rates closer to the beam axis, and by the spectrometer acceptance.

The paricle flux investing the whole region covered by apparatus acceptance varies by 5 order of magnitude. In the zone along the beam the tracking detectors have to be characterized by an exellent spatial resolution and must cope with the high particle rate. Also, the amount of the material have to be minimized in order to reduce multiple scattering and the effects due to the secondary interactions. Going towards the outer zone from the beam line the requested spatial resolution is lower but the area to be covered increases.

Thus the tecniques employed by the detectors follow the requirements given by the particle rates, by the spatial and time resolution and by the area covered by the sensitive materials. A first classification of the detectors can be done starting from their acceptance coverage and their distance from the beam; hence they can be divided in VSAT (Very Small Area Trackers), SAT (Small Area Trackers) and LAT (Large Area Trackers).

- **Very Small Area Trackers (VSAT)**. These detectors cover the nominal beam region up to a radial distance of 2.5 - 3cm. The very high rate of particles in this area (up to about 10^5 s^{-1} mm^{-2} in the centre of the muon beam) requires excellent time or position resolution of the corresponding detectors in order to identify hits belonging to the same track. Scintillating fibres and silicon microstrip detectors fulfil this task.

  - Scintillating fibre detectors are placed upstream and downstream of the target. Several layers of fibres are stacked for each projection, the fibre axes of one layer being shifted with respect to the ones of the next layer and the overlap of fibres is chosen sufficiently large in order to avoid dead zones, fig. 3.5. The number of fibres in one column is chosen to achieve the required time resolution, which varies between 350 ps and 550 ps, and at the same time minimise the amount of material in the beam.

    The fibre's diameter goes to 0.5 mm to 1 mm and different fibre's stations have different orientation in order to measure different coordinates. Their spatial resolution goes from 130 μm to 210 μm, for the most downstream detectors and the intrinsic detection efficiency was measured to be $\sim 99\%$.

  - Silicon microstrip detectors are also placed upstream and downstream of the target and have a spatial resolution of 14 μm. Their time resolution is of the order of 3 ns. In each silicon wafer the readout strips on the n-side are perpendicular to the ones placed on the p-side, so that with one wafer two-dimensional position information can be obtained thus reducing the material budget by a factor of two as compared to a single-sided readout. Two detectors make up one silicon station. They are mounted back-to-back such that one detector measures the horizontal and vertical coordinates of a particle trajectory, while the other is rotated around the beam axis by 5°, providing two additional projections.

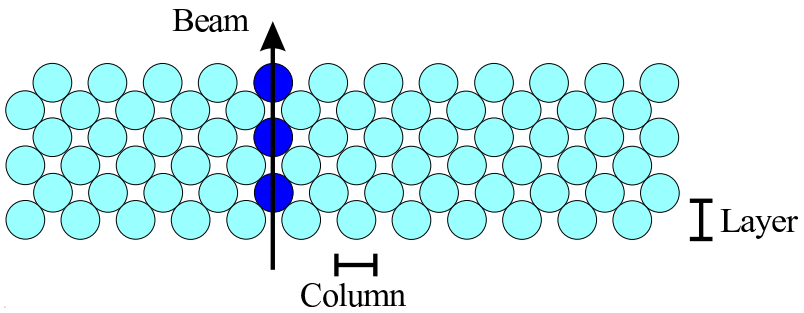

Figure 3.5: Fibre configuration of a SciFi plane (the actual number of fibre layers per plane is 8, 12 or 14, depending on the station).

- **Small Area Trackers (SAT)** The intermediate region at a radial distance of 2.5 cm to 30 - 40 cm is covered by the SAT. Two devices – MICROMEGAS (MICRO MEsh GAseous Structure) and GEM (Gas Electron Multiplier) detectors – are employed successfully for the first time in a large-scale particle physics experiment. Both are gaseous detectors where the zones of conversion and of amplification are separated and combine high rate capability (up to about 10^4 s^{-1} mm^{-2}), a good spatial resolution (better than 100 μm) with low material budget over fairly large sizes and an efficiency of $\sim 97\%$.

  – Micromega detectors are placed in the 1 m long region between the polarized target solenoid and the first dipole magnet SM1. The detector is based on a parallel plate electrode structure and a set of parallel microstrips for readout. A metallic micromesh separates the gaseous volume into two regions: a conversion gap where the ionisation takes place and the resulting primary electrons drift in a moderate field (1 kV/cm over 3.2 mm), and an amplification gap where a higher field (50 kV/cm over 100 μm) produces an avalanche which results in a large number of electron/ion pairs, see fig. 3.6.

  – GEM detectors are positioned along the whole spectrometer. Two detecors, one rotated by 45° with respect to the other, form one station resulting in the measurement of a charged particle trajectory in four projections. The central region of the detector is switched off during data taking, because of the high particle rate, and is activated during for run dedicated to the alignment. The GEM detector consist of three GEM amplification stages, shown in fig. 3.7, separated by thin spacer grids of 2 mm height and the GEM consists of a 50 μm thin Polyimide foil into which a large number of micro-holes has been chemically etched. Upon application of a potential difference of several 100 V across the foil, avalanche multiplication of primary electrons drifting into the holes is achieved when the foil is inserted between parallel plate electrodes of a gas-filled chamber. Suitable electric fields extract the electrons from the holes on the other side of the foil and guide them to the next amplification stage or to the readout anode.

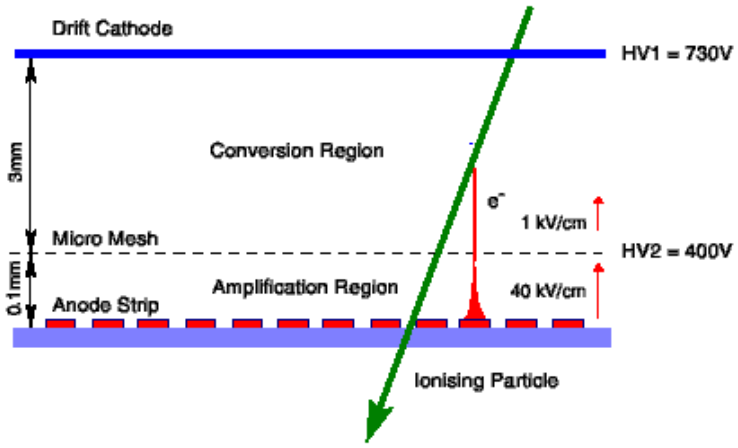

Figure 3.6: Principle of a Micromegas detector.

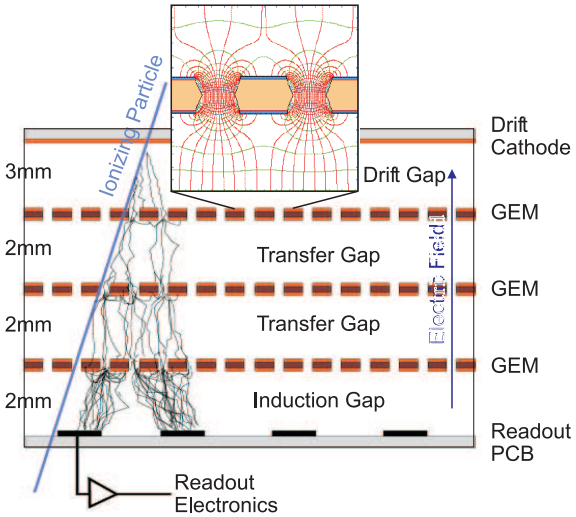

Figure 3.7: Schematic cross section of a triple GEM detector. The insert shows the electric field configuration for typical GEM voltages.

- **Large Area Trackers (LAT)** The reduced flux in the outermost regions allows the use of drift chambers straw tube chambers, and multiwire proportional detectors. The active area of these detectors is of the order of few m^2.

  – Drift chambers are positioned before and after SM1 and are able to measure 8 coordinates. The maximum drift time is 70 ns and the spatial resolution is 170 μm. Each plane composing the detector has an active area of 180×127 cm^2 and is characterized by an efficiency of $\sim 95\%$.

  – Straw tube drift chambers are used for the tracking of charged particles produced at large scattering angles ($15 - 200$ mrad) in the LAS downstream of SM1. The straw tubes are made of two layers of thin plastic films. The inner layer consists of a carbon loaded Kapton foil with a thickness of 40 μm and it is glued onto the second layer made of aluminised Kapton foil of 12 μm thickness. The diameter of the tubes is of 6 mm in the central region of the detector and 10 mm in its outer region. To resolve left-right ambiguities of a particle trajectory, each detector consists of two staggered layers of straws, which are glued together and mounted onto an aluminium frame. Each detector has an active area of about 9 m^2 and measures 3 coordinates with a spatial resolution varying from 200 μm to 300 μm.

  – Multi wire proportional chambers have the main role in the reconsruction of particles at large radial distance from the beam in the SAS. The wires used have length of ~ 1 m and a pitch of 2 mm. The spatial resolution is 500 μm and the active area is up to 180×120 cm^2 and the typical time jitter of the wire signal is about 80 ns.

  – The other two drift chambers of the spectrometer, $W4 - 5$, are placed after SM2 covering a 5×2.5 m^2 area and have a spatial resolution of 500 μm.

3.5 Particle identification

The Large Angle and Small Angle Spectrometers include several particle identification detectors. A RICH counter located in the first spectrometer (RICH-1) allows pions, kaons and protons identification, by measuring the particle velocity using the Cherenkov radiation emitted by charged particles. Two hadron calorimeters (HCAL1 and HCAL2) measure the energy of hadrons and provide a complementary trigger signal. An electromagnetic calorimeter (ECAL2) determines the energies of the photons and electrons emitted at small angles. Finally, in both LAS and SAS, scattered muons are detected in two muon wall systems (MW1 and MW2) both consisting of tracking detectors combined with a hadron absorber.

- **The muon detectors** The muon identification is performed by two detector systems made of a set of tracking stations and a hadron absorber followed by a second set of tracking stations. Such a structure permits to distinguish muons from track segments induced by the typical backgrounds like hadronic punch

through coming from the hadron calorimeters. The muon filtering system in the LAS consists of two stations MW1, separated by a 60 cm thick iron absorber. In the SAS the tracking behind SM2 is used in combination with a 2.4 m thick concrete absorber followed by two stations of MW2 and three MWPC stations

- **The Calorimetry** Two hadron calorimeters and one electromagnetic calorimeter are used: HCAL1 is placed at the end of the first stage of the spectrometer while ECAL2 and HCAL2 are a at the end of the spectroemter, before MW2. Both hadron calorimeters are sampling calorimeters having a sandwich structure: in HCAL1 Fe plates 25 mm thick are alternated with 5 mm of scintillator material; in HCAL2 Pb plates of 16 mm are placed as absorbers. Both hadron calorimeters measure the energy of hadrons produced in the target and participate in triggering on inelastic muon scattering events. At the beginning of each COMPASS data taking period, the calibration of both hadronic calorimeters is checked by using halo muons. The comparison between the energy deposited in the calorimeter and the momentum of the associated particle reconstructed by the spectrometer is shown in fig. 3.8, 3.9.

  ECAL2 is a homogeneous calorimeter consisting of lead glass blocks located before HCAL2 composed by 64×48 modules constitued by a lead glass block of $38 \times 38 \times 450$ mm^3. It serves to measure the energy of electromagnetic showers. The information coming from ECAL2 are not used in the standard analysis of the data collected up to 2004. In 2005 the electro magnetic calorimetry has been considerably improved: ECAL2 have been enlarged and a new calorimeter ECAL1 has been placed before HCAL1.

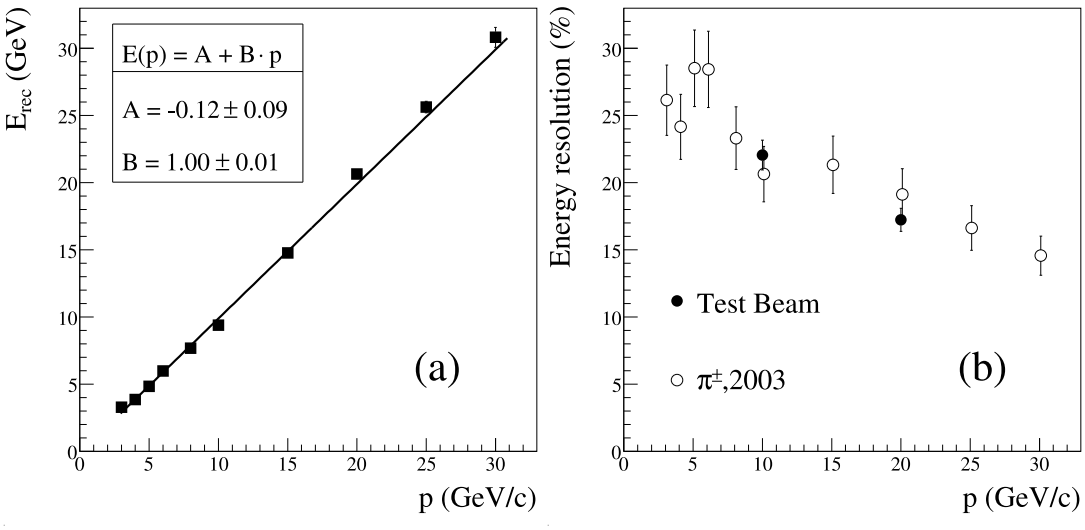

Figure 3.8: The energy measured by HCAL1 versus the momentum of particles reconstructed and identified as hadrons is shown in the left picture (**a**). The energy resolution as function of the momentum is shown in the right picture (**b**).

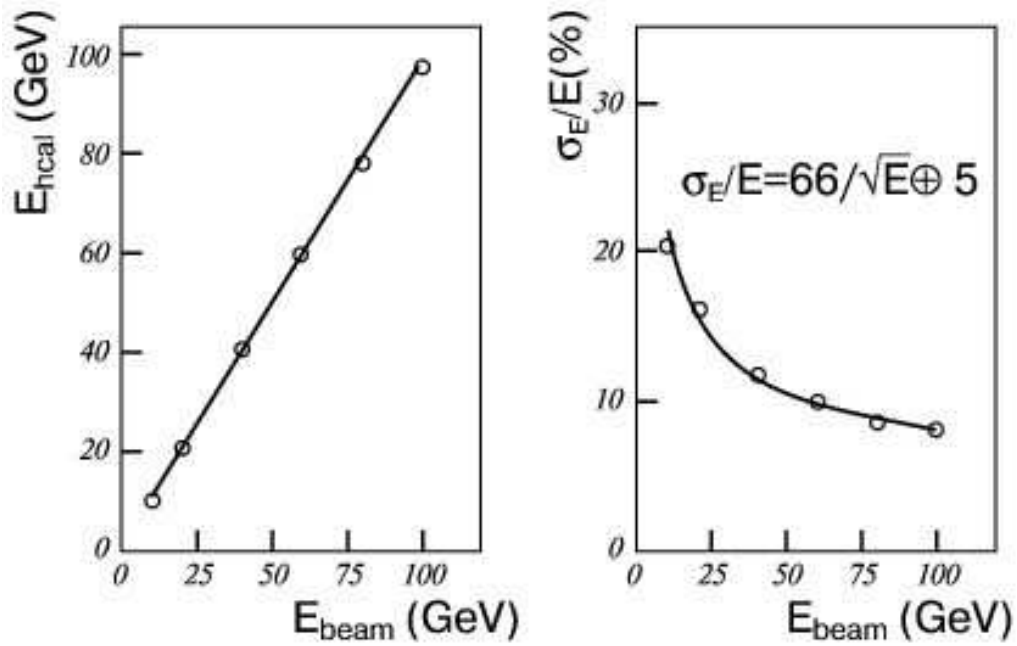

Figure 3.9: The energy measured by HCAL2 versus the momentum of the beam particles used for the calibration is shown in the left picture. The energy resolution as function of the momentum is shown in the right picture.

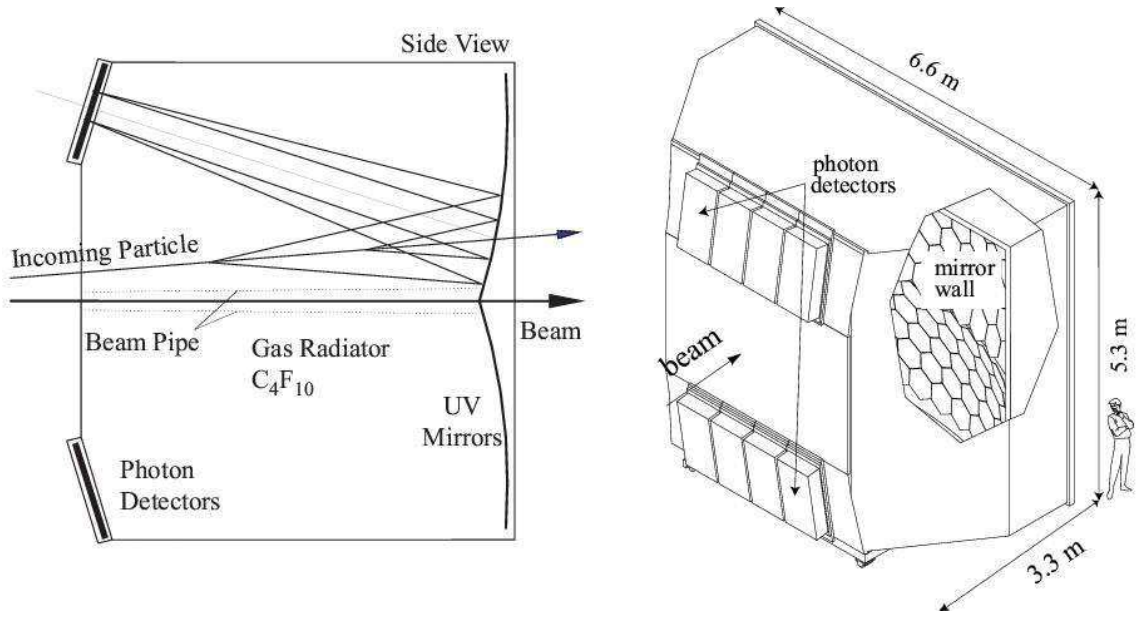

Figure 3.10: COMPASS RICH-1: at left, the principle of the detection of the Cherenkov radiation emitted by a charged particle crossing the gas radiator. An artistic view of the outer part of the vessel is also shown in the picture on the right.

- **The RICH detector** The COMPASS RICH-1 is a large-size Ring Imaging Cherenkov detector, installed at the end of the LAS, which performs hadron identification in a large momentum interval, from the Cherenkov threshold ($\sim$ 2.5 GeV/c for pions, $\sim$ 9 GeV/c for kaons and $\sim$ 17 GeV/c for protons) up to $\sim$ 50 GeV/c. It has large transverse dimensions (it covers the whole angular acceptance of the COMPASS LAS, i.e. $\pm$250 mrad in the horizontal plane and $\pm$180 mrad in the vertical plane), high-rate capability and introduces minimum material in the region of the spectrometer acceptance. Its large-volume vessel, shown in fig. 3.10, is filled with C_4F_{10} radiator gas. Cherenkov photons emitted in the gas are reflected by two spherical mirror surfaces. The photons are converted to electrons by the CsI photocathodes of eight MWPCs, which amplify the single photoelectrons and detect them. The characteristics of the RICH-1 detector allow to reach high efficiency and high purity in the hadron identification.

3.6 The trigger system

The trigger system has to select event candidates in a high rate environment with a decision time below 500 ns and with high efficiency. It is based on signals from hodoscopes of scintillating detectors, energy deposits in calorimeters and a veto system. A schematic representation of the trigger system is illustrated in fig. 3.11.

The triggered events are characterized by Q^2 values which span a large kinematical interval, ranging from $Q^2 \approx 0$, for the ΔG/G measurement to the maximum

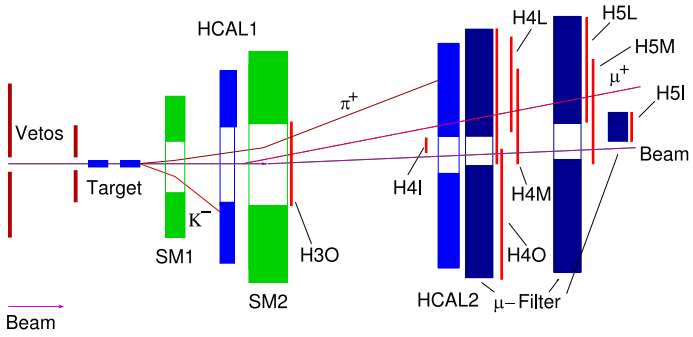

Figure 3.11: Schematic overview on the main hodoscopes trigger components.

allowed by kinematics (the DIS events are characterized by $Q^2 > 1$ (GeV/c)^2). Events with $Q^2 > 0.5$ (GeV/c)^2 are mainly triggered by using the scattered muon information only, extracted from two horizontal scintillator hodoscopes, in order to determine the projection of the muon scattering angle in the non-bending plane. The compatibility with the target position (vertical target pointing) is checked by using a coincidence matrix. To suppress the main source of noise due to halo muons, a veto system is added to the trigger system and it is shown in fig. 3.13.

At low Q^2, in the quasi-real photon regime, the muon scattering angles are close to zero so that target pointing does not work any longer. These events are selected by measuring the energy loss with two vertical scintillator hodoscopes using the bending of the muon track in the spectrometer magnets. The large background coming from processes such as elastic scattering off target electrons, elastic and quasi-elastic radiative scattering off target nuclei is reduced by requiring energy clusters in the hadronic calorimeters.

The hodoscopes of the trigger system are subdivided into four subsystems consisting of two hodoscope stations each, the IT (H4I, H5I), the LT (H4L, H5L), the MT (H4M, H5M) and the OT (H3O, H4O) (see fig. 3.12). The kinematical regions covered by each subsystem are shown in fig. 3.14. The IT (Inner Trigger), the LT (Ladder Trigger) and the MT (Middle Trigger) require also the information given by the hadronic calorimeters. The signal coming from HCAL1 and HCAL2 must be well above the one given by minimum ionizing particles such the halo muons. In fact the rate of halo muons crossing the active area of the calorimeters is high ($\sim 2 \cdot 10^7$ s^{-1}) and the probability to have pile up in the temporal window in which the calorimeters collect the signal is not negligible.

A trigger using only the hadronic calorimeter information (Calo Trigger or CT) has been used. In this case the threshold used to trigger on the event is higher than the one used when the calorimeter is combined with the hodoscopes. As can be seen in fig. 3.14 the CT allows to cover the large Q^2 region which is unreachable triggering on the hodoscopes. In 2006 and 2007 the information coming from ECAL1 has been also added in the trigger system.

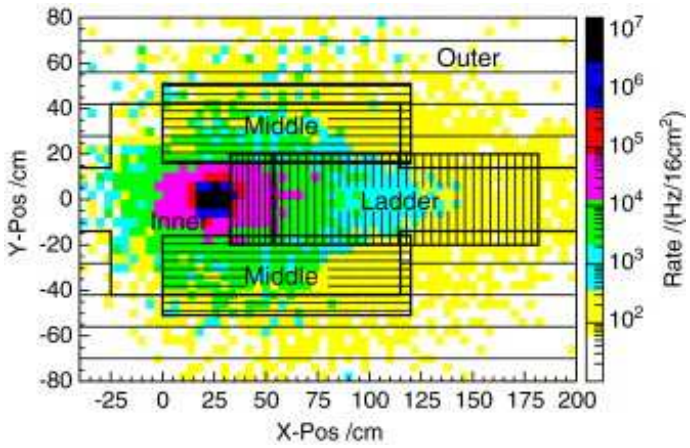

Figure 3.12: Schematic view of the hodoscopes stations of the different subsystems projected on the vertical YX plane. The size of the different hodoscopes are also indicated. The simulated beam rate is also shown (the beam comes perpendicular to the sheet).

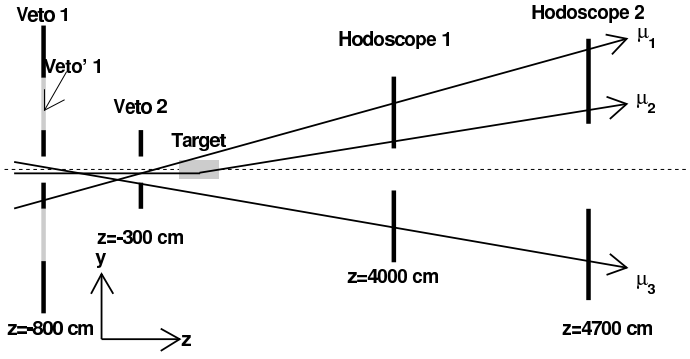

Figure 3.13: Veto schematic overview: only the track μ_2 fires the trigger.

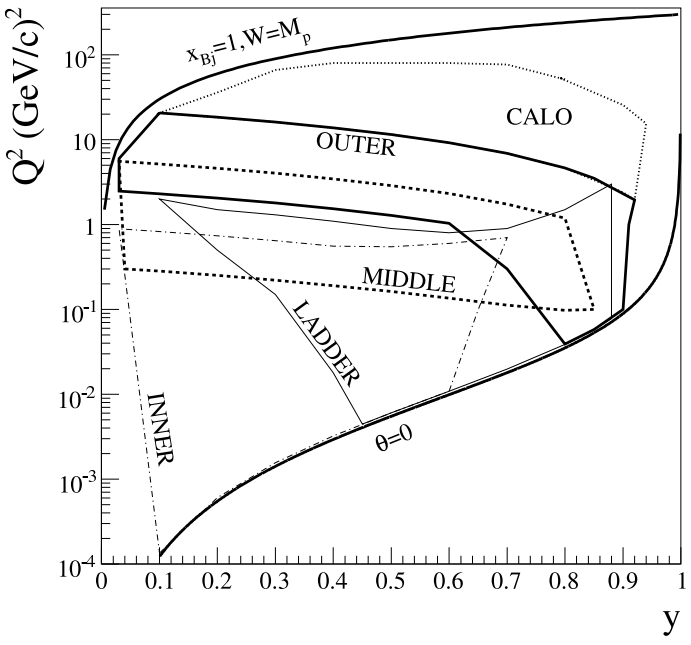

Figure 3.14: Coverage of the $Q^2 - y$ plane of the 5 trigger subsystems.

3.7 The data acquisition

The data acquisition system [50] was designed to read the 250 000 detector channels with an event rate of up to 100 kHz and with essentially no dead-time. This required a full custom design of the readout electronics (mounted directly on the detectors) and of the readout-driver modules (named CATCH and GeSiCA), which perform local event building and trigger distribution to the front-end boards (Fig. 3.15). The trigger control system (TCS) performs trigger distribution and synchronisation of the time-to-digital converters to better than 50 ps. The data collected during the 4.8 s spills is stored in 32 GByte buffers. The event building is performed on high performance Linux PCs connected to the read out system via Gigabit Ethernet. The data are grouped in "runs" corresponding to about 100 consecutive spills in 2002 and 2003 and 200 in 2004. General information on the run is extracted and stored in the meta-data tables of an Oracle database. The files are then sent to the Central Data Recording facility in the CERN computer centre in parallel multiple streams over a dedicated optical fibre network at an average speed of 70 MBytes/s.

Once at the computer centre, the files are registered in the name space of CASTOR (the CERN hierarchical storage management system): from this moment onward, CASTOR controls thoroughly the events data handling (copy to tape, managing of the disk space), while an Oracle RAC database system is in charge of translating high-level requests of data into file requests.

In the first three years of data taking, from 2002 to 2004 COMPASS collected 30 billion events, corresponding to a total data sample of more than 1 PByte. Because of the continuous work on alignment and improvement of the reconstruction code, these data have been efficiently processed several times at the CERN computing centre.

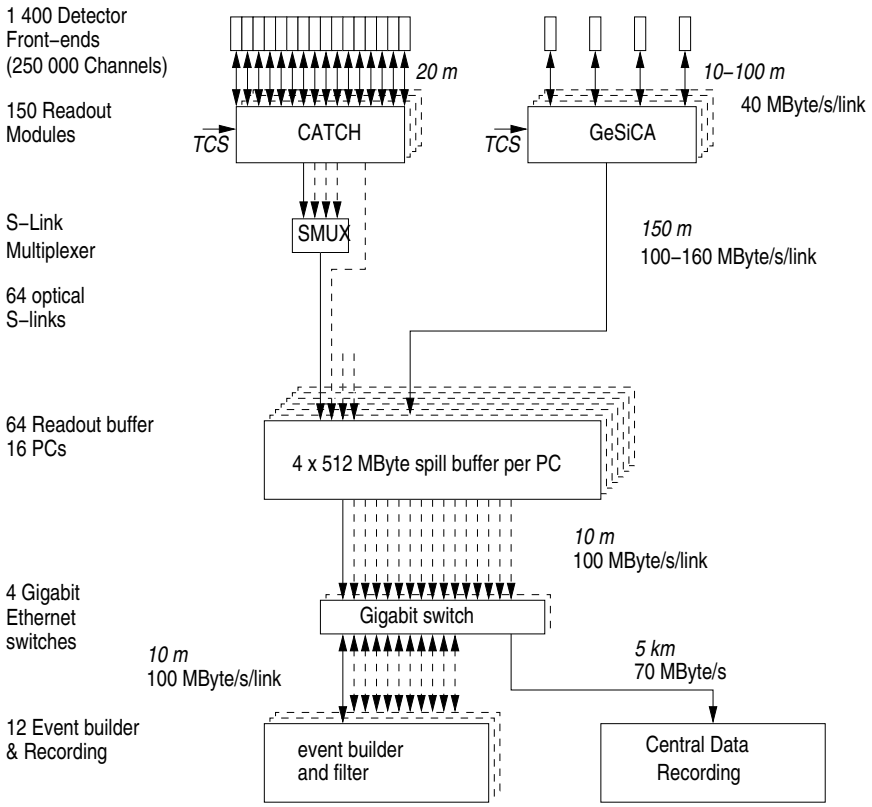

Figure 3.15: General architecture of the DAQ system.

Chapter 4

Data reconstruction and event simulation

4.1 The COMPASS offline system

The data files produced by the COMPASS acquisition software contain the raw information from the detectors digitised by the front-end electronics. This gives a huge amount of data of about 350 TBytes/year. The raw events are reconstructed at the batch system of the CERN computer centre, using a computing power of about 200k SPECint2000.

The event reconstruction is carried on by CORAL [52], the COMPASS reconstruction and analysis framework, a fully object oriented program with a modular architecture written in $C++$. CORAL performs the data decoding, the track and vertexes reconstruction and performs particle identification making use of the alignment and calibration data describing the apparatus, which are stored in a MySql database. The schematic representation of the COMPASS reconstruction software, describing the various steps performed and their mutual connections, is shown in fig 4.1. The input of the reconstruction software is represented either by the raw data collected by the experiment, or by the output of the Monte Carlo simulation software (see section 4.3.1). The geometrical position of each detector plane is retrieved from files that are generated either by the alignment procedure (performed on dedicated run during the data taking) or by the Monte Carlo package. In the decoding phase the information on the fired detector channel (either wire, pad or cell depending on the detector type) is extracted form the raw data. Then the detector channels that are fired by the same particle are grouped together by the clusterization and the geometrical coordinates of the cluster are calculated in the main reference system of the apparatus. The information from tracking detectors is used to reconstruct the trajectories of charged particles and hadrons calorimeters are used to separate muons from hadrons. The RICH-1 software package is used to perform hadrons identification using the information coming from the RICH detector. The results of the reconstruction phase is output in a proprietary format to files called Data Summary Tapes (DSTs), and in ROOT [53] format to mini-DSTs which are selectively filtered out from the DSTs during production. DSTs and miniDSTs are stored centrally on tape, under CASTOR. The physics analysis is performed on the

mini-DSTs, replicated and filtered according to the specific analysis requirements in the different Institutes, by means of PHAST [54], the COMPASS framework for the final data analysis.

4.2 Event reconstruction and SIDIS selection

The selection of the SIDIS events is similar for all the COMPASS analysis. Here the selection applied to the data taken during 2004 in the transverse spin configuration used to extract the unpolarized asymmetries analysis is described. This data sample has been used for the measurement of the Collins and Sivers asymmetries on deuteron, published in [26].

A first selection is applied at the end of the reconstruction and consists in writing on miniDSTs only events with at least one "incoming muon", one "scattered muon" and one "primary vertex", where the following definitions are used.

- Incoming muon. A beam track candidate is a track with an associated momentum measured in the BMS and reconstructed in the detectors before the target. These are the scintillation fibers and the silicons.

- Scattered muon. Good candidates are all positive tracks reconstructed after SM1 with a momentum higher than 1 GeV/c. Their extrapolations at the beginning and at the end of the target have both to be closer than 5 cm to the target axis. If the event is characterized by a scintillator hodoscopes based trigger, the reconstructed track has to be compatible with the hodoscopes hits as given in the corresponding trigger matrix. If the event is characterized by the calorimeter trigger alone the candidate track must have a minimum number of associated hits downstream of the hadron absorbers. To minimize hadrons contamination it is also requested that the track crosses a minimum amount of material.

- Primary vertex. Each primary vertex is defined to have one incoming muon and one scattered muon. The interaction point is then defined as the one with the minimum distance between the tracks associated to the vertex. The value of the minimum distance has to be less than $2 - 3$ mm. The best primary vertex can be chosen as the one with the maximum number of tracks.

The filtered mini-DSTs used in the analysis only contain the events with $Q^2 > 1$ $(\mathrm{GeV/c})^2$ with at least one primary vertex which has one or more additional associated tracks other than the scattered muon (reducing by a factor of 100 the size of the raw data). At this stage a selection is done on the data quality. The stability of the detectors is monitored by checking the the quality of the reconstruction, on spill per spill basis, and the kinematical distributions, on a run per run basis. The spills or runs which showed a different behaviour with respect to the general trend ($\sim 20\%$) have been rejected in order to have stable data.

Further cuts have been applied to the remaining events and are described in the following. To achieve a clean muon identification, the amount of material traversed in the spectrometer has to be larger than 30 radiation lengths. Only events with

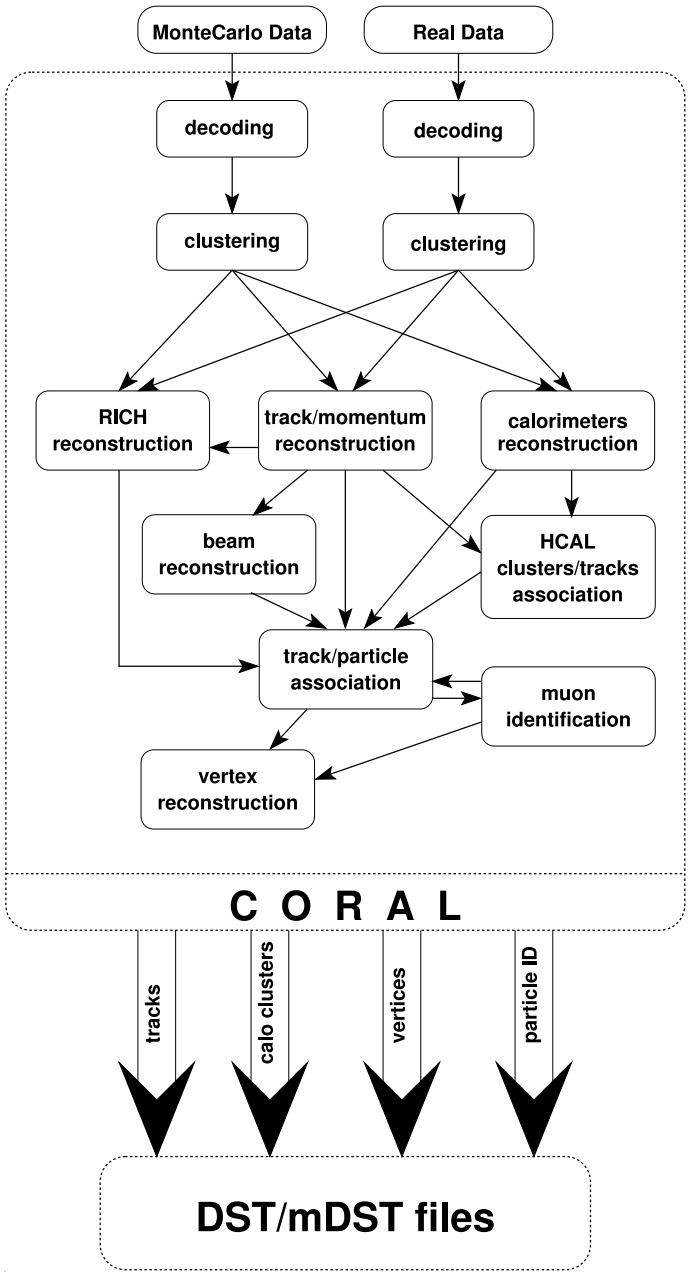

Figure 4.1: Schematic representation of the COMPASS reconstruction software. The data (real or simulated) are given in input and the information produced for every event are written on DST or mDST files. The various steps performed in the reconstruction are shown together with their mutual connections.

only one muon candidate enter the analysis. Then every other outgoing track from the primary vertex is considered an hadron if:

- at least one hit associated to the track belongs to a detector which is downstream of first magnet. This is in order to use all the SM1 field to measure its momentum;
- the amount of material traversed in the spectrometer has to be smaller than 10 radiation lengths;
- the transverse momentum of the particle with respect to the virtual photon direction has to be larger than 0.1 GeV/c, to have a good resolution on the azimuthal angle.
- the cut $z > 0.2$ has been applied to all hadron tracks in order to exclude particles coming from the target fragmentation region.

All the data taken form 2002 to 2004 in the longitudinal spin mode have been used for the measurement of the longitudinal azimuthal asymmetries. For historical reason the selection for the data quality used in this analysis is slightly different with respect to the one described before. Also no selection on the traversed material has been made nor for the scattered muon nor for the hadron and the information coming from both hadronic calorimeters has been used to select the hadrons track. This different selection will be described in details in chapter 7. The results obtained with the two data selection are consistent as shown in section 7.4.3.

Starting from the $Q^2 > 1(GeV/c)^2$ sample the typical DIS cuts have been applied:

- the cut $W > 5GeV/c^2$ excludes the region corresponding to the known nuclear resonances;
- $y > 0.1$ excludes elastic events and $y < 0.9$ in order to limit the error due to radiative corrections and to warrant a good determination of the scattered muon.

The position of the primary vertex is selected to be inside the target volume by means of a geometrical cut. The effect of this cut and the resolution of the coordinate along the nominal beam axis can be deduced from fig 4.2.

The kinematical distributions obtained after this selection (and starting from the sample used for the unpolarized asymmetries analysis) are shown in fig. 4.3. The Q^2 range is wide going up to ~ 100 (GeV/c)^2 and the explored x interval goes from very small values (0.004) to the quark valence region (~ 0.3). The correlation between the x and Q^2 variables is mainly induced by the cuts on y.

Different cuts, applied for the different analysis described in this thesis will be explained in chapters 5 and 7.

4.3 Event simulation

An extensive use of the Monte Carlo(MC) simulations has been done in the unpolarized asymmetries analysis. In particular the azimuthal acceptance of the apparatus,

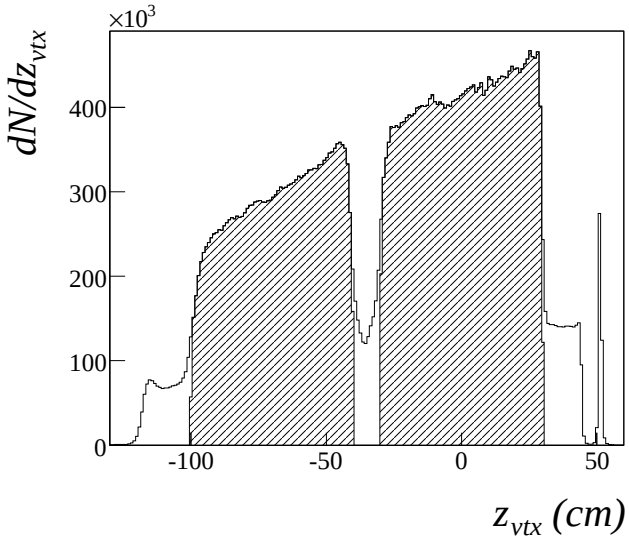

Figure 4.2: Distribution of the number of events having the Z coordinate, i.e. the nominal beam axis, of the interaction vertex. The cut applied to attribute one event to a given cell is also shown.

needed to correct the azimuthal hadron distributions, has been calculated by means of the MC simulations as it is described in chapter 5. Dedicated studies on the MC description of the COMPASS apparatus, as it was during the 2004 transverse data taking, have been described in [55]. Only the studies and the improvements made starting from that configuration are described in this thesis, in section 4.3.2 and chapter 5.

4.3.1 Software for the simulation

In COMPASS, the simulation of the events, from the elementary interaction to the tracking of the particles in the apparatus, is performed with a MC chain which links different softwares. These programs are built and developed inside the COMPASS collaboration and the output of each program is used as input for the following step.

The DIS event generation and the propagation of the tracks through the spectrometer is done independently and the last is performed by COMGEANT, a program interfaced to Geant 3.21 [56]. COMGEANT can be also linked to any external generator of lepton or hadron interactions such as Lepto [57], Aroma [58] or Pythia [59]. Radiative corrections can also be introduced in the generated events [60], although it is not clear which is the optimal way to simulate them. The track parameters used to generate beam and halo particles are extracted from dedicated measurement on the real data performed periodically. Both the trajectory of the particles produced in the final state of the event generation and the physical processes which the particles undergo inside the apparatus are simulated in COMGEANT. These are for example, the hadron decays, the multiple scattering, the ionization, the δ ray production and the interactions with both the passive and active material that builds the spectrometer. The detectors' response to the crossings of some particle is simulated at the best of the knowledge. The description of the geometry and of the

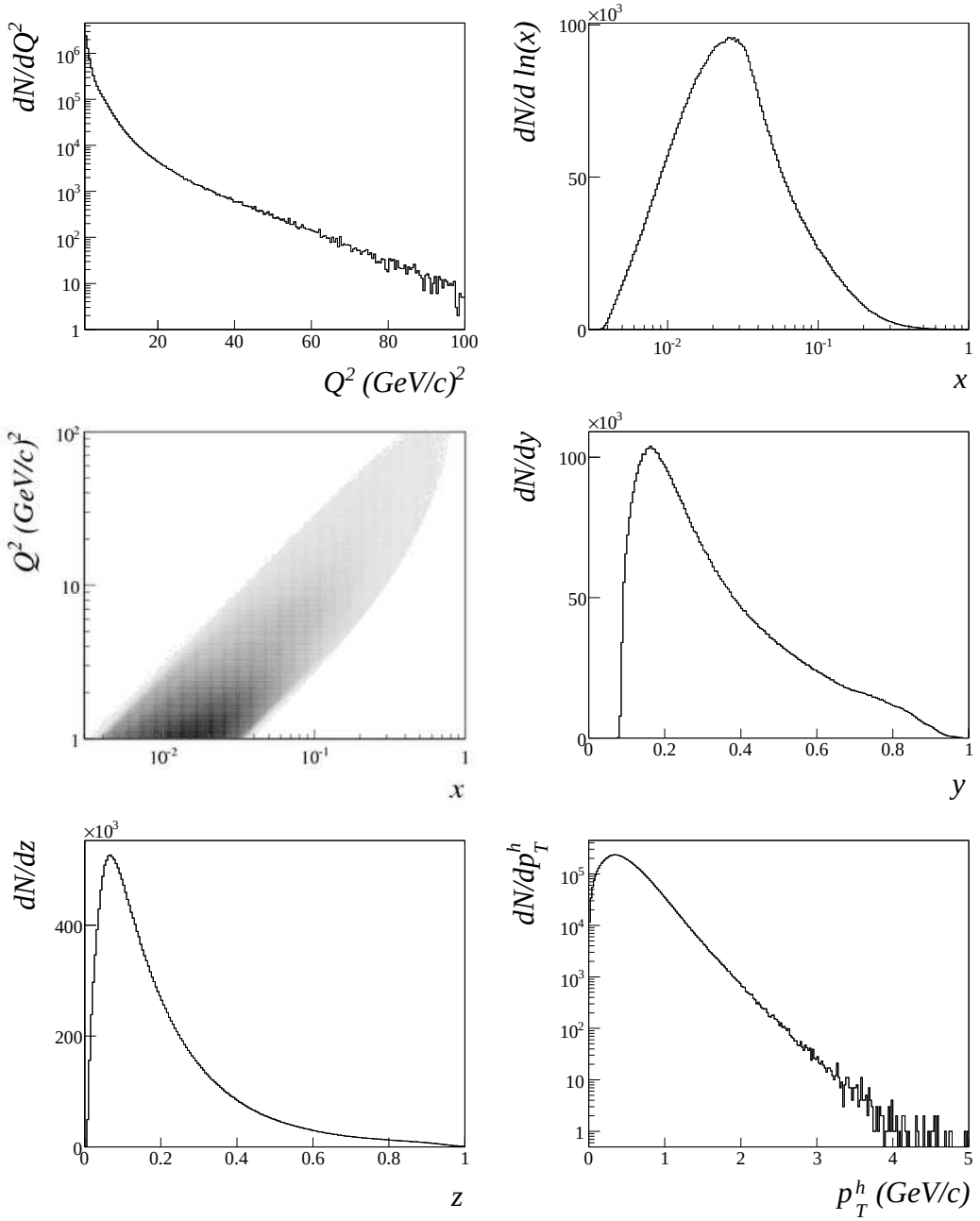

Figure 4.3: Distribution of the main kinematical quantities (Q^2, x, y, z e P_T) after the standard SIDIS cuts. The $x - Q^2$ correlation is mainly given by the cut $y > 0.1$, at large x, and by the cut $y < 0.9$, at low x.

materials of all the elements of the apparatus as well as the main parameters which characterize the behaviour of each detectors is extremely detailed. These quantities, like efficiencies, resolutions and thresholds, are measured from the real data and are given in dedicated option files which are continuously updated for each data taking year.

The main COMGEANT output is a *zebra* file (a binary file in a proprietary format) containing the results of the propagation of the particles through the spectrometer, the information given by the generator program and a text file with a simplified version of the description of the apparatus and of the geometry of the detectors. Both files are given as input to CORAL which performs the digitization and then the reconstruction in complete analogy to what happens for the real data.

The MC generator of the DIS event simulation chosen for the work described in this thesis is Lepto. It completely simulates the lepton nucleon deep inelastic scattering using the Standard Model cross section corrected for the perturbative QCD effects. The content of the nucleon is mainly described by the available unpolarized collinear PDF parametrization, based mainly on the DIS (lepton-nucleon) data both from fixed target experiments and from colliders. The quark fragmentation is implemented using the phenomenological LUND string model and the pQCD effects can be introduced by means of the parton showers. This program is widely used in the high energy physics and it has been proved to be the most reliable DIS generator, able to reproduce satisfactory the experimental data on the inclusive hadron production in DIS. The kinematical range, the type of lepton and target used and other parameters, concerning the different physical processes, can be changed. As a starting point for this work all the default values have been used.

The comparison between real and MC data distributions, after the standard SIDIS event selection is shown in fig. 4.4 and 4.5. The ratios between the real and MC data distributions are shown for the different kinematical variables. It can be seen that the y, Q^2, W, z and P_T^h measured distributions are reproduced by the MC. There are some disagreement for the shape of the x distribution, in the lower x region, and the ratio of the hadron polar angle θ_{lab}^h distributions has some slope in the small angle region. Anyway the overall picture is good enough for a first evaluation of the acceptance on the azimuthal angle of the hadron, for which a perfect agreement on the other kinematical distributions is not required. Different tunings have been tried inside the Collaboration, for the different analysis, in order to improve the agreement with the COMPASS data and have been also used for the measurement of the azimuthal asymmetries on the unpolarized deuteron target as described in chapter 5.

4.3.2 Monte Carlo studies

Reconstruction resolution

The values of the reconstructed physical quantities (the momenta of the detected particles) could be affected by the finite resolution of the detectors, or of the tracking procedure, and thus be different with respect to the real values. The effects on the main kinematical variables have been studies by means of the MC simulations where both the information on the generated and the reconstructed tracks are saved. The

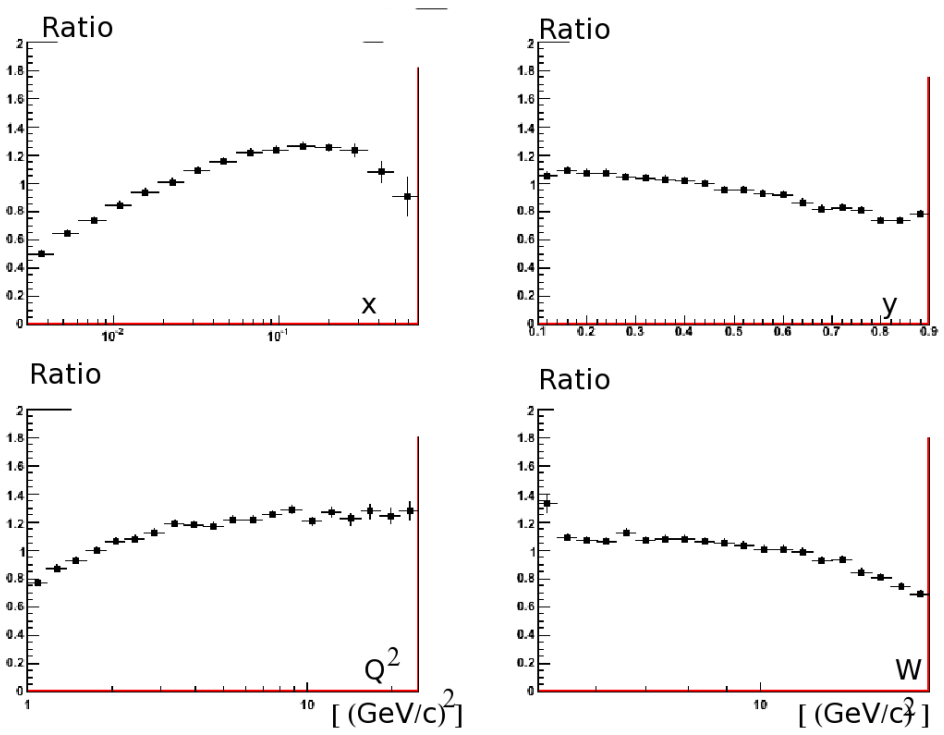

Figure 4.4: Ratios between the kinematical distributions calculated from the real data and the Monte Carlo data after the standard DIS cuts. The ratios for the event distributions of x, y, Q^2 and W are shown.

differences between the values of x, y, z and P_T^h calculated from the reconstructed particle momenta and the corresponding generated ones have been computed for every event (for x and y) or for every hadron (for z and P_T^h). The differences between the reconstructed and generated quantities divided by the reconstructed one ($x^{rec} - x^{gen}/x^{rec}$ and $y^{rec} - y^{gen}/y^{rec}$) are shown in the left plots of fig 4.6. The differences $x^{rec} - x^{gen}$ versus x^{rec} and $y^{rec} - y^{gen}$ versus y^{rec} are shown in the right part of fig 4.6. The same, but for z and P_T^h, is shown in fig 4.7. The mean values of the distributions are centred at zero and their RMS are less than 10%.

The distribution of the quantity $(\phi_h^{rec} - \phi_h^{gen})$ (calculated from the reconstructed and the generated tracks) and $\phi_h^{rec} - \phi_h^{gen}$ versus ϕ_h^{rec} are shown in fig. 4.8. Here most of the hadrons have a $(\phi_h^{rec} - \phi_h^{gen})$ difference smaller than 0.4 rad and this is the size of the bins used to build the ϕ_h histograms for the analysis of the azimuthal asymmetries on the unpolarized target described in chap. 5.

The effect of the smearing has also been studied and it is presented in chapter 5.

Studies of the tracks at $\phi_h \simeq 0$

The measured ϕ_h distribution has a small peak in the $\phi_h \simeq 0$ region, which is not reproduced by the corresponding distribution obtained from the Monte Carlo sample (fig. 4.9). These particles are produced around the direction of the scattered muon with an angular distribution peaked in the very forward direction. No particular correlation has been found with the event kinematics but the effect is more evident

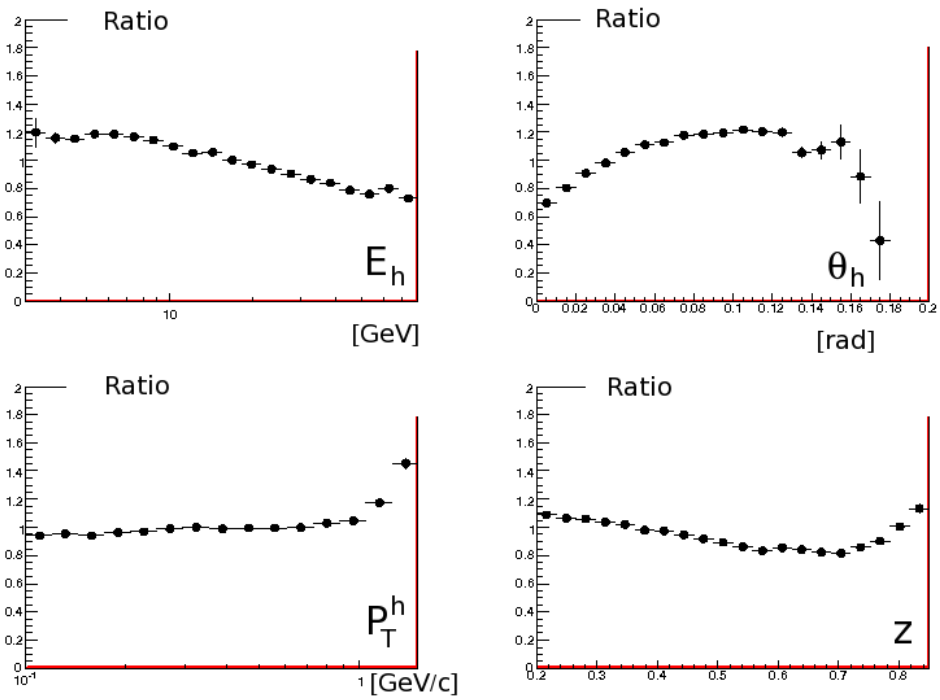

Figure 4.5: Ratios between the kinematical distributions calculated from the real data and the Monte Carlo data after the standard DIS cuts. The ratios for the hadron distributions of the momentum E^h_{lab}, of the polar angle θ^h_{lab}, of z and P^h_T are shown.

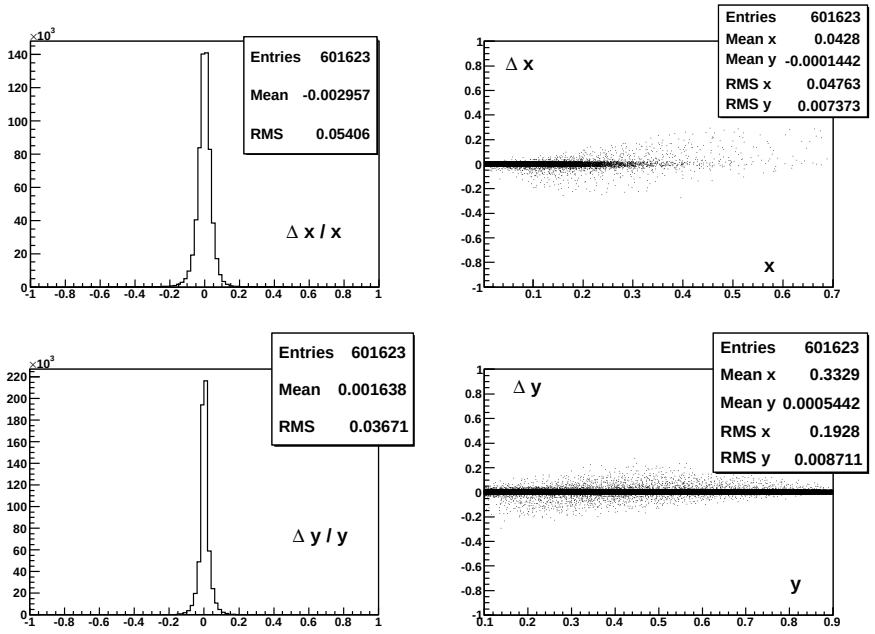

Figure 4.6:

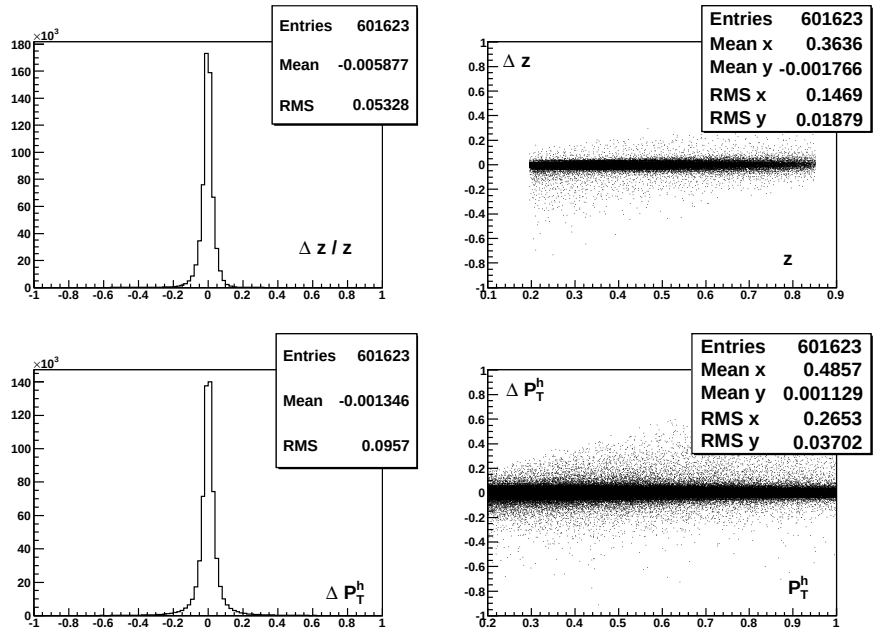

Figure 4.7:

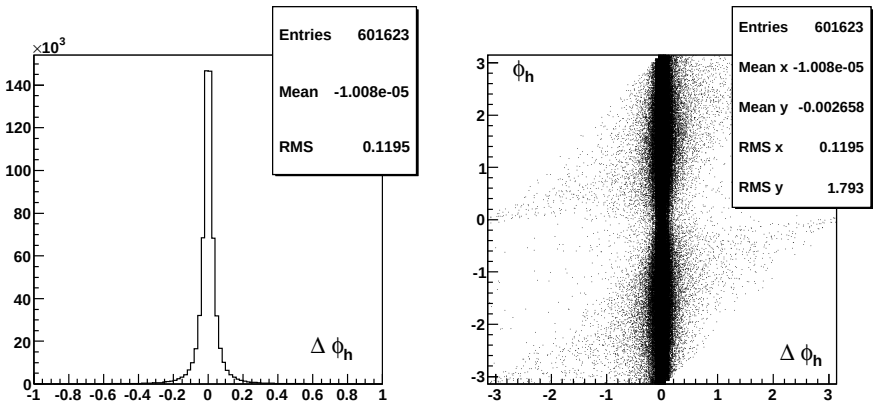

Figure 4.8:

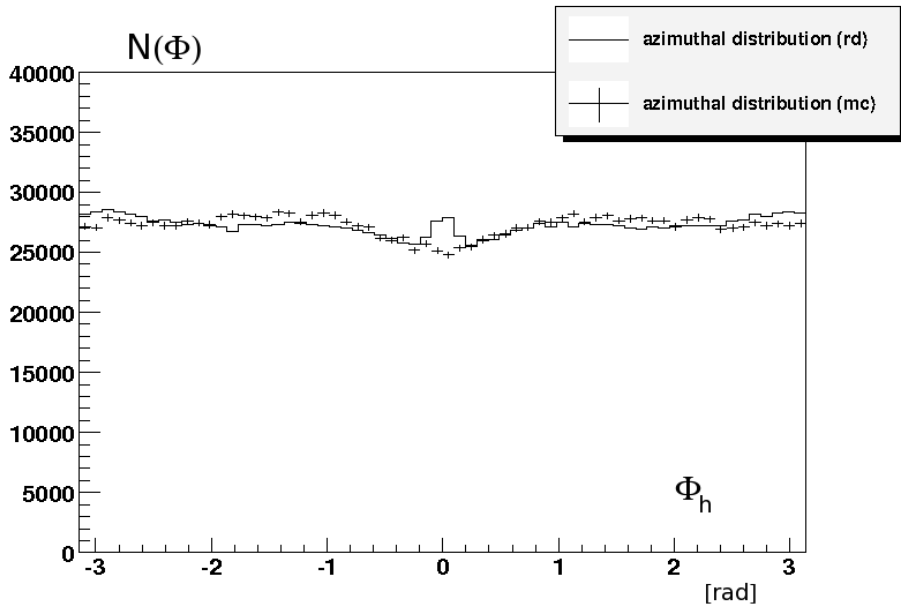

Figure 4.9: Measured (histogram) and MC (points) ϕ_h distributions. The peak in the $\phi_h \simeq 0$ region is visible only in the real data.

for hadrons produced at small polar angle, $\theta^h_{lab} < 20$ mrad. In fig. 4.10 the ratio between the ϕ_h distributions obtained from data and Monte Carlo are shown for $\theta^h_{lab} < 20$ mrad and $\theta^h_{lab} > 20$ mrad: in this last case the peak disappears.

Several studies have been done to identify a clear signature of the effect. An important result was found studying the azimuthal distribution of the particle identified as electrons using the information coming from the RICH detector. This detector is optimized to identify π up to $\simeq 60$ GeV and to allow a good separation between π and K. The electron identification is possible only for tracks with momenta below roughly 7 GeV as shown in fig. 4.11 where the Cherenkov angle reconstructed using the RICH and associated to the track is plotted versus the momentum of the track. The electrons are expected to give an horizontal band at $\simeq 54$ mrad of the Cherenkov angle which cannot be distinguished from the π band at higher momenta. The azimuthal distribution given by the tracks with Cherenkov angle between 52 and 58 mrad and momentum below 7 GeV/c is shown in fig. 4.12. The peak around $\phi_h = 0$ is clearly visible. The contamination of electrons in the hadron sample has been evaluated to be $\sim 5\%$ with the MC, which is consistent with a rough estimation of the ratio between the events in the peak and the ones around 0.

Other studies have been made trying to characterize those tracks with kinematical or topological cuts. The dependence of the shape of the measured azimuthal distributions, calculated separately for each trigger, shows that the peak is less evident for the events characterized by the CALO trigger, for which a signal from the large angle hadronic calorimeter is required (section 3.6 in chapter 3). This requirement is similar to cut away the tracks which go in the small polar angle region. Other tests, trying to exclude the cases in which the photon conversion happens

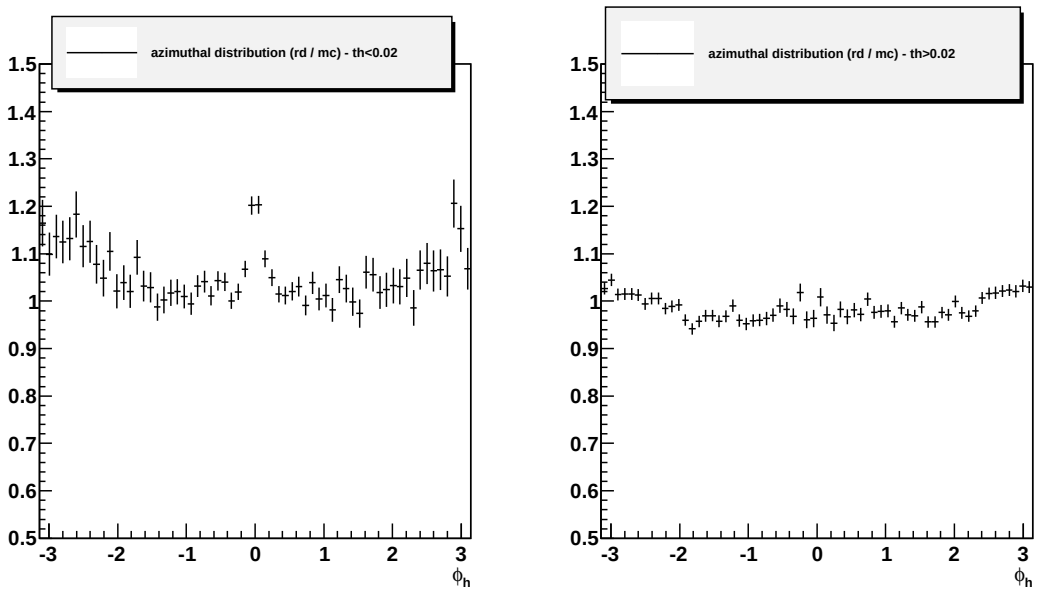

Figure 4.10: The ratio between the ϕ_h distributions obtained from data and Monte Carlo are shown for $\theta^h_{lab} < 20$ mrad (left plot) and $\theta^h_{lab} > 20$ mrad (right plot): in this last case the peak disappears.

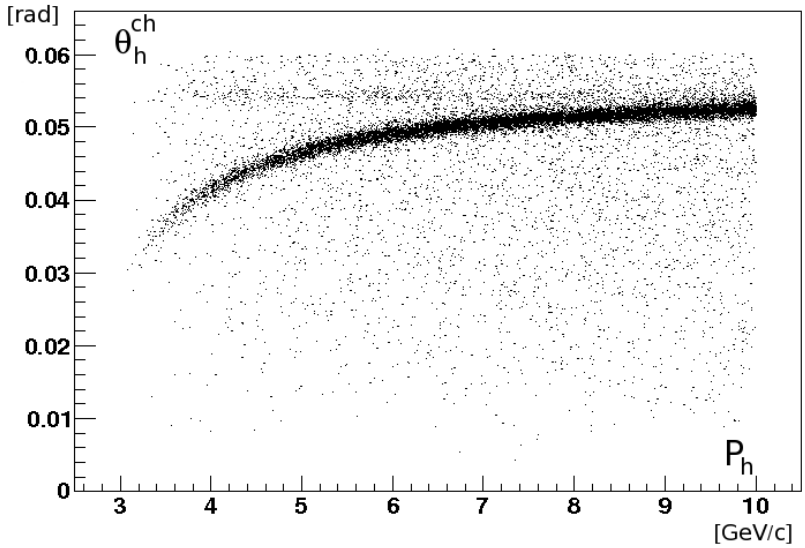

Figure 4.11: Cherenkov angle reconstructed using the RICH (associated to the track) plotted versus the momentum of the track. The electrons are expected to give an horizontal band at $\simeq 54$ mrad of the Cherenkov angle.

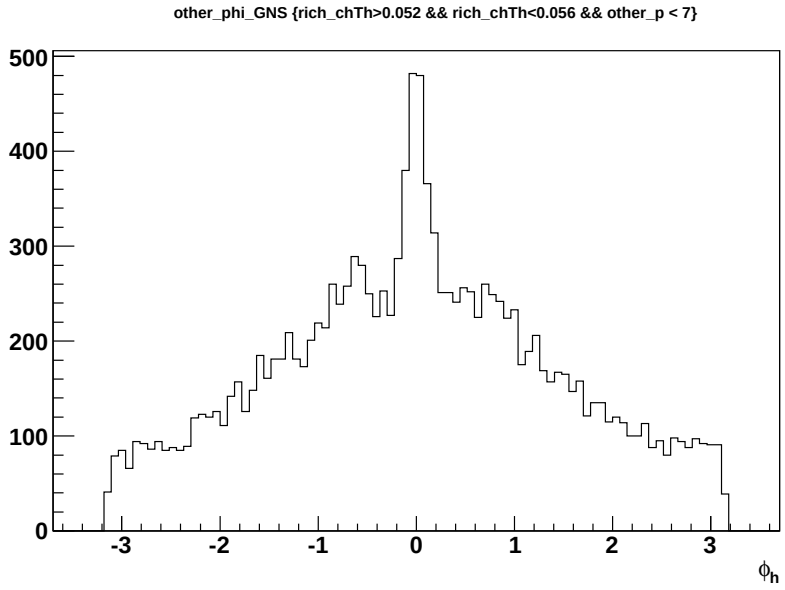

Figure 4.12: The azimuthal distribution given by the tracks with Cherenkov angle between 52 and 58 mrad and momentum below 7 GeV/c. The peak around $\phi_h = 0$ is clearly visible.

inside the target, but asking that the SIDIS interaction happens in the most downstream part of the target and asking that the first measured hit associated to the track must be given by a detector positioned before the first bending magnet SM1, have not allowed to isolate those tracks.

The tracks which give that particular shape around $\phi_h = 0$ have been finally identified as electrons or positrons coming from the conversion, mostly in the target region, of real photons produced in the SIDIS reaction. Both Brehmstralung and photon conversion are fully simulated in COMGEANT, but the emission of a hard real photon in the DIS, also called radiative effect, is not simulated in LEPTO. Such electrons are indeed expected to be mostly produced at small polar angle, along the scattered muon direction.

The only effective cut to exclude the peak is on the angular acceptance of the hadron tracks, asking $\theta^h_{lab} > 20$, but it has a large effect on the shape of the hadron azimuthal distribution, as shown in fig. 4.13. Such a big distortion should be avoided when measuring small effects in the amplitudes of the azimuthal modulations, in particular when the measured distributions have to be corrected by the acceptance effects. Finally the ϕ_h bins around zero have simply been excluded in the extraction of the azimuthal asymmetries on the unpolarized target described in chap. 5.

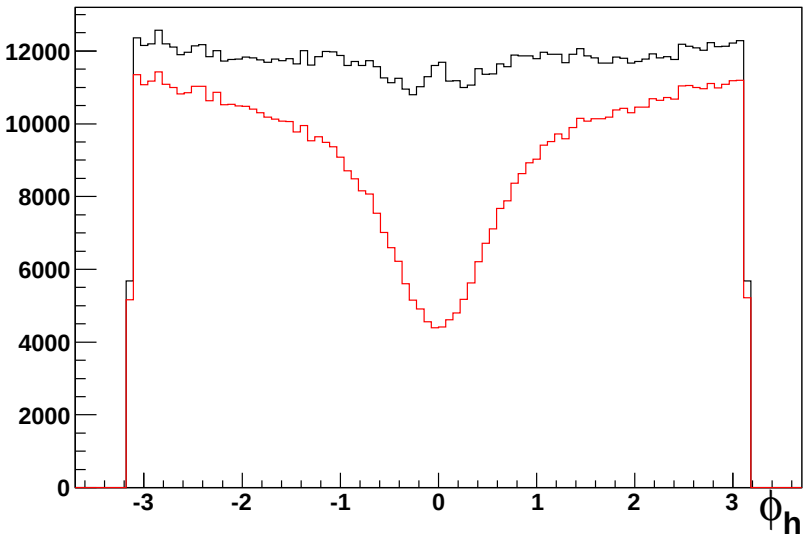

Figure 4.13: Measured ϕ_h distribution after the standard SIDIS cuts (black) and adding the $\theta^h_{lab} > 20$ cut (red) which induces a strong deep in the central part of the ϕ_h interval.

Chapter 5

Measurement of the azimuthal asymmetries on unpolarized target

As explained in chapter 2 the cross section of SIDIS off an unpolarized target allows for three independent azimuthal modulations: $cos\phi_h$, $cos2\phi_h$ and $sin\phi_h$, where ϕ_h is the azimuthal angle of the final state hadrons with respect to the scattering plane, as measured in the gamma-nucleon system. It can be expressed as

$$\frac{\mathrm{d}\sigma}{\mathrm{d}x\,\mathrm{d}y\,\mathrm{d}z\,\mathrm{d}\phi_h\,P_T^h\,\mathrm{d}P_T^h} = \frac{\alpha^2}{xyQ^2}\frac{(1+(1-y)^2)}{2}\cdot A_0\cdot\Big(1+\epsilon_1(y)A_{\cos\phi_h}\cos\phi_h + \\ +\epsilon_2(y)A_{\cos 2\phi_h}\cos 2\phi_h + \lambda_l\epsilon_3(y)A_{\sin\phi_h}\sin\phi_h\Big)\,, \qquad (5.1)$$

where λ_l is the longitudinal polarization of the incident lepton,

$$\epsilon_1 = \frac{2\cdot(2-y)\sqrt{1-y}}{1+(1-y)^2},\;\; \epsilon_2 = \frac{2\cdot(1-y)}{1+(1-y)^2},\;\; \epsilon_3 = \frac{2\cdot y\sqrt{1-y}}{1+(1-y)^2}\,, \qquad (5.2)$$

and $A_{\cos\phi_h} = \frac{F_{UU}^{\cos\phi_h}}{F_{UU}}$, $A_{\cos 2\phi_h} = \frac{F_{UU}^{\cos 2\phi_h}}{F_{UU}}$, $A_{\sin\phi_h} = \frac{F_{UU}^{\sin\phi_h}}{F_{UU}}$, using the notation of eq. 2.6 in chapter 2.

The measurement of the amplitudes $A_{\cos\phi_h}$, $A_{\cos 2\phi_h}$, and $A_{\sin\phi_h}$ as functions of the kinematics gives information on the structure of the nucleon and allows to access the quark transverse momentum distribution and the Boer-Mulders function. The interest of these azimuthal modulations has been already pointed out in chap. 2.

The COMPASS measurement, described in this thesis, has been done using the data collected in 2004 with the transversely polarized ^{6}LiD target. To minimize the effect of the acceptance of the polarized target solenoid, only the events with primary vertex in the downstream target cell have been used and the data collected with opposite polarization have been combined in order to cancel out possible effects due to the single spin azimuthal asymmetries.

After a first extraction of the asymmetries in 2008, briefly described in section 5.1, the analysis has been considerably improved as described in the remaining of this chapter. The new method for the corrections due to the apparatus acceptance is introduced in section 5.2. The MC studies of the acceptance and the new kinematical cuts are described in section 5.3.2, while section 5.4 is dedicated to the asymmetries

extraction method used to produce the final results given in chapter 6. The study of systematic effects and the final systematic errors are described in section 5.5.

Most of the work presented in this chapter has been done on the data collected in 2004 with the transversely polarized target. The results obtained from part of the data collected with the longitudinal polarized ^{6}LiD target in 2004 and 2006 are discussed in sections 5.5.7 and 5.6 respectively.

5.1 First extraction of the azimuthal asymmetries

The first preliminary COMPASS results for the azimuthal asymmetries have been produced in 2008 [61] for positive and negative hadrons separately using the data collected in 2004 with the transversely and longitudinal polarized ^{6}LiD target. The hadrons were selected requiring

- $Q^2 > 1$ GeV^2 ,
- $W > 5$ GeV/c^2 ,
- $0.1 < y < 0.9$,
- $0.1 < P_T^h < 1.5$ GeV/c,
- $0.2 < z < 0.85$,

where $z < 0.85$ cuts out the exclusive hadrons production and $P_T^h < 1.5$ GeV/c to select the small P_T^h region where the dominant contributions to the amplitudes of the azimuthal modulations should come from the intrinsic transverse momentum of the quark. These cuts have also been used as a starting point for the work presented in this thesis.

The amplitudes of the azimuthal modulations are extracted binning alternatively the data in the kinematic variables x, z, and P_T^h. The amplitudes A_i are extracted separately from the azimuthal distribution of positive and negative hadrons in every kinematical bin. Each distribution has to be corrected for the acceptance (and efficiency) of the apparatus which may also introduce azimuthal modulations. The resulting distributions are then fitted with a function of ϕ_h containing at least all the modulations which appear in the cross-section.

The critical point of these measurements is the evaluation of the possible effects introduced by the acceptance which have to be evaluated by means of Monte Carlo simulations. These measurements are more difficult than those of the spin dependent azimuthal asymmetries, since the azimuthal acceptance does not cancel. On the other hand, only possible modulations in ϕ_h in the acceptance are relevant and there is no need to know any absolute normalization.

The simplest procedure to extract the amplitudes of the azimuthal modulation in a specific kinematical bin is illustrated in the following. The azimuthal acceptance ($Acc(\phi_h)$) is calculated from the ratio

$$Acc(\phi_h) = \frac{N_{rec}^{mc}(\phi_h)}{N_{gen}^{mc}(\phi_h)}, \tag{5.3}$$

where $N^{mc}_{rec}(\phi_h)$ is the hadron azimuthal distribution coming from the reconstructed MC events and $N^{mc}_{gen}(\phi_h)$ is the corresponding generated distribution. The measured azimuthal distribution $N^m(\phi_h)$ is then corrected for the acceptance by making the ratio

$$\frac{N^m(\phi_h)}{Acc(\phi_h)} = N^{corr}(\phi_h). \tag{5.4}$$

and the amplitudes of the three azimuthal modulations are extracted by fitting the $N^{corr}(\phi_h)$ distribution using the function:

$$p_0 \cdot (1 + p_1 \cos(\phi_h) + p_2 \cos(2\phi_h) + p_3 \sin(\phi_h)) \tag{5.5}$$

where p_0, p_1, p_2 and p_3 are four free parameters. As an example the measured azimuthal distribution $N^m(\phi_h)$ and the corresponding corrected azimuthal distribution $N^{corr}(\phi_h)$, together with the fitting function, are shown in fig. 5.1 for the bin $0.64 < P_T^h < 0.77$ GeV/c.

This method is very simple, and its results are easy to be checked. It has been used in the first analysis to produce the results, shown at TRANSVERSITY 2008 [61], which for the first time were obtained for positive and negative hadrons separately. As can be seen in fig. 5.2, where the measured asymmetries are given as functions of x, z and P_T^h, both $A_{\cos\phi_h}$ and $A_{\cos 2\phi_h}$ turned out to be different from zero, with a strong dependence on the kinematical variables and different for positive and negative hadrons.

The interest for these results, and the non negligible estimated systematic errors motivated the further work described in the following.

In particular, the method used in the first analysis to correct the azimuthal distributions for the apparatus acceptance implies an implicit integration over all the other kinematical variables both in the acceptance calculation and the asymmetry extraction which could lead to biased results. A detailed discussion on the procedure to take into account possible dependencies of the acceptance from the kinematics is presented in the next section.

5.2 Acceptance corrections

The effects of the apparatus acceptance on the hadron azimuthal distribution can depend on the kinematical variables. In general the number of hadrons can be written as:

$$N^m(\phi_h, \vec{x}) = N^M(\phi_h, \vec{x}) \cdot A(\phi_h, \vec{x}) \tag{5.6}$$

where $N^M(\phi_h, \vec{x})$ is the true hadron distribution given by the SIDIS cross-section and $A(\phi_h, \vec{x})$ is a function which describes the apparatus acceptance and efficiency. The vector $\vec{x}$ stands for independent kinematical variables on which the response of the apparatus and the cross-section depend. Thus one possible choice for $\vec{x}$ would be x, y, z and P_T^h. However it is reasonable to assume that the strongest dependence would be on the variables calculated in the laboratory system such as the energy

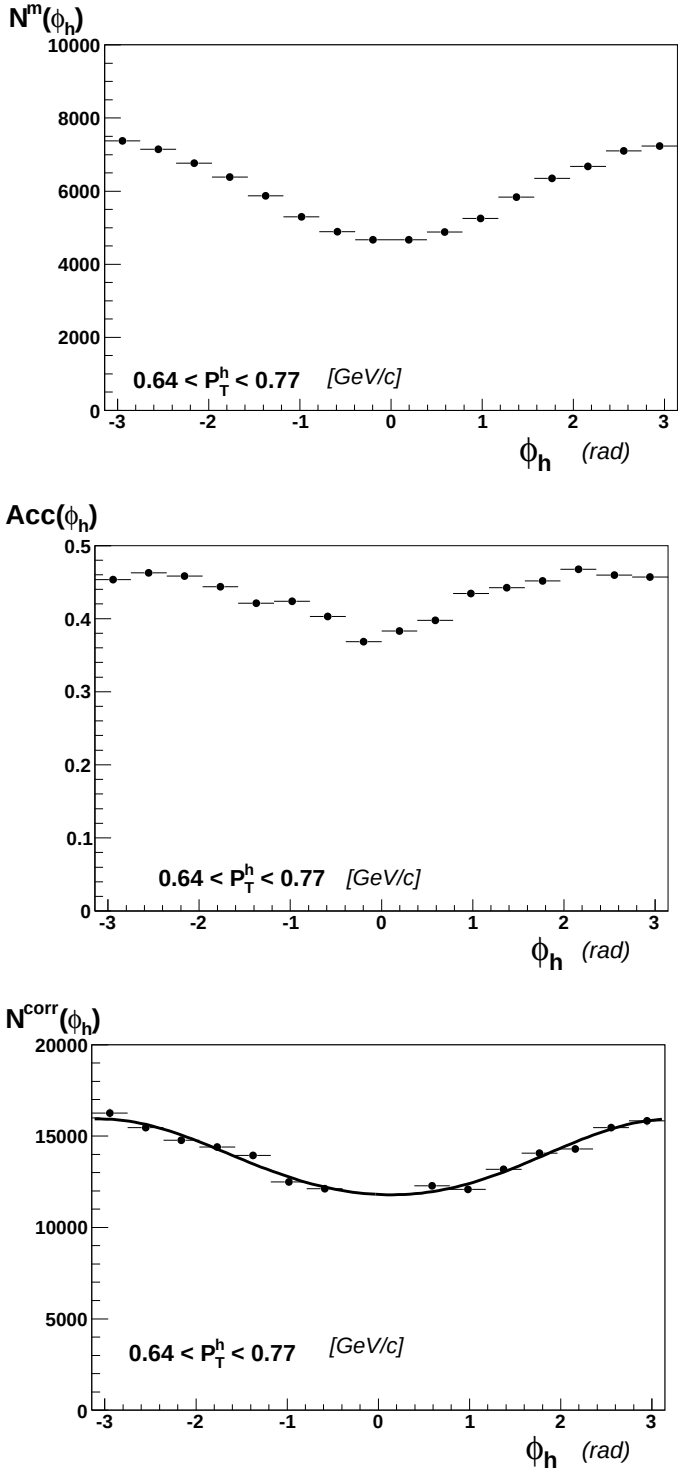

Figure 5.1: . The measured azimuthal distribution $N^m(\phi_h)$ (top plot), the azimuthal acceptance $Acc(\phi_h)$ calculated from the ratio $N^{mc}_{rec}(\phi_h)/N^{mc}_{gen}(\phi_h)$ (middle plot) and the measured azimuthal distribution corrected by the acceptance $N^{corr}(\phi_h) = N^m(\phi_h)/Acc(\phi_h)$ (bottom plot), calculated in a given bin of P_T^h are shown.

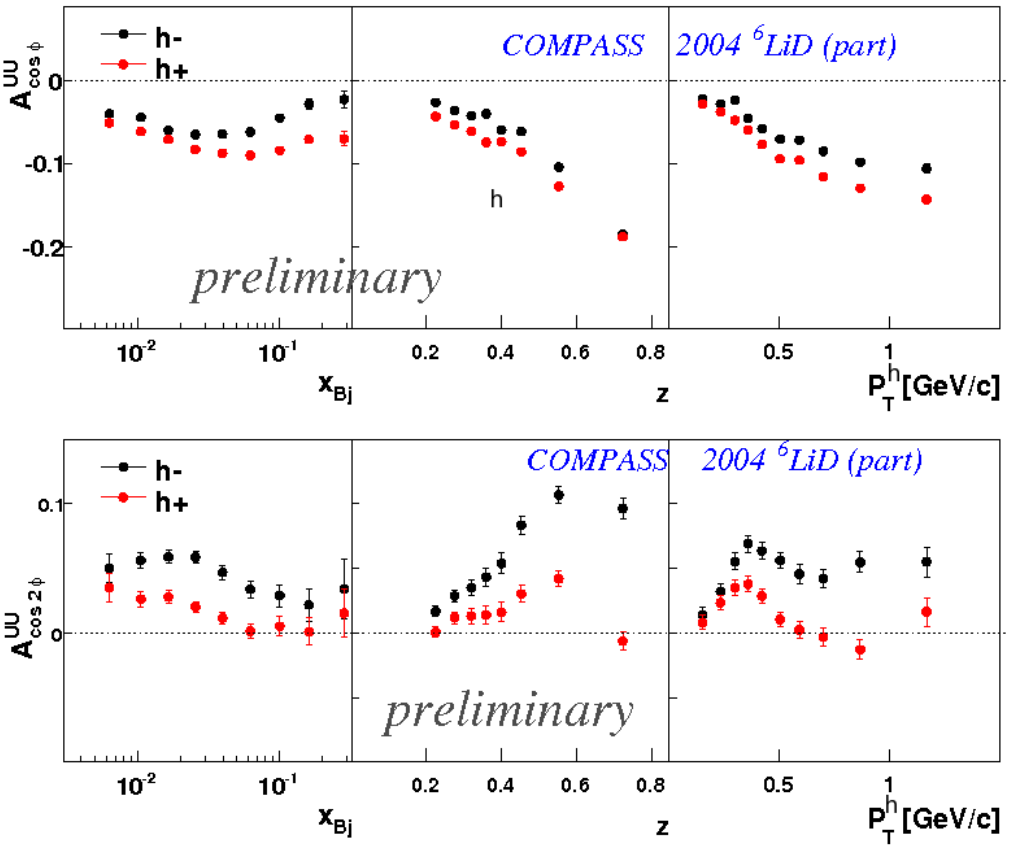

Figure 5.2: First results [61] of the azimuthal asymmetries on the unpolarized target produce for positive (black points) and negative (red points) hadrons separately. The results for $A_{\cos\phi_h}$ are shown on top and the ones for $A_{\cos 2\phi_h}$ are shown in the bottom plot. For both the amplitudes the measured signal is different from zero and strongly dependent from the kinematical variables. Moreover a dependence from the hadron charge is also present.

and the polar and azimuthal angles of the scattered muon and of the hadrons. Such dependencies can be diluted when considering the standard SIDIS variables.

To measure the amplitudes of the azimuthal modulations one should use the ratio $N^m(\phi_h, \vec{x})/A(\phi_h, \vec{x})$ between the measured hadron azimuthal distribution and the azimuthal acceptance, both extracted as functions of all the variables. This would lead to a complex analysis, starting from the huge number of bins required ($\simeq 10^4$, assuming 10 bins in each variable) and the consequent number of distributions to control. It is essential to reduce this complexity. In the following it is explained how the problem has been addressed and how the kinematical dependence of the acceptance has been investigated.

To keep the analytical calculations simple, we assume that only a $cos\phi_h$ modulation is present in both N^m and A and effects up to the first order in the amplitudes of the azimuthal modulation are considered. Also, we assume $\vec{x} = (x_1, x_2)$, a specific bin in x_1 is considered and the possible dependence of the acceptance on the other independent kinematical variable x_2 is discussed. In the following, the dependencies on x_1 are not given explicitly.

In this case the hadron distribution and the acceptance can be written as:

$$\begin{aligned} N^m(\phi_h, x_2) &= N_0(x_2) \cdot (1 + \epsilon(x_2) \cdot \cos\phi_h) \\ A(\phi_h, x_2) &= A_0(x_2) \cdot (1 + \alpha(x_2) \cdot \cos\phi_h). \end{aligned} \tag{5.7}$$

The amplitude of the azimuthal modulation ϵ is then extracted from the measured distribution corrected by the acceptance

$$N^C(\phi_h) = \frac{\int N^m(\phi_h, x_2) \cdot A(\phi_h, x_2))dx_2}{\int A(\phi_h, x_2)dx_2}. \tag{5.8}$$

Substituting equations 5.7 in eq. 5.8, keeping the terms up to the first order in the amplitudes α and ϵ (using $1/(1+\varepsilon) \simeq 1 - \varepsilon$), the corrected azimuthal hadron distribution can be written as:

$$\begin{aligned} N^C(\phi_h) &= \frac{\int dx_2\, N_0(x_2) \cdot \{1 + \epsilon(x_2) \cdot \cos\phi_h\} \cdot A_0(x_2) \cdot \{1 + \alpha(x_2) \cdot \cos\phi_h\}}{\int dx_2\, A_0(x_2) \cdot \{1 + \alpha(x_2) \cdot \cos\phi_h\}} \\ &\simeq \frac{\int dx_2\, N_0(x_2) \cdot A_0(x_2) + \cos\phi_h \cdot \int dx_2\, N_0(x_2) \cdot A_0(x_2) \cdot \cos\phi_h \cdot \{\alpha(x_2) + \epsilon(x_2)\}}{\int dx_2\, A_0(x_2) + \int dx_2\, A_0(x_2) \cdot \alpha(x_2)} \\ &\simeq \frac{C_0}{a_0} \cdot \Big[1 + \cos\phi_h \cdot \big(\frac{C_1 + C_2}{C_0} - \frac{a_1}{a_0}\big)\Big] \end{aligned} \tag{5.9}$$

having defined:

$$\begin{aligned} C_0 &= \int dx_2\, N_0(x_2) \cdot A_0(x_2); \\ C_1 &= \int dx_2\, N_0(x_2) \cdot A_0(x_2) \cdot \epsilon(x_2); \\ C_2 &= \int dx_2\, N_0(x_2) \cdot A_0(x_2) \cdot \alpha(x_2); \\ a_0 &= \int dx_2\, A_0(x_2); \\ a_1 &= \int dx_2\, \alpha(x_2) \cdot A_0(x_2). \end{aligned} \tag{5.10}$$

Thus when N_0, ϵ, A_0 and α are functions of x_1 and x_2, the extracted physics amplitude is:

$$\epsilon^m = \frac{C_1}{C_0} + \left(\frac{C_2}{C_0} - \frac{a_1}{a_0}\right), \tag{5.11}$$

and in general the extracted amplitude ϵ^m has a bias, which turns to zero if the cross-section does not depend on x_2 and in general the integration can be performed over all the variables which do not enter the cross-section. If this is not the case, two different situations have been analysed.

1. If the acceptance amplitude α does not depend on x_2, the extracted amplitude is:

$$\epsilon^m = \frac{\int dx_2\, A_0(x_2) \cdot N_0(x_2) \cdot \epsilon(x_2)}{\int dx_2\, A_0(x_2) \cdot N_0(x_2)}. \tag{5.12}$$

   In this case the extracted amplitude ϵ^m embodies the cross section times the acceptance of the apparatus, i.e. its mean value is evaluated with the measured events. This is the typical measured quantity in the case of the target spin dependent SIDIS azimuthal asymmetries, like the Collins and the Sivers asymmetries or the longitudinal spin asymmetries described in chapter 7.

2. If the acceptance in the x_1 bins does not depend on the other kinematical variables (x_2 in our example) the measured amplitude is:

$$\epsilon^m = \frac{\int dx_2\, N_0(x_2) \cdot \epsilon(x_2)}{\int dx_2\, N_0(x_2)}. \tag{5.13}$$

   In this case there is no bias and the extraction of the asymmetry leads to the same result as from analytical calculation starting from the SIDIS cross-section expression.

From these simple calculations we can conclude that the integration (as in eq. 5.8) can be performed over all the variables on which the acceptance or the cross section do not depend. If the azimuthal acceptance is flat in the considered kinematical

range, the results obtained with the method described in 5.1 would be the same as a multi dimensional analysis.

An effective way, to evaluate the dependence of the azimuthal acceptance on the different kinematical variables, is to compare the amplitudes of the azimuthal modulations measured using different MC samples to calculate the acceptance. The acceptance is given by the ratio between the distributions of the reconstructed hadrons N_{rec}^{mc} and of the generated ones N_{gen}^{mc}

$$Acc(\phi_h, x_2) = \frac{\int N_{gen}^{mc}(\phi_h, x_2) \cdot A(\phi_h, x_2) dx_2}{\int N_{gen}^{mc}(\phi_h, x_2) dx_2}, \tag{5.14}$$

for every bin of x_1, in which the asymmetries are extracted. Thus if generated distributions N_{gen}^{mc} of the MC samples have different x_2 dependencies, the result will be different if there is a relevant dependence of the acceptance on x_2. This important test has been done calculating the acceptance using three different tunings of LEPTO, as described in sec. 5.3.1.

5.3 Monte Carlo studies for the azimuthal acceptance calculation

The Monte Carlo software described in chap. 4 has been used to produce the N_{gen}^{mc} and N_{rec}^{mc} distributions. The quantity $Acc = N_{rec}^{mc}/N_{gen}^{mc}$ thus takes into account not only the geometrical acceptance of the apparatus, but also the reconstruction and triggers and detectors efficiencies, as all these effects are fully simulated in the COMPASS Monte Carlo chain.

5.3.1 Tuning of the generator

The agreement between the real data and the MC data is not the same for all the physics channels investigated in COMPASS. In some cases extra tuning had to be done, sometimes leading to no improvement. For the measurements described here a different approach has been used. Since it is not obvious that the discrepancies are due to the event generator only, and not to a non perfect description of the COMPASS spectrometer, three different MC have been used. Starting from the distributions obtained using the default LEPTO setting and compared to the real data distributions in chap. 4, further work has been done on the tuning of the LEPTO parameters related to the fragmentation process and to the Lund FF. A new set of values was found to better describe the COMPASS data. They are compared with those of the default LEPTO tuning, in tab. 5.3.1. The Lund fragmentation function is $FF(z) = (1/z) \cdot (1-z)^{PARJ(41)} exp\Big(- PARJ(42) \cdot m_\perp^2/z \Big)$ where the transverse mass $m_\perp^2 = E_h^2 - p_z^{h2}$ is built from the hadron energy and its longitudinal momentum.

Also, different sets off PDF, like CTEQ5 [62] and MSTW08 [63], have been used and the three MC produced are

mc0 , generated using the default setting and PDFs(CTEQ2),

		default value	new value
PARJ(21)	transverse momentum	$0.36 GeV/c$	$0.34 GeV/c$
PARJ(23)	of hadron in	0.01	0.04
PARJ(24)	the fragmentation	2.0	2.8
PARJ(41)	LUND Frag.	0.3	0.025
PARJ(42)	Function	$0.58 GeV^{-2}$	$0.075 GeV^{-2}$

Table 5.1: Values used in the mc1 and mc2 Monte Carlo generation ("new values") compared with the default setting used in mc0 ("default value").

mc1 , generated with CTEQ5 PDFs, which are used in PYTHIA by default,

mc2 , generated with MSTW08 PDFs and including the correction for the gluon interaction.

Both mc1 and mc2 have the new setting shown in tab. 5.3.1.

The ratios between the distributions for real and MC events are shown in fig. 5.3, for the DIS variables, and in fig. 5.4 for hadrons. The agreement between real and MC data is quite satisfactory for mc1, which is thus considered as the reference. The other two MCs give ratios which show opposite trends for most of the variables, and are considered as "extreme" cases. All the three MC samples have been used to study the kinematical dependence of the azimuthal acceptance as described the next section. The difference between the amplitudes of the azimuthal modulations extracted using the three MCs has also been used to estimate the systematic uncertainty, as will be explained later.

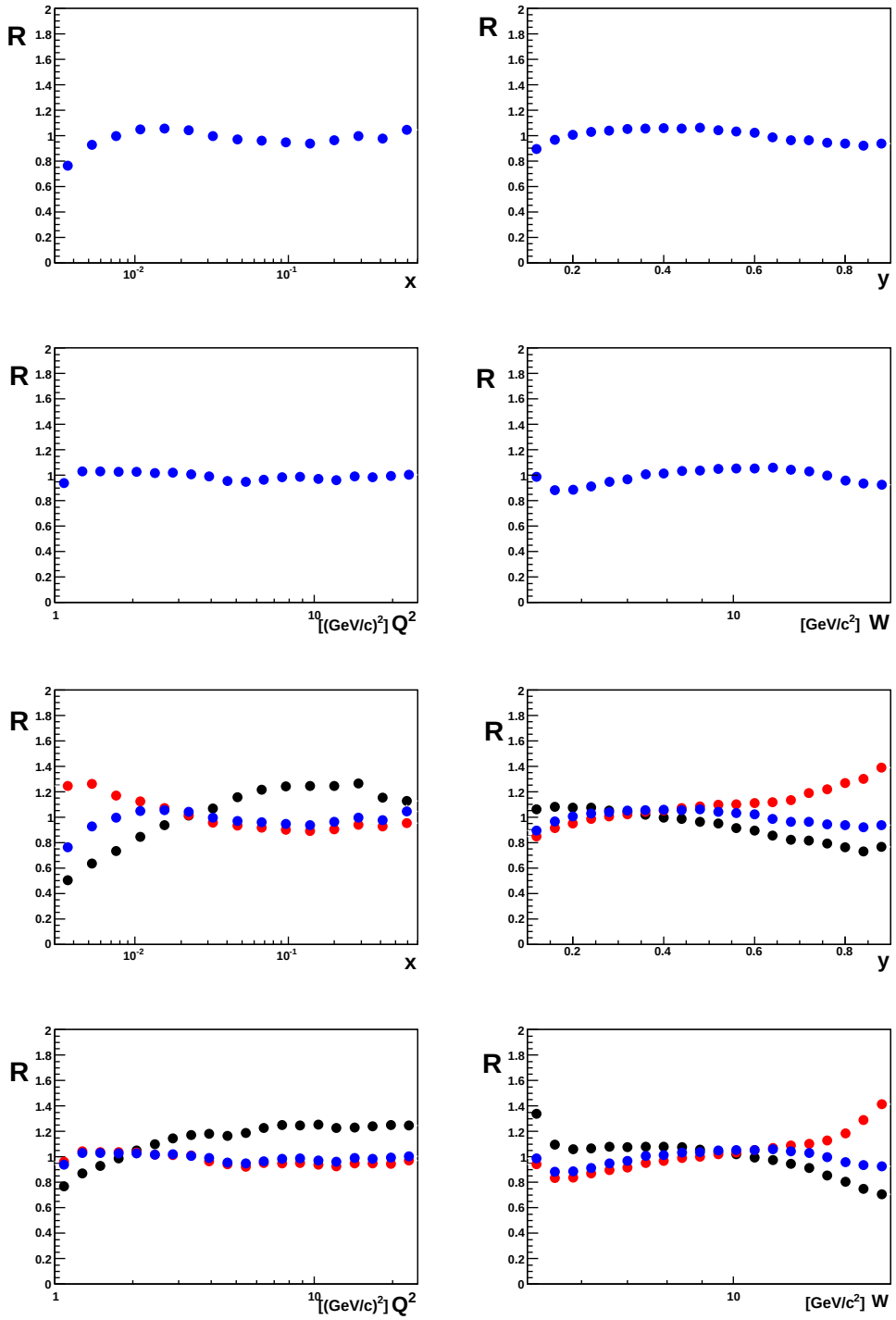

Figure 5.3: Ratios R between kinematic distributions for real and simulated data using the mc1 (upper plot) for the kinematical variables x(top right plot), y(top left plot), Q^2(bottom right plot) and W(bottom left plot). The comparison between the ratios R obtained from the three different MC samples: mc0 (black points), mc1 (blue points) and mc2(red points), is also shown (lower plot). The picture looks the same when considering positive and negative hadrons separately.

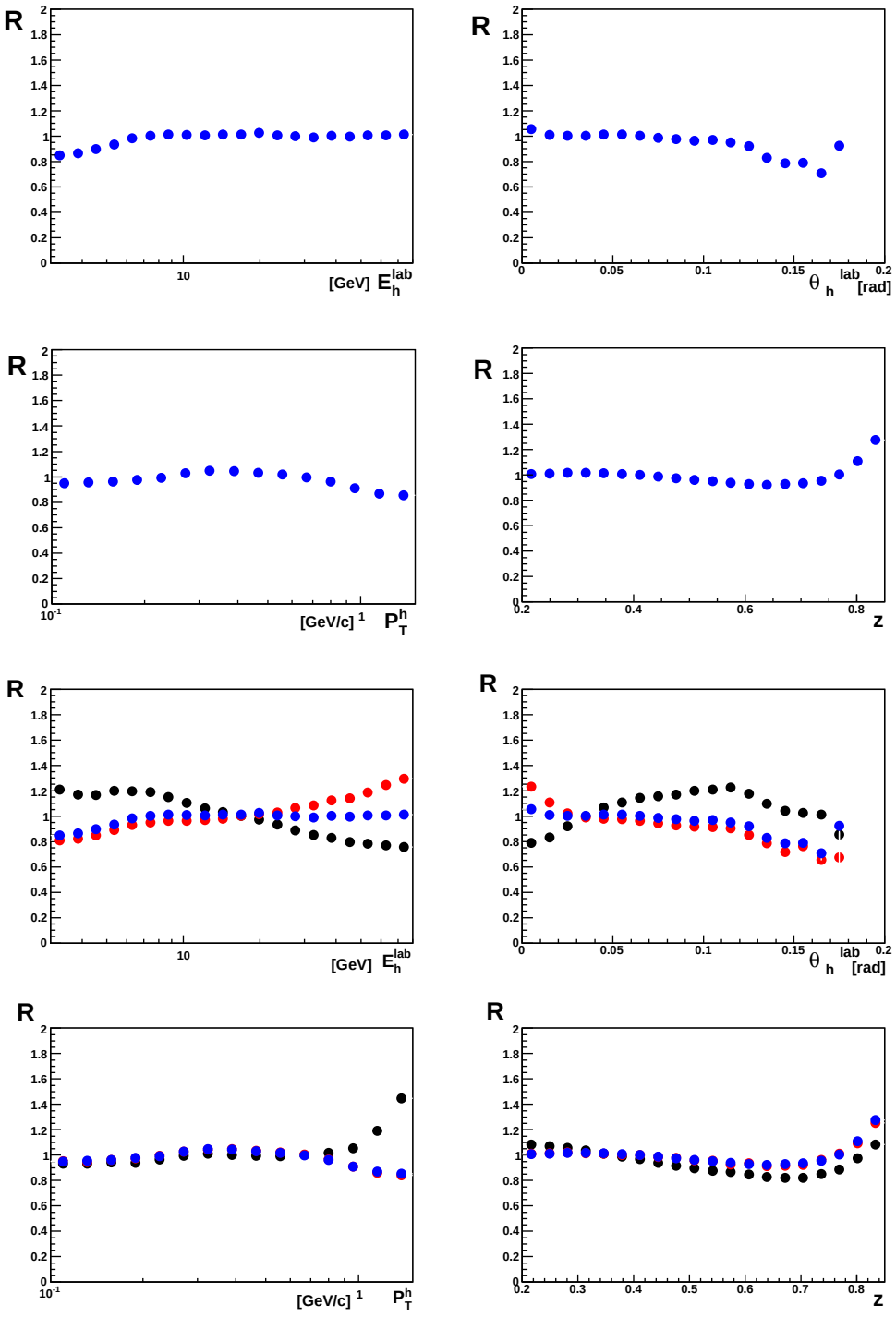

Figure 5.4: As fig. 5.3 for the distributions of the hadron energy (top left plot), the hadron polar angle in the lab (top right plot), z (bottom left plot) and P_T^h (bottom right plot).

5.3.2 Kinematical dependence of the azimuthal acceptance

The three MC samples mc0. mc1 and mc2, have been used to evaluate the physical asymmetries using the integrated acceptance. The results are shown in fig. 5.5 for positive hadrons (the results for the negative hadrons give the same general picture and are not shown). The black points are the amplitudes extracted using mc0, the red points are the ones extracted using mc2 and the blue ones using mc1.

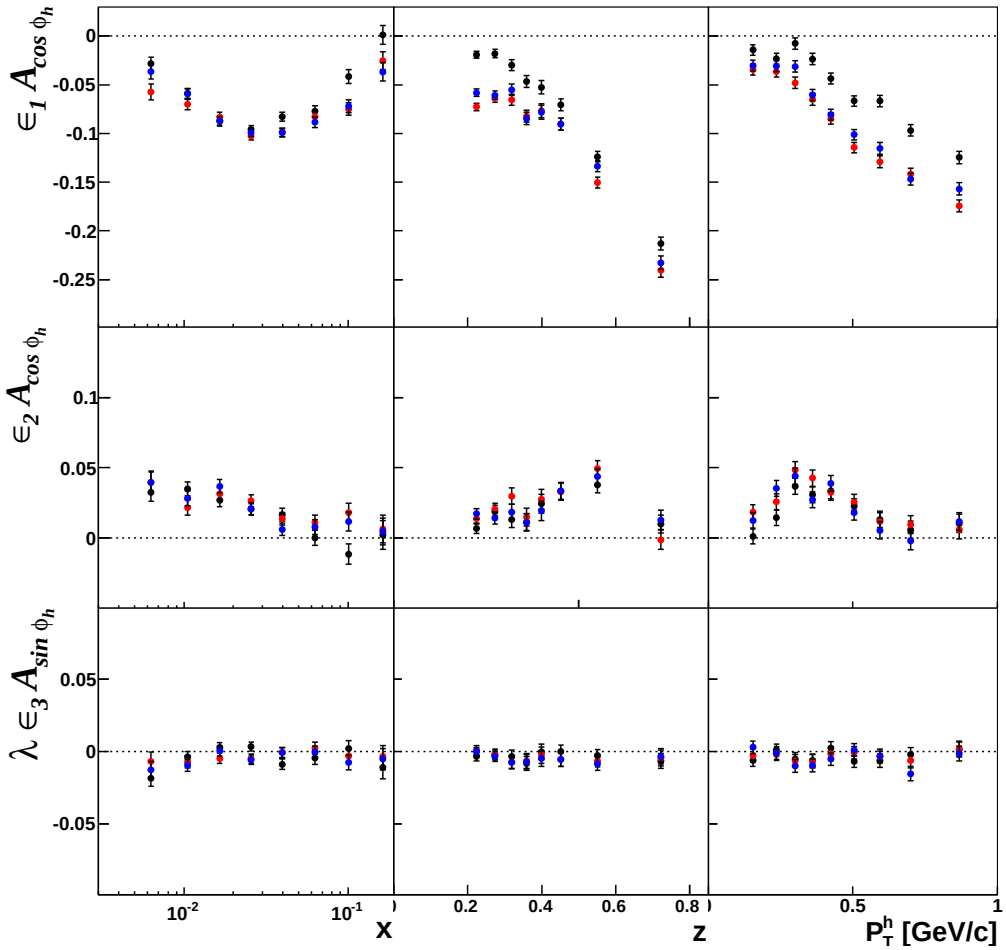

Figure 5.5: Comparison between $\epsilon_1 A_{\cos\phi_h}$ (first column), $\epsilon_2 A_{\cos 2\phi_h}$ (second column) and $\lambda_l \epsilon_3 A_{\sin\phi_h}$ (third column) for positive hadrons as functions of x (first row), z (second row), and P_T^h (third row) as extracted using mc0 (black points), mc2 (red points) and mc1 (blue points) and the "integrated " acceptance as in the first analysis.

As can be seen, the trends are the same, and the values differ by a few standard deviations only for the $\epsilon_1 A_{\cos\phi_h}$ asymmetry as a function of z and P_T^h. This is a clear

effect and detailed studies of the acceptance have shown that with the COMPASS apparatus there is a strong dependence on x of the amplitude of the acceptance $\cos\phi_h$ modulation shows up in the asymmetries measured as functions of z and P_T^h, where the integration over x occurs. If this interpretation is correct the effect can be cured by correcting the measured azimuthal distribution by the acceptance as function of x as in eq. 5.15

$$N^{corr}(\phi_h) = \int dx N^m(\phi_h, x)/Acc(\phi_h, x)\,, \tag{5.15}$$

for each considered bin in z and P_T^h. In this case the measured azimuthal distribution of the hadrons N^m is divided by the acceptance Acc before performing the integration on x, and this is done for each bin in z and P_T^h. This procedure takes into account possible dependencies of the acceptance on the variable x and thus, as explained in section 5.2, the measured asymmetry should be free from biases even if the generated x distribution of the three MC samples used are different. The measured azimuthal distribution are thus obtained by calculating the number of events in each bin of z and P_T^h and in each bin of ϕ_h as

$$N^{corr}(\phi_h) = \sum_i 1/Acc(\phi_h, x_2^i)\,, \tag{5.16}$$

which is the same of eq.(5.15), but for the discrete case. The results obtained by correcting the measured azimuthal distribution as in eq. 5.16 ("2d acceptance") are shown in fig. 5.6 for positive hadrons. They are essentially the same for the three MC samples as expected since the x effective dependence of the acceptance has been fully taken into account.

In spite of the very positive outcome of this test, the azimuthal acceptance has been studied in details, both to search for other possible kinematical dependencies and to calculate the magnitude of the acceptance corrections. For each kinematical bin in x_1, which can be x, z or P_T^h, the acceptance has been parametrized as:

$$\begin{aligned} Acc(\phi_h, x_2) \;=\; & a_0(x_2)\cdot(1 + a_1(x_2)\cdot\cos\phi_h + \\ & + a_2(x_2)\cdot\cos 2\phi_h + a_3(x_2)\cdot\sin\phi_h + a_4(x_2)\cdot\cos 3\phi_h) \end{aligned} \tag{5.17}$$

where each function $a_i(x_2)$ is determined from a fit to the ratio $N_{rec}^{mc}(x_2\phi_h)/N_{gen}^{mc}(x_2\phi_h)$ performed in each bin of x_1. The $\cos 3\phi_h$ modulation has been added to the ones which appear in the cross section to have a better fit χ^2 to the function describing the azimuthal acceptance. The variable x_2 is chosen among y, Q^2, x, z, P_T^h and the polar angle of the virtual photon θ_{γ^*}.

It is worthwhile to explain the relevant role played by θ_{γ^*} in the description of the azimuthal acceptance with some simple geometrical arguments. Let assume the COMPASS apparatus (spectrometer and polarized target solenoid) to cover a circle orthogonal the beam axis and centered on the beam spot, as in fig. 5.7. The scattered muon and the virtual photon meet the circle at opposite side with respect to its center and the SIDIS hadrons are mostly produced in a cone around the virtual photon. The azimuthal angle of the hadron in the GNS ϕ_h is calculated with respect to the scattering plane and the zero is always at the scattered muon side, in the inner

part of the circle while π is always in the outer part. If the opening angle of the virtual photon is large and the cone of hadrons is at the outer edge of the apparatus then the particles produced at $\phi_h \simeq \pi$ are systematically not detected because they are out of the geometrical acceptance. The azimuthal distribution of the hadrons has thus less events at π, giving rise to an effect like a $\cos\phi_h$ azimuthal modulation in the acceptance.

Considering the strong correlation between x and θ_{γ^*}, shown in fig. 5.8, large θ_{γ^*} acceptance corrections would correspond to large corrections and strong x dependence of the azimuthal part of the acceptance. In figure 5.9 the results for $a_1(\theta_{\gamma^*})$ are shown for positive hadrons and for each bin of P_T^h (similar results are obtained for the negative hadrons). Each plot refers to different P_T^h bins ranging from 0.1 to 1.5 GeV/c. The dependence on θ_{γ^*} is strong in every bin of P_T^h for $\theta_{\gamma^*} \gtrsim 0.06$ rad (bin 15) and a_1 can be large, up to 80% at high θ_{γ^*}, leading to large corrections in the corresponding azimuthal asymmetry extraction.

The detailed studies performed on the acceptances have allowed to define a few new cuts to be applied in order to avoid region in which acceptance corrections are large or change a lot. The new, final, cuts which are added to those given in section 5.1, are

- $\theta_{\gamma^*} < 0.06 rad$,
- $y > 0.2$,
- $P_T^h < 1 GeV/c$.

Also only events with $0.003 < x < 0.13$ have been used in the following to reject low statistic bins (after applying the cuts above).

The motivation for the cut $y > 0.2$ can be deduced from fig. 5.10 which shows the amplitudes $a_1(y)$ of the $\cos\phi_h$ modulation as a function of y. The different plots correspond to different P_T^h bins ranging from 0.1 to 1.0 GeV/c There is a clear acceptance effect for the high P_T^h hadrons produced in events with $y < 0.2$. Since y is also related with the direction of the virtual photon a similar reasoning as in the case of θ_{γ^*} justifies the cut. After the cut $y > 0.2$ the requirement $\theta_{\gamma^*} < 0.06$ rad is much less effective, as can be seen in fig. 5.11 where the θ_{γ^*} distribution is shown before (black line) and after (red line) the $y > 0.2$ cut.

The amplitudes a_2 and a_3 have been found to be less dependent on the kinematical variables (no particular effect has been found) and their values are small.

A general overview of the acceptance calculated in the final kinematical region is given in fig. 5.12 where each a_i term appearing in eq. 5.17 is shown as function of pairs of the the kinematical variables x, z and P_T^h. The azimuthal corrections are usually below 20% and almost no dependence from the kinematics is seen.

According to the considerations of section 5.2, being the acceptance corrections almost independent on the kinematical variables, either the simplified method of section 5.1 or the more refined "2d acceptance" corrections could be used to extract the azimuthal asymmetries. To be on the safe side, however, the new method has been used to get the final results, as explained in the next section.

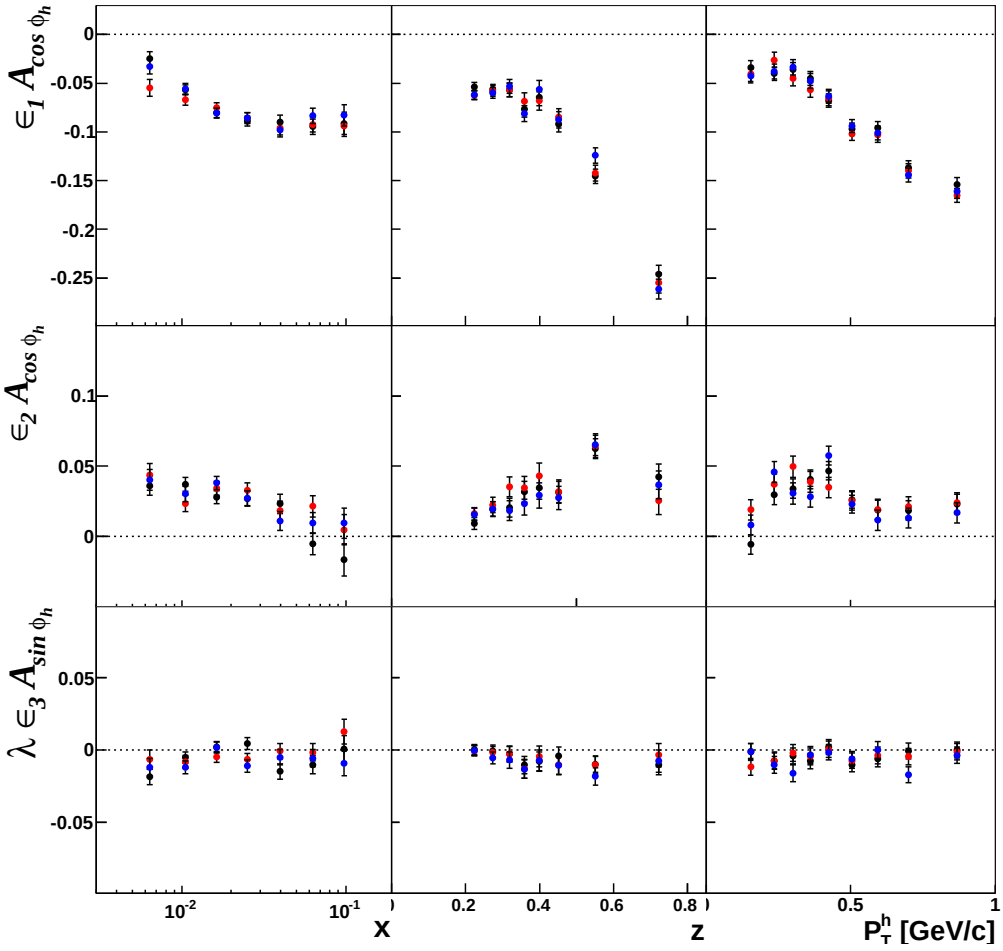

Figure 5.6: Comparison between $\epsilon_1 A_{\cos\phi_h}$ (first row), $\epsilon_2 A_{\cos 2\phi_h}$ (second row) and $\lambda_l \epsilon_3 A_{\sin\phi_h}$ (third row) for positive hadrons as functions of x (first column), z (second column), and P_T^h (third column) as extracted using mc0 (black points), mc2 (red points) and mc1(blue points). The azimuthal distributions extracted in bins of z and P_T^h have been corrected by the acceptance calculated as a function of x.

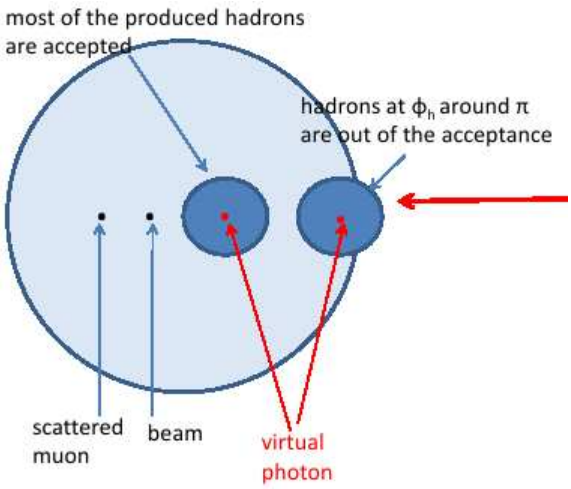

Figure 5.7: Simple geometrical explanation of the large acceptance corrections at large values of θ_{γ^*}: the hadrons produced with $\phi_h \sim \pi$ are systematically rejected if θ_{γ^*} near the outer edge of the apparatus geometrical acceptance.

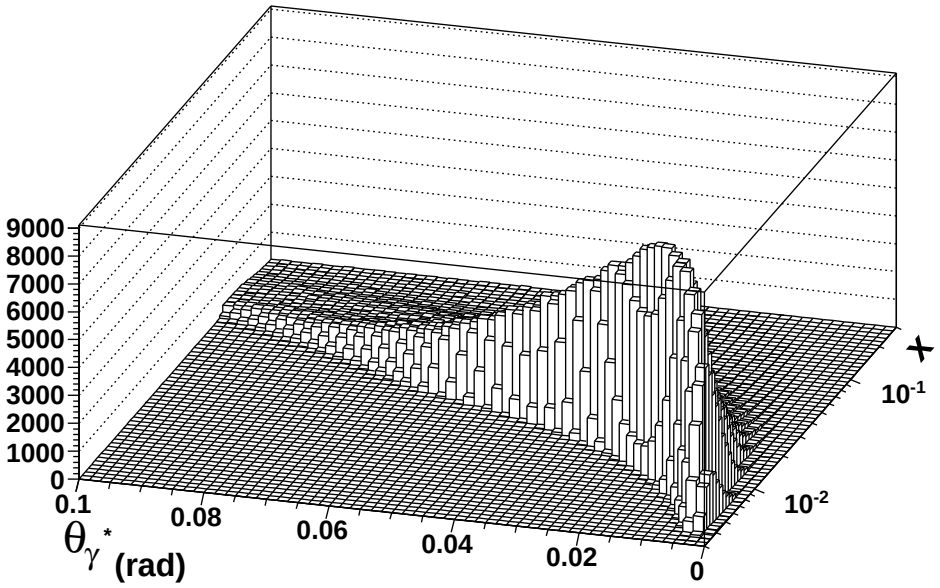

Figure 5.8: Correlation between x and θ_{γ^*}.

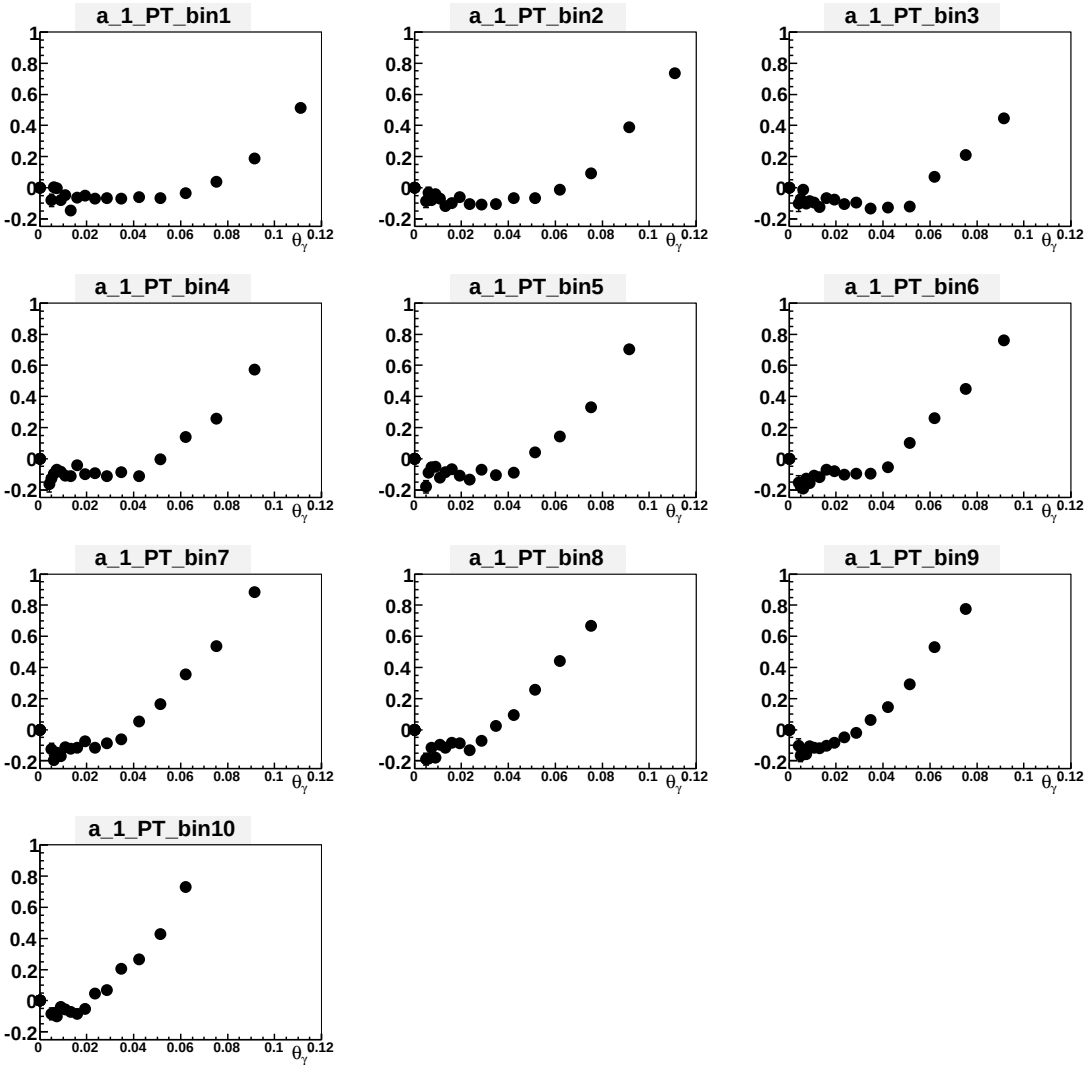

Figure 5.9: Results for $a_1(\theta_{\gamma^*})$ shown for positive hadrons and for each bin of P_T^h. The plots refer to different P_T^h bins ranging from 0.1 to 1.5 GeV/c.

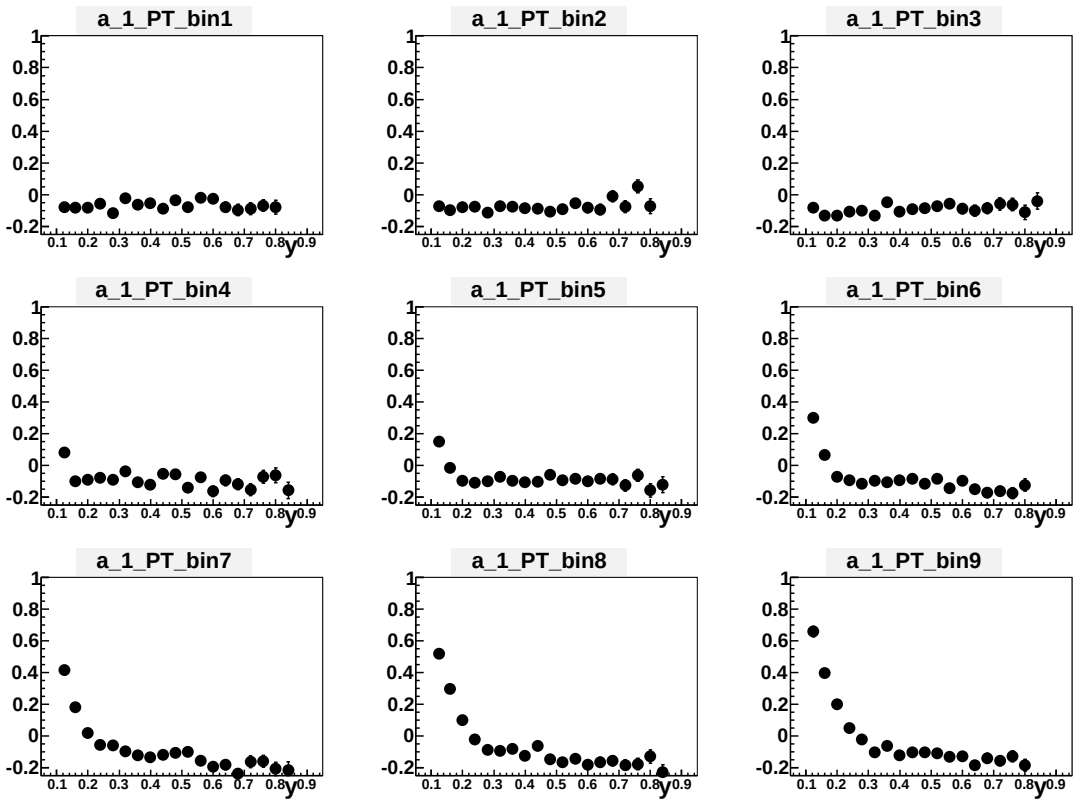

Figure 5.10: amplitudes $a_1(y)$ of the $\cos\phi_h$ modulation as a function of y (only the cuts $P_T^h < 1GeV/c$ and $\theta_{\gamma^*} < 0.06rad$ have been applied in addition to the "old cuts" described in section 5.1). Different plots correspond to different P_T^h bins (ranging from 0.1 to 1.0 GeV/c).

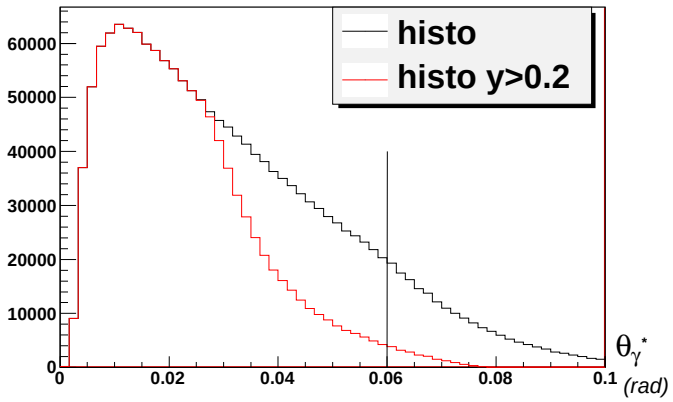

Figure 5.11: The θ_{γ^*} distribution shown before (black line) and after (red line) the $y > 0.2$ cut.

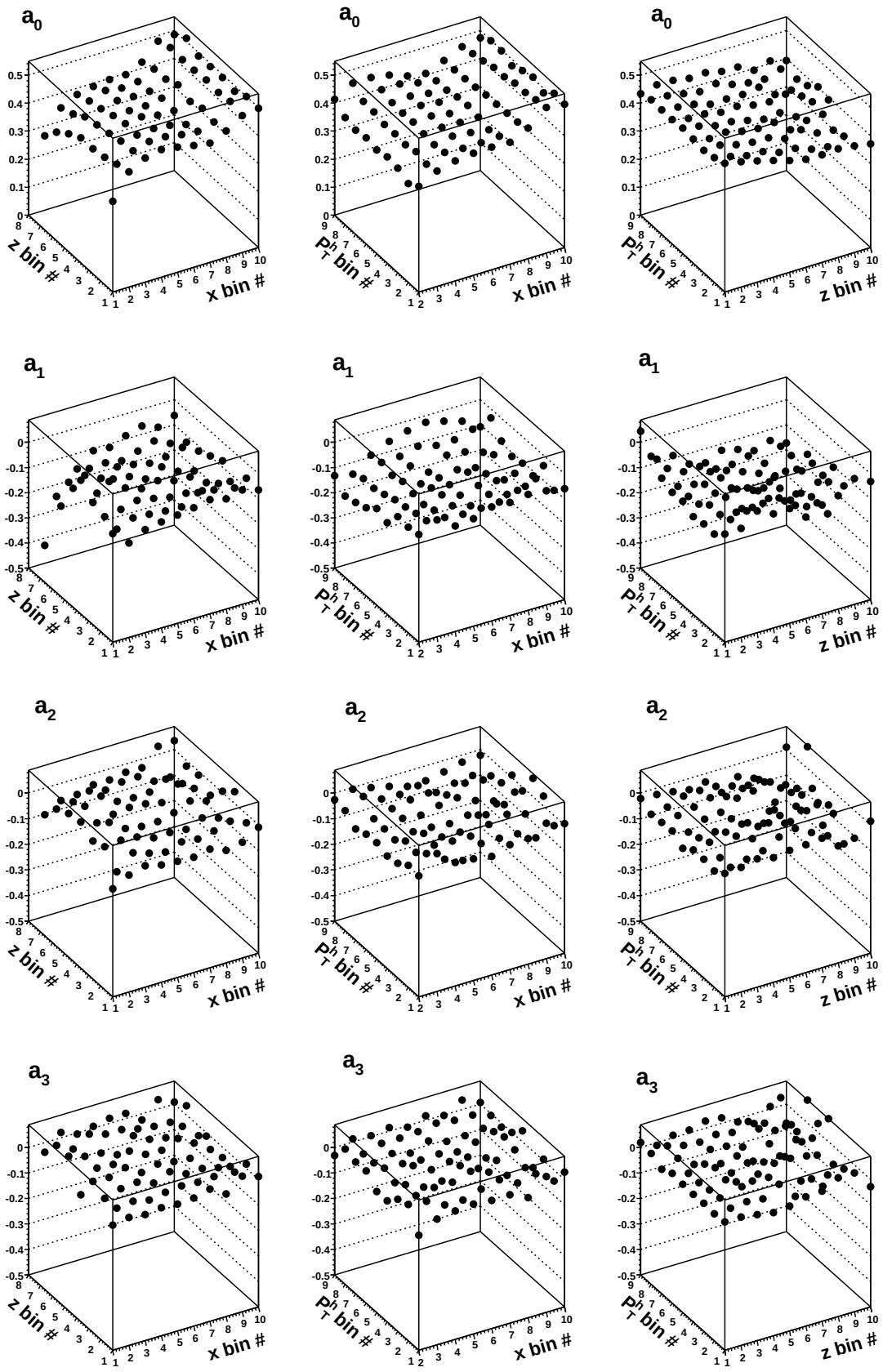

Figure 5.12: a_i parameters of eq. 5.17 extracted from the acceptance calculated in the final kinematical region. On the top row the parameters (a_0, a_1, a_2 and a_3, from top to bottom) extracted in bins of z and x (left column), P_T^h and x (central column) and in bins of P_T^h and z (right column).

5.4 Extraction of the asymmetries

The amplitudes of the azimuthal modulations $\epsilon_i A_i$ have been extracted starting from the distribution corrected for the "2d acceptance". The number of events in each bin of $x_1 = x$, z and P_T^h and in each ϕ_h bin has been calculated as

$$N^{corr}(\phi_h) = \sum_i 1/Acc(\phi_h, x_2^i)\,. \tag{5.18}$$

The sum runs over all the hadrons detected in the given bin of x_1 and $Acc(\phi_h, x_2^i)$ is the value of the acceptance function calculated for the value x_2^i of the hadron i. The function $Acc(\phi_h, x_2)$ is the on given in eq. 5.17 and has been calculated, for every bin of x_1, fitting with suitable functions each amplitude $a_i(x_2)$. Following the results presented in the previous section $x_2 = x$ has been set when extracting the amplitudes in bin of z and P_T^h.

The 2004 transverse data sample (W33, W34, W35, W36) with the cuts described in sec. 5.3.2 and the simulated events from mc1, described in sec. 5.3.1, have been used. The data collected with opposite target polarizations have been equalized to have the same flux with positive and negative polarizations in order to cancel possible contributions coming from the spin dependent asymmetries.

The statistical error σ_{corr} has been calculated for N^{corr} in every bin of ϕ_h as the sum in quadrature of two contributions. One is given by the statistical error associated to N^{corr} in each bin and is given by

$$\sigma_1 = \sqrt{\sum_i w_i^2}, \tag{5.19}$$

where $w_i = 1/Acc(\phi_h, x_2^i)$. The other comes from the statistical error coming from the x_2 integrated acceptance Acc, which is given by the ratio $\frac{N_{rec}^{mc}(\phi_h)}{N_{gen}^{mc}(\phi_h)}$ calculated for each bin of x_1. The binomial formula has been used to evaluate this error

$$\sigma_2 = \frac{\sqrt{N_{gen}^{mc} \cdot Acc \cdot (1 - Acc)}}{N_{gen}^{mc}}. \tag{5.20}$$

where N_{rec}^{mc} and N_{gen}^{mc} are the ϕ_h bin content of the reconstructed and generated azimuthal distribution and $Acc = \frac{N_{rec}^{mc}}{N_{gen}^{mc}}$. Finally

$$\frac{\sigma_{corr}}{N^{corr}} = \sqrt{(\frac{\sigma_1}{N^{corr}})^2 + (\frac{\sigma_2}{Acc})^2}\,. \tag{5.21}$$

The amplitudes of the azimuthal modulations are then obtained by fitting $N^{corr}(\phi_h)$ with the function

$$f(\phi_h) = p_0 \cdot \{1 + p_1 \cdot \cos\phi_h + p_2 \cdot \cos 2\phi_h + p_3 \cdot \sin\phi_h\} \tag{5.22}$$

and p_0 and the amplitudes p_1, p_2, p_3 are extracted for each bin in the variable x_1, namely x, z and P_T^h. The two bins in the $\phi_h \simeq 0$ region have been not used for the fit, as described in section 4.3.2.

The measured amplitudes $\epsilon_1 A_{\cos\phi_h}$, $\epsilon_2 A_{\cos 2\phi_h}$ and $\lambda_l \epsilon_3 A_{\sin\phi_h}$ are shown in fig. 5.13 for positive hadrons and in fig. 5.14 for the negative hadrons. The error bars are the statistical error coming from the fit.

The impact of the new cuts described in sec. 5.3.2 on the results is almost negligible for all the extracted amplitudes and over the explored kinematics. Only the results for $A_{\cos\phi_h}$ in the high x region slightly change, going towards more negative values, in particular for negative hadrons where the amplitudes extracted as functions of z and P_T^h are also systematically lower. The negative hadrons $A_{\cos 2\phi_h}$ amplitudes are shifted to lower values. The same strong dependence on z and P_T^h appears, for both $A_{\cos\phi_h}$ and $A_{\cos 2\phi_h}$, using the new cuts and the one described in sec. 5.1.

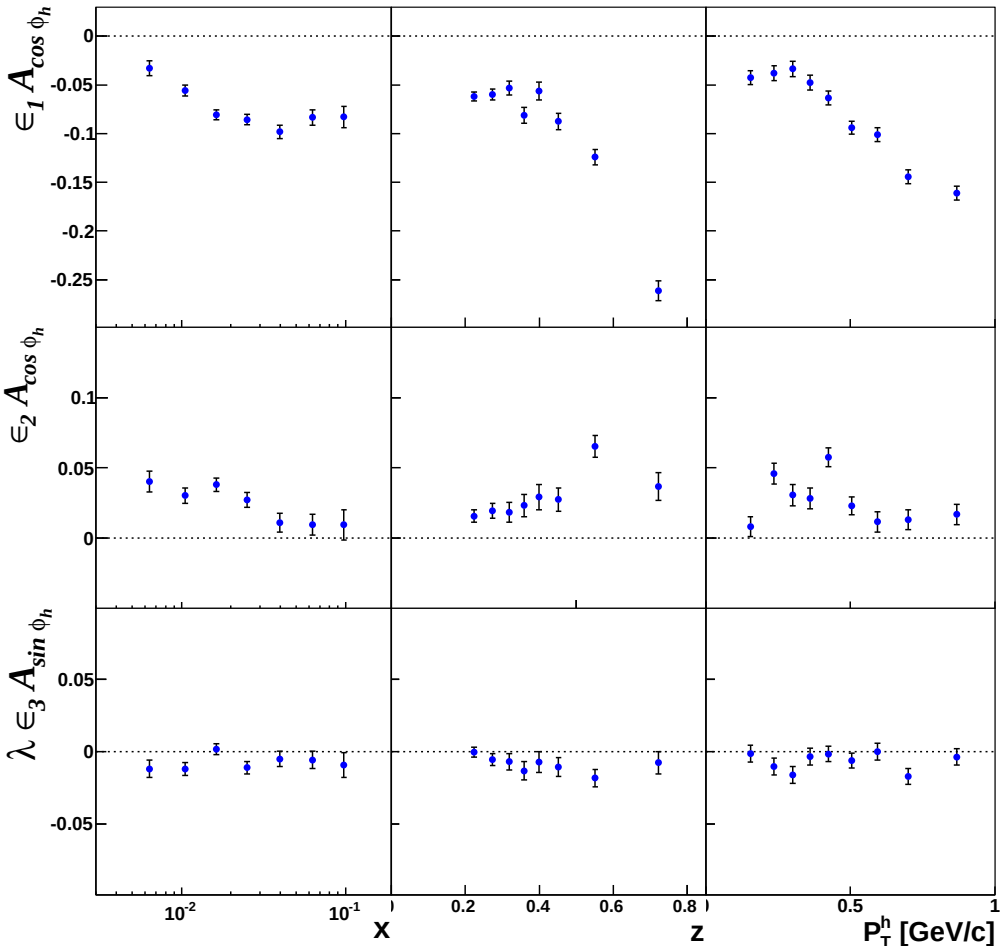

Figure 5.13: Results for the amplitudes of the azimuthal modulations for positive hadrons as a function of x (left column), of z (central column) and of P_T^h (right column). The amplitudes of the $cos\phi$ modulation ($\epsilon_1 A_{\cos\phi_h}$) are on the first row, the amplitudes of the $cos2\phi_h$ ($\epsilon_2 A_{\cos 2\phi_h}$) are on the second row and the amplitudes of the $sin\phi_h$ modulations ($\lambda_l \epsilon_3 A_{\sin\phi_h}$) are on the third row. The azimuthal distributions extracted in bins of z and P_T^h have been corrected by the acceptance calculated as a function of x.

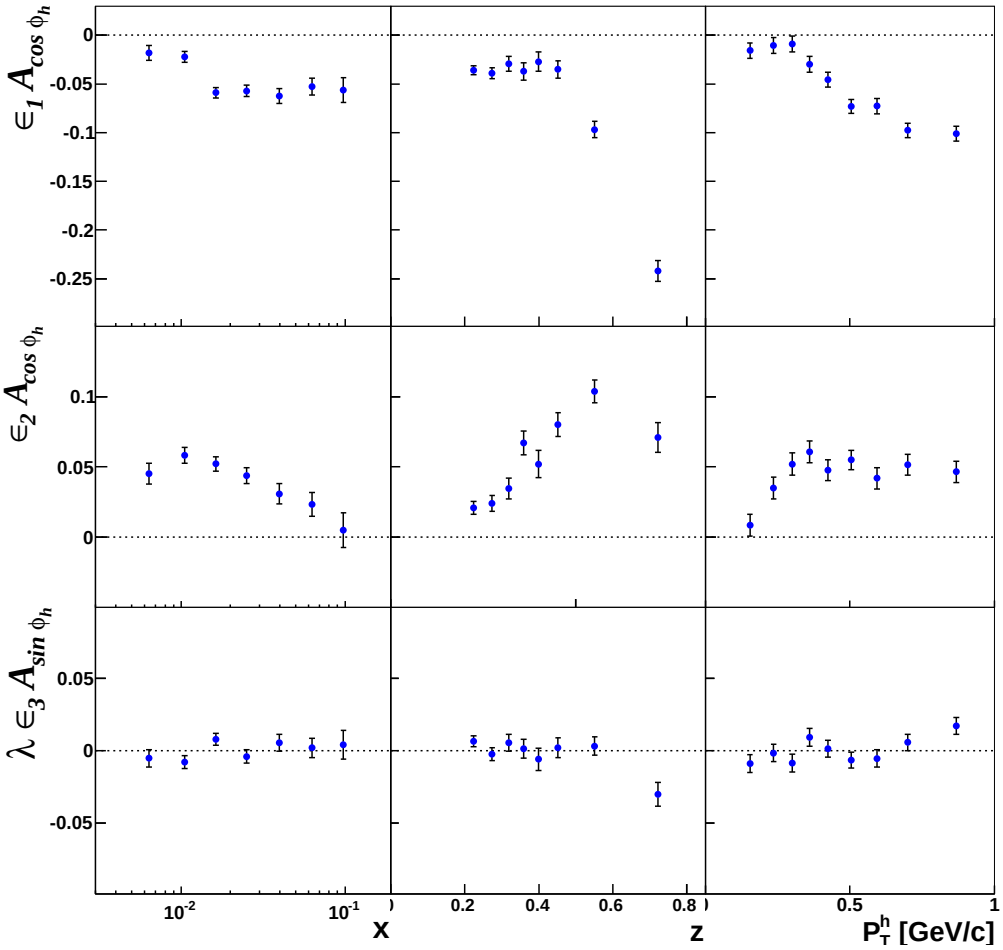

Figure 5.14: same as fig.5.13 but for negative hadrons.

5.5 Systematic studies

Several possible systematic effects have been investigated. The most relevant are described in this section. Not all of them turned out to have important effects and thus had not to be included in the systematic errors given in section 5.5.8.

5.5.1 Radiative corrections

As seen before, while considering lepton nucleon scattering, only the main contribution to the cross-section given by a single photon exchange (the so-called Born contribution) is taken into account. Other contributions are then introduced as corrections (generally referred as radiative corrections). These corrections depend by the experimental observable considered, by the kinematics and by the cuts used in the data analysis and have to be calculated case by case.

For unpolarized asymmetries, photon emissions from the muons modify the reconstructed virtual photon 4-momentum, which differs from the true virtual photon exchanged in the muon-nucleon interaction. This bias the azimuthal distributions, since the reconstructed virtual photon direction in the scattering plane is always at larger angles than the true virtual photon, given the unaccounted energy of the radiated photon.

The effect on the measured asymmetries is expected to be small at COMPASS where the beam is composed by muons. However it has been evaluated by mean of Monte Carlo simulations. Radiative effects are not included in the LEPTO generator, and have been taken into account by using a dedicated software named RADGEN [60] in combination with LEPTO. For this case the simulation proceeds as follows:

1. as a first step LEPTO generates according to the DIS cross-section the lepton kinematics only;

2. using this kinematics, RADGEN calculate the weights for the Born DIS cross-sections (modified at NLO by the loops and by photon emission and absorption by the muons), and the weights for elastics, quasi elastics and inelastic scattering channels of the γ^*-nucleon cross-section;

3. if a radiative event have happened RADGEN also generates the emitted real photon and the virtual photon exchanged in this configuration;

4. if the final invariant mass of the $\gamma^* - N$ system is above 2 GeV/c^2, LEPTO is called again to complete the event generation with the generation of the hadronization and of the nucleon remnant.

About 10 millions of event have been generated for a deuteron target, both with and without RADGEN included. The event kinematics have been reconstructed using the muon information only (as for the real data) and the same selection applied in the analysis (namely $Q^2 > 1$ (GeV/c)^2, $W > 5$ GeV/c^2, $0.2 < y < 0.9$, $0.003 < x < 0.13$, $\theta_{\gamma^*} < 0.06$ rad and $0.2 < z < 0.85$, $0.1 < P_T^h < 1.0$ GeV/c for the hadrons) have been applied to these Monte Carlo events.

In each bin of x, z or p_T^h used for the analysis, the ratio:

$$R(\phi_h) = \frac{N(\phi_h)_{\text{Lepto+Radgen}}}{N(\phi_h)_{\text{Lepto}}}$$

has been calculated, with, as usual, the azimuthal angle of the hadron produced ϕ_h evaluated in the gamma-nucleon system. Fitting this ratio with the function:

$$f(\phi_h) = p_0 \left[1 + p_1 \cos\phi_h + p_2 \cos 2\phi_h\right]$$

allows to extract the amplitude of the azimuthal modulations introduced by the modification of the kinematics. The full set corrections for positive and negative hadrons are shown in figure 5.15 for the $\cos\phi_h$ modulation and in figure 5.16 for the $\cos 2\phi_h$ modulation.

The correction is negligible for the $\cos 2\phi_h$ modulation and is small (few per cent in the high x region at most) for the $\cos\phi_h$ modulation, almost of the same size both for positive and for negative hadrons. This is expected, given the use of muon beams and by the presence of hadrons in the final state which limits the radiative corrections to the inelastic part of the $\gamma - N$ cross-section.

Moreover, the use of a more complete analytical calculation [64] gave a first indication of negligible effects ($\lesssim 1\%$ for the $\cos\phi_h$ modulation) in the COMPASS environment. For this reason the radiative corrections have finally not been applied to the measured asymmetries and not included in the systematic errors.

Radiative effects can also explain the fact, already mentioned in section 4.3.2 of chapter 4, that the distribution of the azimuthal angle of the hadron calculated in the GNS from the real data shows a peak around $\phi_h = 0$ rad which is not reproduced by any MC sample. To be on the safe side it was finally decided to exclude the two central bins of the azimuthal distributions of the hadrons. This effect has been attributed to the electrons or positrons coming from the high energy photons radiated in the DIS interaction. As can be seen in fig 5.17, the radiated photon azimuthal distribution is concentrated at $\phi_h = 0$ rad. Thus it is reasonable to assume that also most of the electrons or positron produced in the conversion inside the apparatus go in that region.

Further studies have been done to verify these considerations. The generated Lepto+Radgen MC sample passed through the full MC chain described in chapter 4, i.e. performing both the propagation through the apparatus and the reconstruction.

The azimuthal distributions obtained from the hadrons produced separately in the events after the standard SIDIS cuts, described in chapter 4, in which the photon radiation occurred ("irad!=0") or not ("irad==0"), are shown in figures 5.18, for the generated (upper plots) and reconstructed (lower plots) samples. The generated distribution produced with "irad!=0" does not have the peak since the real photon are cut out by the requirement of a charged particle. The products of the photon conversion (mainly in the target region and wrongly associated to the interaction vertex) are clearly visible in the distribution obtained in the reconstructed sample. It has been also checked that those particles are mainly $e^+\,e^-$. In figure 5.19 the ϕ_h distribution of the hadron obtained from the reconstructed sample is shown for all the hadrons (after the SIDIS cuts).

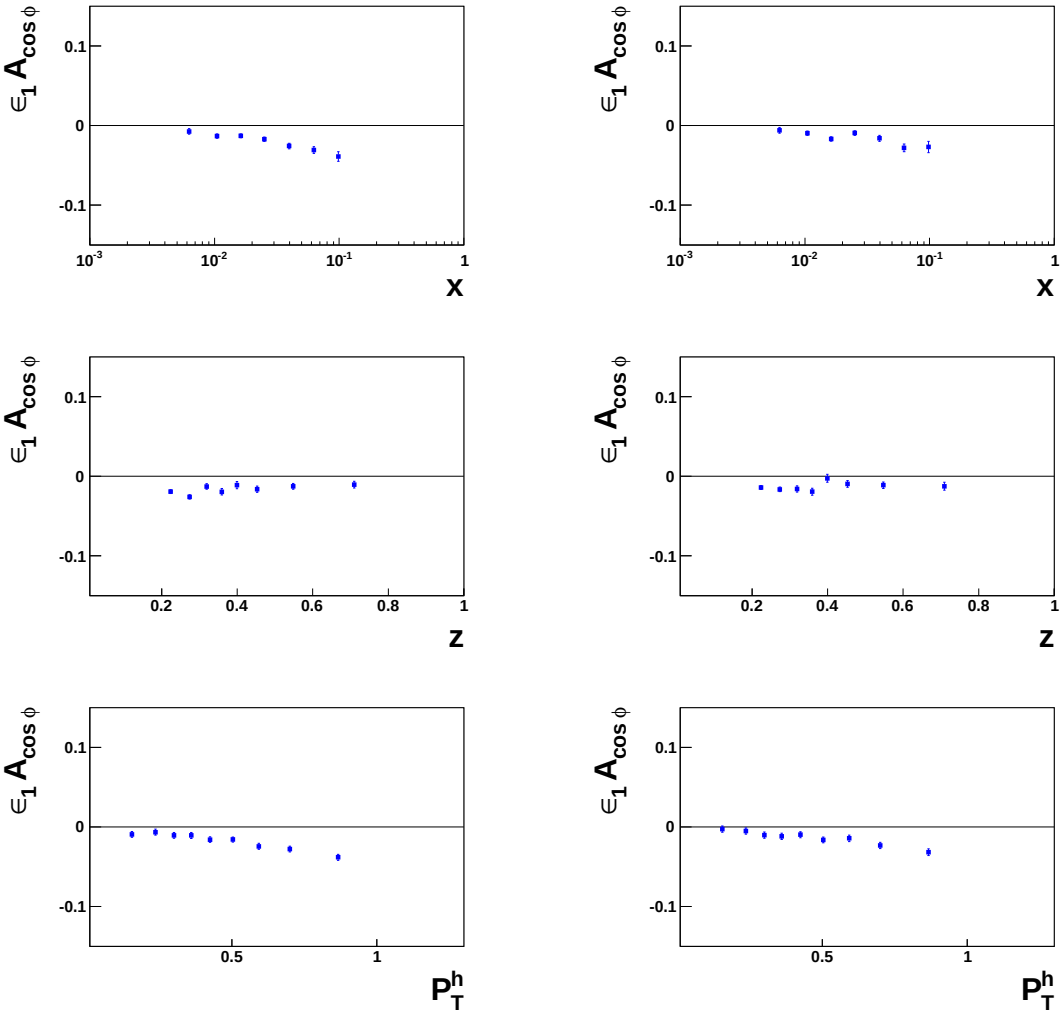

Figure 5.15: Amplitudes in the $\cos\phi$ azimuthal modulations induced by radiative events for positive (left) and negative (right) hadrons

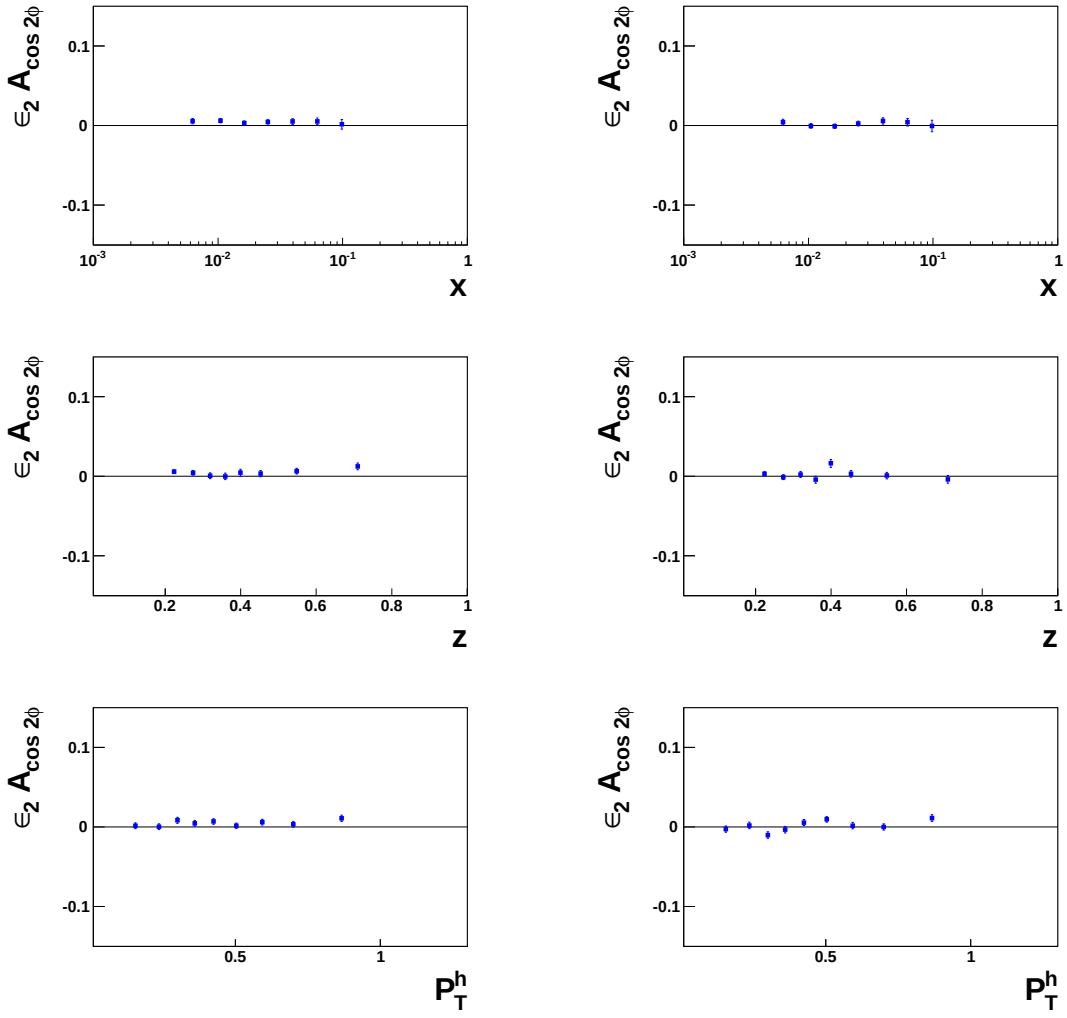

Figure 5.16: Amplitudes in the $\cos 2\phi$ azimuthal modulations induced by radiative events for positive (left) and negative (right) hadrons

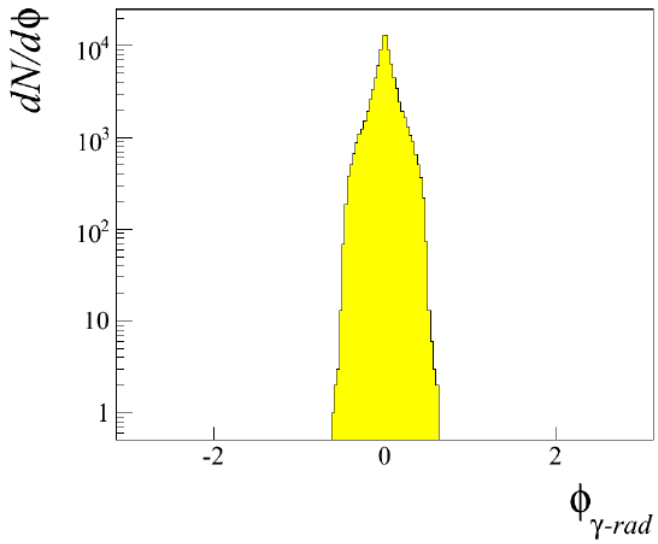

Figure 5.17: Azimuthal distribution of the azimuthal angle of the radiative photon produced in the DIS interaction. The azimuthal angle of the photon is calculated in the GNS.

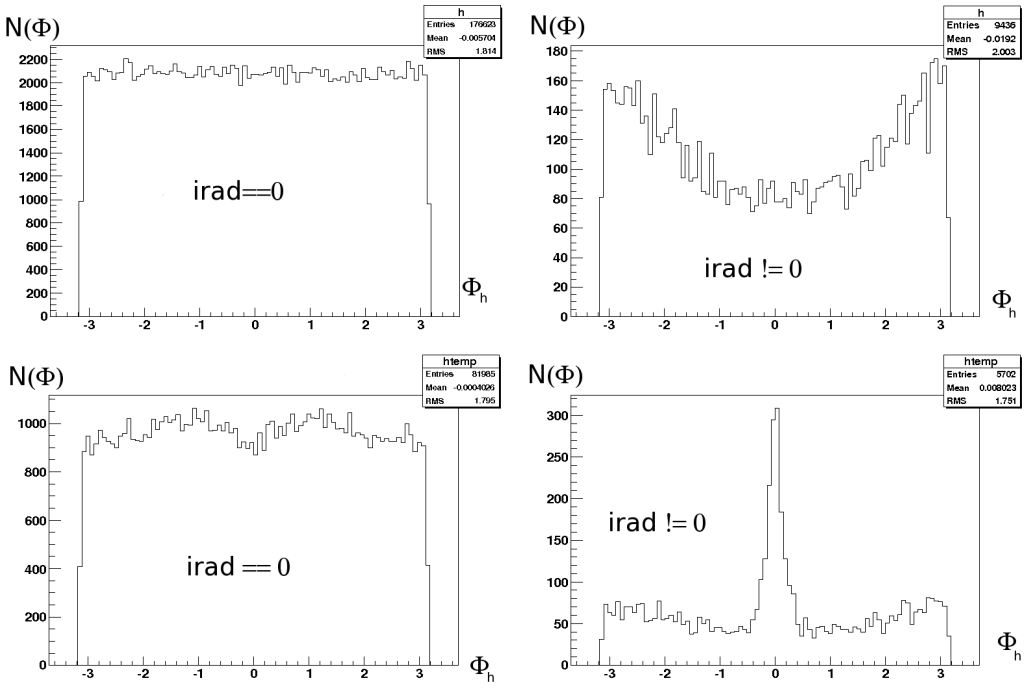

Figure 5.18: The azimuthal distributions of the hadrons are shown for the generated sample (two top plots) and the reconstructed sample (two bottom plots). The plots on the left side are produced using only the events for which no radiation of a real photon occurred ("irad==0"), the plots obtained using only the radiative events are shown on the right side ("irad!=0").

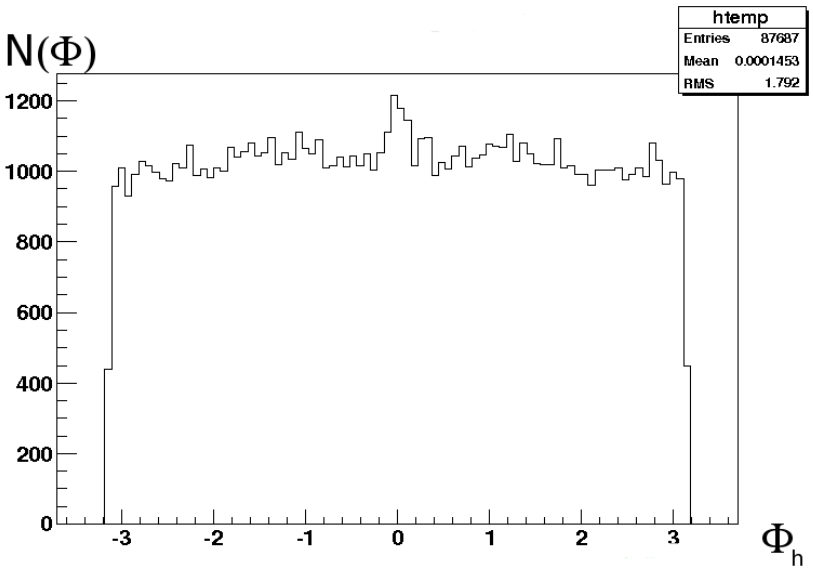

Figure 5.19: MC ϕ_h distribution ("irad!=0" or "irad==0").

The ratio between the ϕ_h distributions of the MC Lepto+Radgen and Lepto samples, after the final selection described in section 5.3.2, has been calculated and it is shown in figure 5.20. The only difference between the two samples is the simulation of the radiative effects and the ratio gives an estimation of the radiative corrections on the amplitudes extracted from the real data. The ratio has been fit with the curve $p_0 \cdot (1 + p_1 \cos\phi_h + p_2 \cos 2\phi_h + p_3 \sin\phi_h)$. As expected the amplitude of the $\cos\phi_h$ modulation is negative and of the order of few percent, while the other two amplitudes are compatible with zero.

An estimation of the number of hadrons in the peak from the measured and the MC Lepto+Radgen azimuthal distributions has been done. The two azimuthal distributions (from real and Monte Carlo data) have been fit using the curve $f = p_0 \cdot (1 + p_1 \cos\phi_h + p_2 \cos 2\phi_h + p_3 \sin\phi_h + p_4 \cos 3\phi_h)$ and the central region have been excluded by the fit as in the analysis. The value of the function f_i in each bin i of the central region has been subtracted to the bin content n_i of the distribution. Then the quantity

$$\frac{\sum_i n_i - f_i}{N}, \tag{5.23}$$

where N is the number of entries of the distribution, has been used to estimate the relative size of the peak. It seems that the peak is almost a factor of ten bigger in the MC distribution than in the measured one, as shown in fig. 5.21, indeed confirming that the radiative corrections calculated from the MC are overestimated.

This is also deduced by comparing the calculation made by A.Afanasef [65] for the muon scattering in the COMPASS kinematics. In fig. 5.22 the ratio $\sigma^{exp}/\sigma^{Born}$, between the DIS cross section calculated including the radiative effects and the Born one, as calculated using the Lepto+Radgen MC sample and the one calculated by [65] are compared. The difference from $\sigma^{exp}/\sigma^{Born} = 1$ is, again, roughly ten

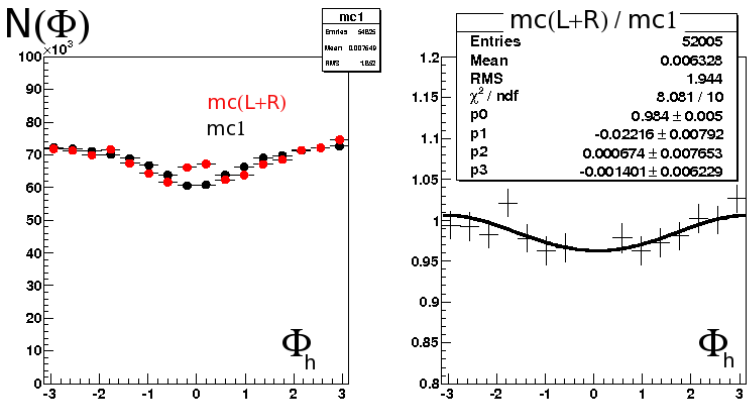

Figure 5.20: ϕ_h distributions obtained from the MC sample used in the analysis (black points on the left plot) and from the MC Lepto+Radgen sample (red points on the left plot). The ratio between the red and black points is shown on the right together with the fit parameters of the function $p_0 \cdot (1 + p_1 \cos\phi_h + p_2 \cos 2\phi_h + p_3 \sin\phi_h)$.

times bigger in the first case.

These studies suggest that the radiative corrections on the asymmetries shown in figures 5.15 and 5.16 are overestimated, thus suggesting a negligible contribution of these effects on the extracted asymmetries.

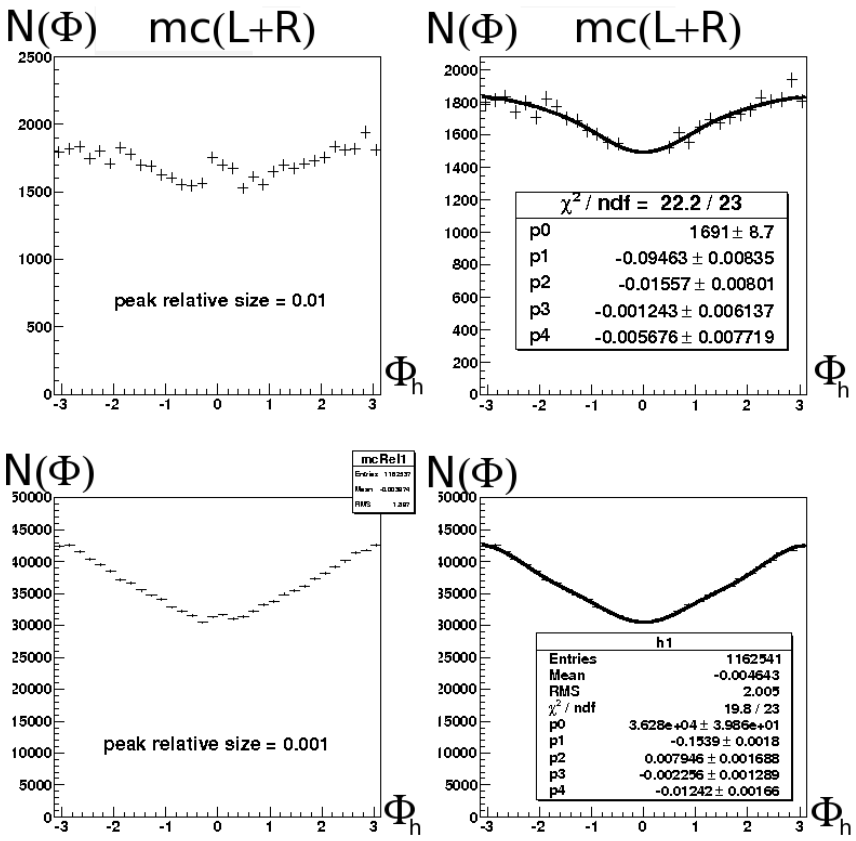

Figure 5.21: ϕ_h distribution obtained after the cuts described in section 5.3.2 from the MC (upper plots) and from the real (lower plots) data sample. The fit function $f = p_0 \cdot (1 + p_1 \cos\phi_h + p_2 \cos 2\phi_h + p_3 \sin\phi_h + p_4 \cos 3\phi_h)$ is also shown, in the right plots.

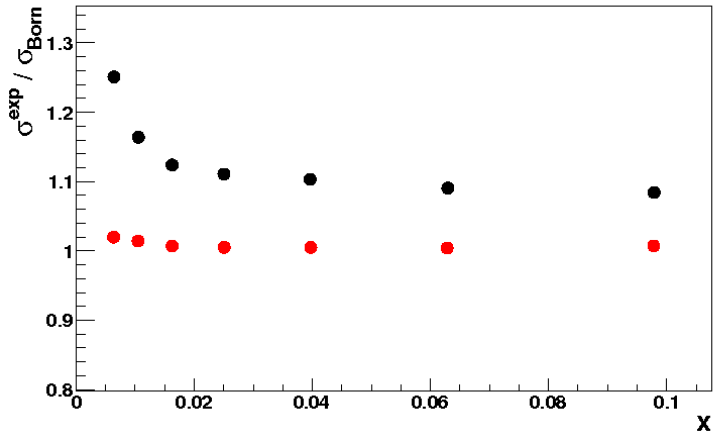

Figure 5.22: Weights ($\sigma^{exp}/\sigma^{Born}$) as function of x defined as the ratio between the DIS cross sections: calculated including the radiative effects and the Born one. The black points are the weights calculated using Lepto+Radgen and the red points are the calculations from [65], made for COMPASS and in the same kinematics.

5.5.2 Studies on the sensitivity of the azimuthal distribution to the measured scattered muon momentum

A bias in the measurement of the scattered muon would shift the reconstructed direction of the virtual photon systematically to larger or smaller values of its polar angle measured from the nominal beam direction. Even a small effect of this kind could lead to a distortion in the azimuthal distribution of the hadron. This effect is illustrated in fig. 5.23 where the COMPASS apparatus is assumed to cover a circle orthogonal the beam axis and centered on the beam spot. The scattered muon and the virtual photon meet the circle at opposite side with respect to its centre and the SIDIS hadrons are mostly produced in a cone around the virtual photon. The direction of the virtual photon is calculated from the beam and the scattered muon momenta and it gives the Z axis of the GNS. The azimuthal angle of the hadron in the GNS ϕ_h is calculated with respect to the scattering plane and the zero is always at the scattered muon side, in the inner part of the circle while π is always in the outer part. The ϕ_h distribution is calculated counting the hadrons which are in each bin, which is a section of the circle around the virtual photon. Assuming that the value of the momentum of the scattered muon is always underestimated the reconstructed virtual photon is always shifted towards the scattered muon, introducing thus a deformation in the measured azimuthal distribution of the hadron.

A crucial role is played by the value of the magnetic field B of SM2, the magnet located in the second stage of the spectrometer. An overestimate or underestimate of the field B translates directly in a systematic effect on the value of the scattered muon momentum p, being $pc = eBR$, where R is the curvature radius.

It has been found that in the processing of the 2004 data used in the first analysis [61] the value of the magnetic field B of SM2 was almost 1% lower than the real one measured by the NMR system. This means that all the measured scattered muon momenta are 1% lower than their real values.

The effect on the kinematical distributions is small and could not be determined comparing kinematical distributions obtained from real data and Monte Carlo data [66]. On the contrary it can introduce a non negligible distortion in the hadron azimuthal distributions. This point has been investigated comparing the distributions obtained from 2 different Monte Carlo samples: one with the same value of B in both propagation and reconstruction and the other using, during the reconstruction, a value which is 1% lower than the one used in the propagation. Large $\cos\phi_h$ modulations have been found in the ratio between the hadron azimuthal distributions, as shown in fig. 5.24 (left plot). Their amplitudes have been also calculated in different intervals of the kinematical variables and, as an example, they are shown in fig. 5.24 (right plot) as function of x where there is a clear dependence of the effect.

The wrong value, for the SM2 field, was not taken into account in the first measurement of the azimuthal asymmetries [61] and it is the responsible for the differences of those results with the new ones [67] presented in this thesis.

In the new analysis the problem has been removed by applying a correction to all the momenta measured using SM2, essentially by rescaling them by a proper factor. The correction procedure has been verified using the 2 simulations previously described and applying the rescaling factor to the one with the bias. The amplitudes

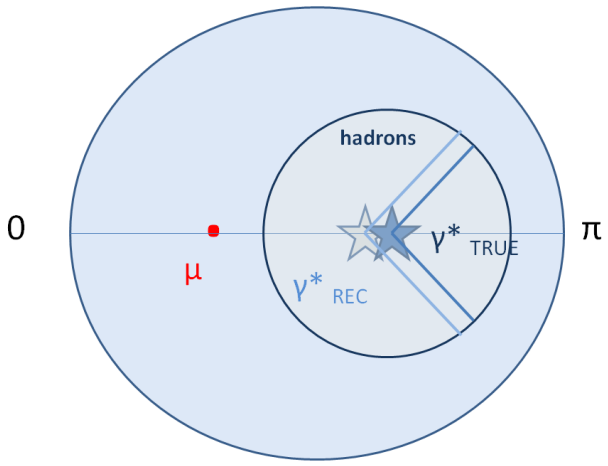

Figure 5.23: Illustration of the effect on the azimuthal distribution of the hadrons of a mis-reconstructed virtual photon. The beam impinges on the picture, perpendicularly to the sheet, and, for simplicity, let assume that the big circle is the acceptance of the COMPASS apparatus projected on the XY plane perpendicular to the beam line. From the momentum conservation the scattered muon (the red point) and the virtual photon (the blue star) go at opposite sides of the incoming muon. The SIDIS hadrons are produced mostly inside a cone, having the virtual photon at the centre and represented by the smaller circle in the picture. The ϕ_h distribution is essentially given by the counts of the hadrons which go into one sector of the small circle (drawn at π in the picture). If the reconstructed virtual photon direction is systematically shifted towards smaller values of the polar angle, with respect to the real one, a greater number of hadrons is counted in the bin at π while a lesser number is counted at zero, with respect to the situation of an exactly reconstructed virtual photon direction. This systematic effect is given, for example, if the momentum of the scattered muon is always underestimated and gives an additional $\cos\phi_h$ modulation in the hadron distribution.

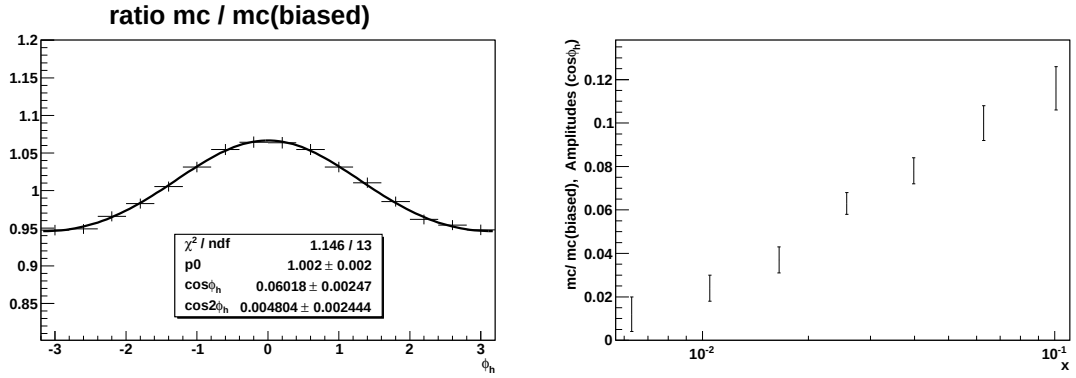

Figure 5.24: Ratio between the hadron azimuthal distributions (left plot) obtained from 2 different Monte Carlo samples: one with the same value of B in both propagation and reconstruction and the other using, during the reconstruction, a value which is 1% lower than the one used in the propagation. Amplitudes of the $\cos\phi_h$ calculated in the different bins of x (right plot) are also shown.

of the $\cos\phi_h$ modulations has been checked to be zero in the ratio of the azimuthal distributions of the hadron resulting from the two different MC samples.

To reproduce the same situation in both real data and Monte Carlo data, the MC sample with the lower value of the SM2 field (with respect to the one used in the propagation) and rescaled as for the real data, has been used to calculate the acceptance of the apparatus.

5.5.3 Detector smearing

The possible wrong reconstruction value of the kinematical variables due to the finite resolution of the detectors and of the tracking, already discussed in chap. 4, could result in a migration of an event (or hadron) to one bin to the next one. This effect, from now on called "smearing", could lead to a dilution of a signal or, if the smearing systematically shifts the quantities towards lower (or higher) values, to a change in the calculated amplitude.

The effects given by the smearing have been evaluated using the MC samples and looking at the quantities $N^{corr}(\phi_h) = \frac{N^{mc}_{rec}(\phi_h)}{Acc(\phi_h)}$. In this case the amplitudes extracted should be the ones given by the LEPTO generator, due only to the simulation of the gluon radiation, which are less than 1% for both positve and negative hadrons. The amplitudes of the $\cos\phi_h$ modulation calculated from the generated MC hadron distribution N^{mc}_{gen} are shown in fig. 5.25, as an example.

A $\cos\phi_h$ modulation having an amplitude of $-0.5 \cdot z$ has been introduced artificially in the azimuthal distribution of the hadron reconstructed in the Monte Carlo sample, to simulate the measured asymmetries. Each reconstructed hadron has been rejected with a random procedure accordingly to the distribution $\{1/(1+a)\} \cdot \{1 - 0.5 \cdot z_{gen} \cdot \cos\phi^{gen}_h\}$, where the values z_{gen} and ϕ^{gen}_h have been calculated from the corresponding generated track.

Thus, the amplitudes of the $\cos\phi_h$ modulation extracted from the reconstructed hadron distributions (using the method described in section 5.1) after the final cuts

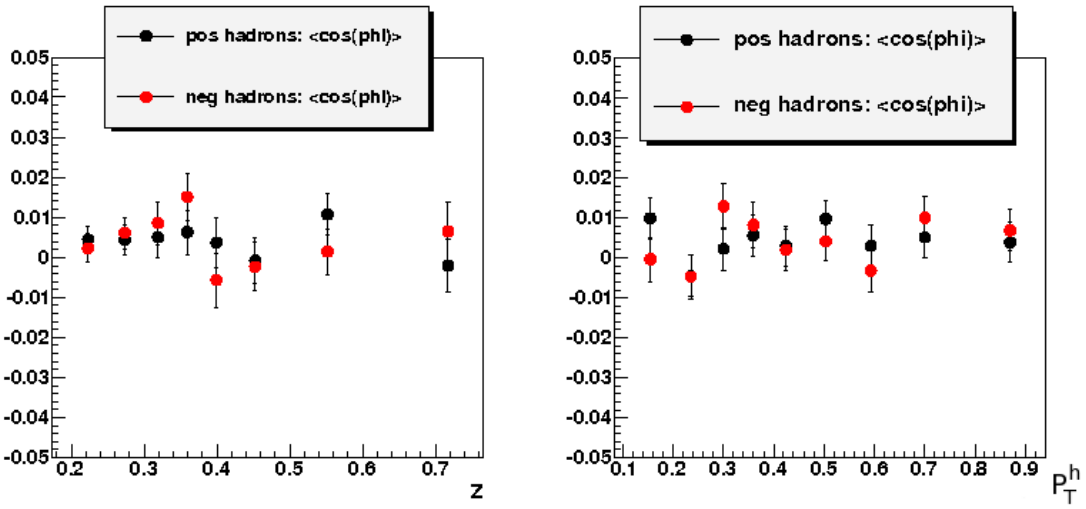

Figure 5.25: Amplitude of the $cos\phi_h$ modulation extracted from the generated MC hadron distribution N_{gen}^{mc} as functions of z(left) and P_T^h(right).

and using the same Monte Carlo to calculate the azimuthal acceptance, should be the same as the one given in input, apart from the azimuthal asymmetries generated in LEPTO and evaluated previously. Indeed the extracted amplitudes should be $-0.5 + A_{gen}$ where A_{gen} are the quantities shown in fig. 5.25, as function of z.

In fig. 5.26 the amplitudes of the $\cos\phi_h^{rec}$ modulation calculated as function of z_{rec} are shown together with the curve representing the input amplitude. It can be seen that the amplitudes obtained are slightly shifted towards less negative values of less than 0.01, accordingly to what is expected. The effect of the smearing is thus very small and it has been neglected in the following.

5.5.4 Detector efficiency

A possible contribution to the azimuthal modulations of the acceptances could be given by some possible detector inefficiencies in regions where there are less redundancies. A MC study was performed in order to search for possible azimuthal modulations in the acceptance assuming that those detectors were switched off during the reconstruction. The ratio between the azimuthal distributions of the hadrons reconstructed with low efficiency and with nominal conditions has been produced in every kinematic bin. From these ratios we have extracted the amplitudes of the azimuthal modulations. Only the $cos\phi_h$ azimuthal modulations have been found to be different from zero, in particular in the high x region where the effect is roughly 3% in the absolute value. This contribution is included in the calculation of the systematic errors given in section 5.5.8.

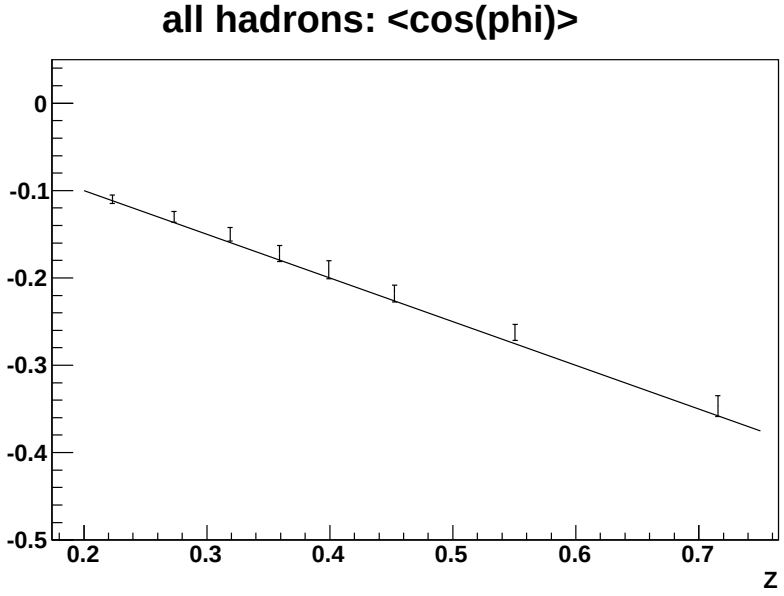

Figure 5.26: The amplitudes of the $\cos\phi_h^{rec}$ modulation calculated as function of the mean value of z_{rec} calculated in each bin. The curve represents the input amplitude.

5.5.5 Acceptance corrections

The asymmetries extracted using the method described in section 5.1 have been measured using the three MC samples. Since the acceptance is reasonably flat in the final kinematical region these results are the same, as shown in fig. 5.27 for positive hadrons and in fig. 5.28 for negative hadrons.

The difference between the amplitudes extracted from the data corrected with the acceptance extracted using the 3 different MC samples (mc0, mc1, mc2) has been used to evaluate the systematic errors. The quantities

$$\frac{|\epsilon_i A_i^{mc1} - \epsilon_i A_i^{mc0}|}{2}; \tag{5.24}$$

and

$$\frac{|\epsilon_i A_i^{mc1} - \epsilon_i A_i^{mc2}|}{2}; \tag{5.25}$$

are calculated for the 3 amplitudes, for each kinematic bin i and for positive and negative hadrons separately. The mc1 is used as reference and it is the MC sample used to extract the final results. These two contributions are added together and the results, in units of the statistical errors of the corresponding amplitude, are used in the calculation of the systematic errors.

5.5.6 Fit procedure

The χ^2 distribution of the fits, performed to extract the asymmetries both for positive and negative hadrons using the function of equation 5.22, is shown in fig. 5.29.

The expected curve of a χ^2 distribution with 10 degrees of freedom is superimposed.

The shape of the distribution does not change by adding in the fitting function different azimuthal modulations, which are not expected from the cross-section. The additional amplitudes have been found to be compatible with zero and the results for the physical asymmetries did not change.

5.5.7 Period compatibility

The results from the data collected in the different subperiods with transversely polarized target have been compared finding a good compatibility. The data taken in 2004 with the longitudinally polarized target have also been used to extract the unpolarized asymmetries. The conditions of the spectrometer were different, starting from the magnetic field in the target region and the tuning of the triggers. Dedicated MC simulations were developed in other analysis and they have been used to extract the acceptance. The ratio between the real and the simulated data are shown in figure 5.30. The asymmetries have been obtained with the same kinematical selection as for the transverse data and the measured azimuthal distributions have been corrected using the "integrated" acceptance.

The comparison between the results from the transverse data and from the longitudinal data is shown in fig. 5.31, for the positive hadrons and in fig. 5.32, for the negative hadrons. As can be seen the agreement is satisfactory.

The absolute value of the semi difference of the results from transverse and longitudinal data has been used as a further contribution the systematic error. These quantities are calculated separately for positive and negative hadrons in each bin i of the kinematic variables x, z and P_T^h. The results in units of the statistical errors are used in the calculation of the systematic errors.

The comparison with the asymmetries measured from the 2006 data is described in section 5.6.

5.5.8 Systematic errors

The relevant contributions to the systematic error have been found to be those due to the acceptance corrections and the period compatibility. The ones given by the detector response simulation have also been included in the systematic errors though they are smaller. The sum in quadrature of the contributions described in section 5.5.4, 5.5.5 and 5.5.7 has been calculated in each kinematic bin. The resulting systematic error, normalized to the statistical uncertainty, is shown in fig. 5.33 for positive hadrons and in fig. 5.34 for negative hadrons.

Since there is no evident trend in both fig. 5.33 and fig. 5.34 we estimate the total systematic error as the mean over all the bins, namely to be a factor of 2 larger than the statistical error. In the plots giving the final results, the systematic uncertainties are shown as bands.

5.6 Results from 2006 data

The amplitudes $\epsilon_1 A_{\cos\phi_h}$, $\epsilon_2 A_{\cos 2\phi_h}$ and $\epsilon_3 A_{\sin\phi_h}$ have also been extracted using the data collected during 2006 at the same energy and with the longitudinally polarized ^{6}LiD target. The experimental apparatus was upgraded in 2005 [51] and one of the most important improvements concerned the polarized target solenoid which was replaced by the new one with a larger angular acceptance, now as foreseen by the proposal. Also new detectors (like ECAL1) were added and the electromagnetic calorimeters were included in the trigger. Only very preliminary results for the unpolarized asymmetries have been so far obtained from these data and the study of the systematics has been just started. The asymmetries have been measured with the same final cuts used for the 2004 data and using the method described in section 5.1. The results are shown in fig. 5.35 (for positive hadrons) and in fig. 5.36 (for negative hadrons), together with the results from the 2004 transverse data. In general the comparison is good and the kinematical trends in x, z and P_T^h are similar both for positive and negative hadrons. For the $\cos 2\phi_h$ and the $\sin\phi_h$ amplitudes the agreement is good and no systematic different can be seen. On the contrary the values for the $\cos\phi_h$ amplitudes from the 2006 data are systematically lower.

As already told, these data have been analysed only recently, the simulation of the calorimeters has to be refined, and more studies on the possible systematic effects are needed. The results of this analysis are encouraging and the work will go on since these data should allow to release the cuts described in section 5.3.2 (mainly done to control the acceptance corrections) taking advantage of the larger acceptance and thus reach higher x values.

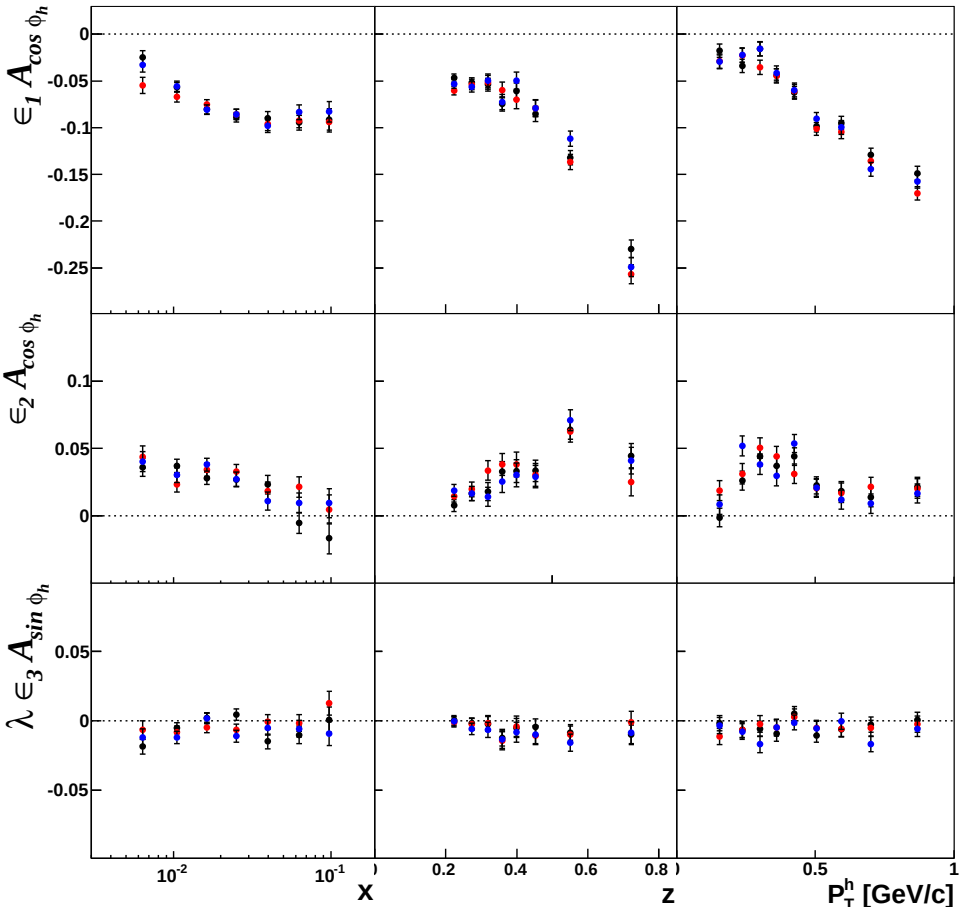

Figure 5.27: Comparison between $\epsilon_1 A_{\cos\phi_h}$ (first row), $\epsilon_2 A_{\cos 2\phi_h}$ (second row) and $\lambda_l \epsilon_3 A_{\sin\phi_h}$ (third row) for positive hadrons as functions of x (first column), z (second column), and P_T^h (third column) extracted using mc0 (black points), mc2 (red points) and mc1(blue points).

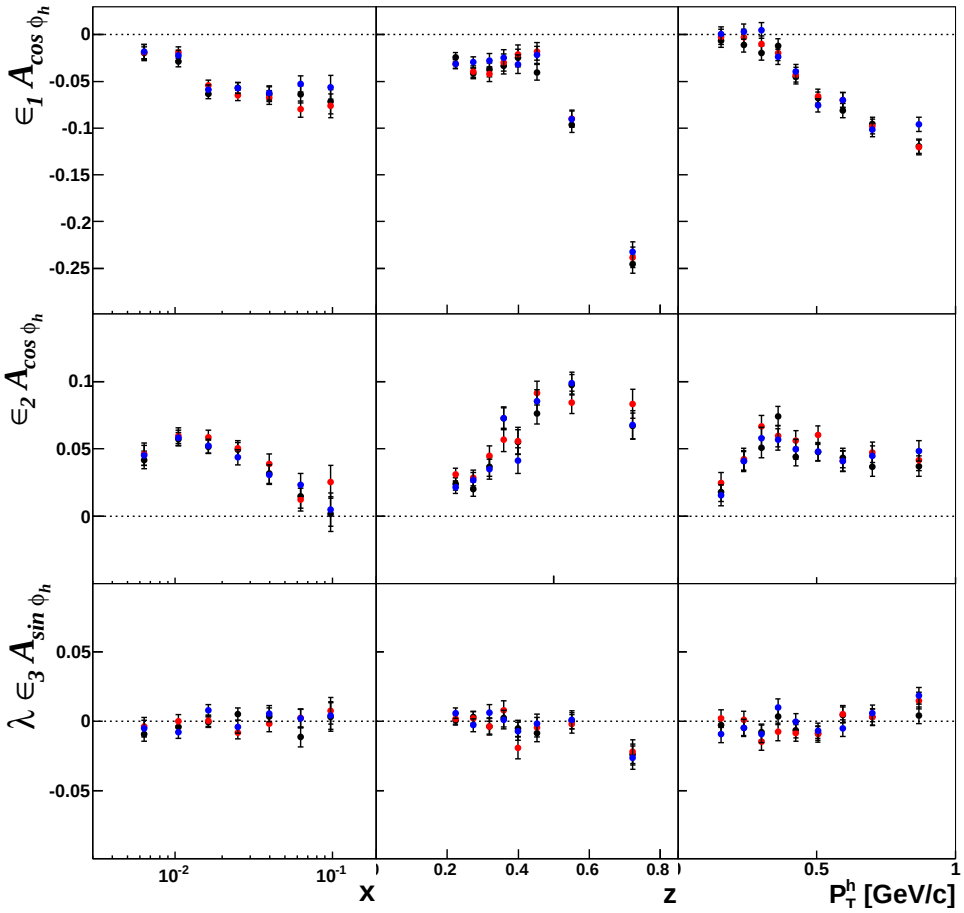

Figure 5.28: Same as fig. 5.27 but for negative hadrons.

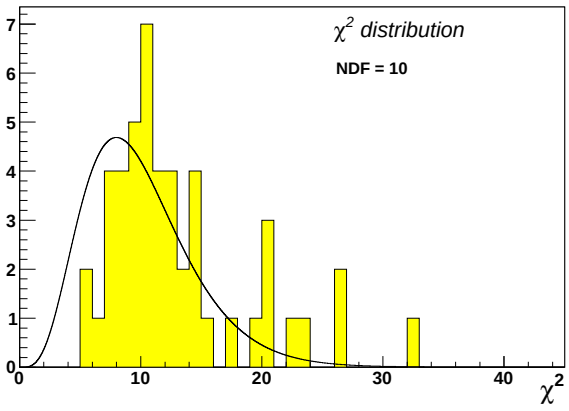

Figure 5.29: The χ^2 distribution of all the fits (both for positive and negative hadrons). The expected curve of a χ^2 distribution with 10 degrees of freedom is superimposed.

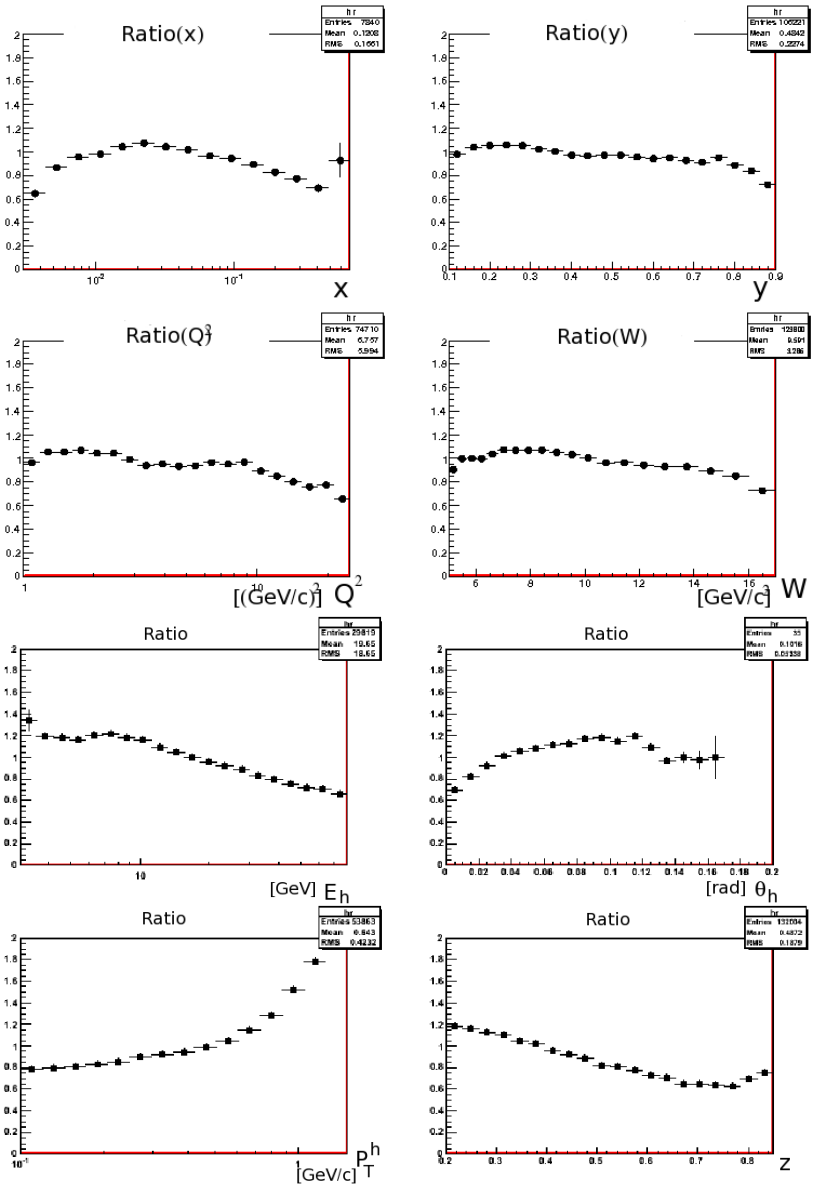

Figure 5.30: Ratios between kinematic distributions for the longitudinal real data (W40) and the simulated data.

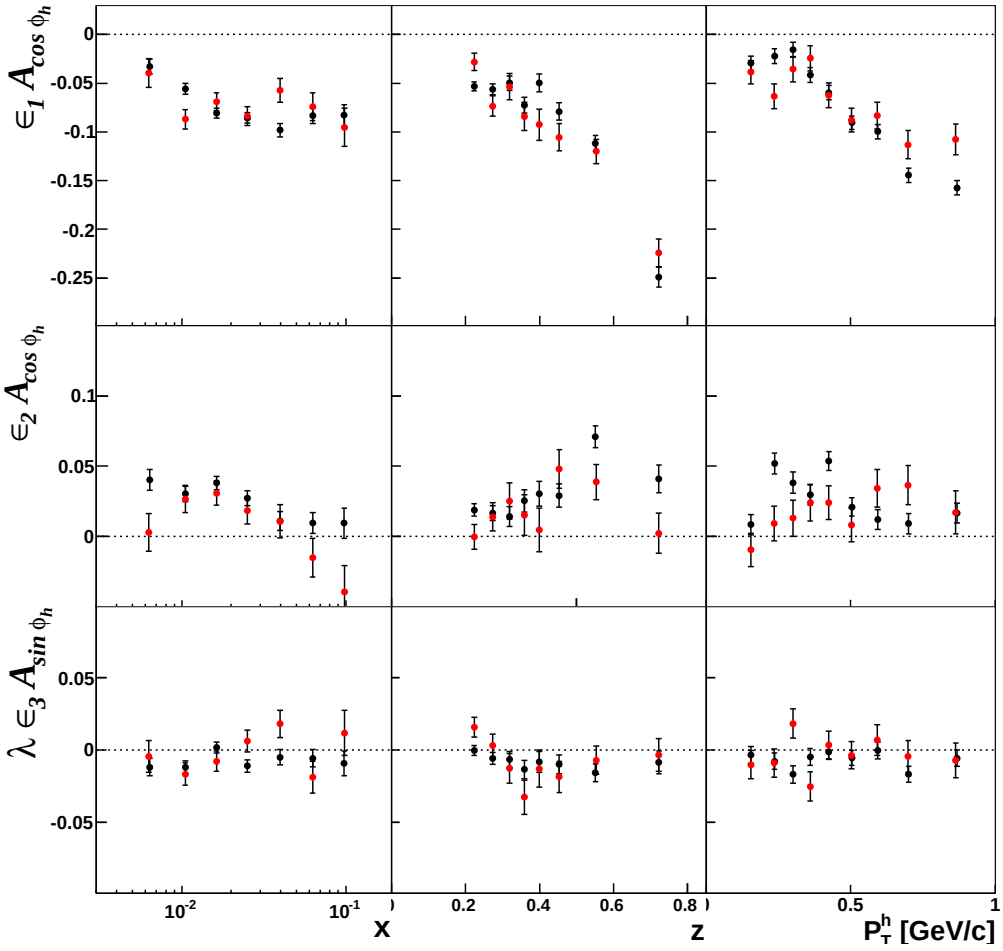

Figure 5.31: Amplitudes of the azimuthal modulations extracted for positive hadrons from transverse data (black points) and from longitudinal data (red points) as a function of x (left column), of z (central column) and of P_T^h (right column). $\epsilon_1 A_{\cos\phi_h}$) on the first row, $\epsilon_2 A_{\cos 2\phi_h}$ on the second row and $\lambda_l \epsilon_3 A_{\sin\phi_h}$) on the third row. The amplitudes have been extracted after the final kinematical selection.

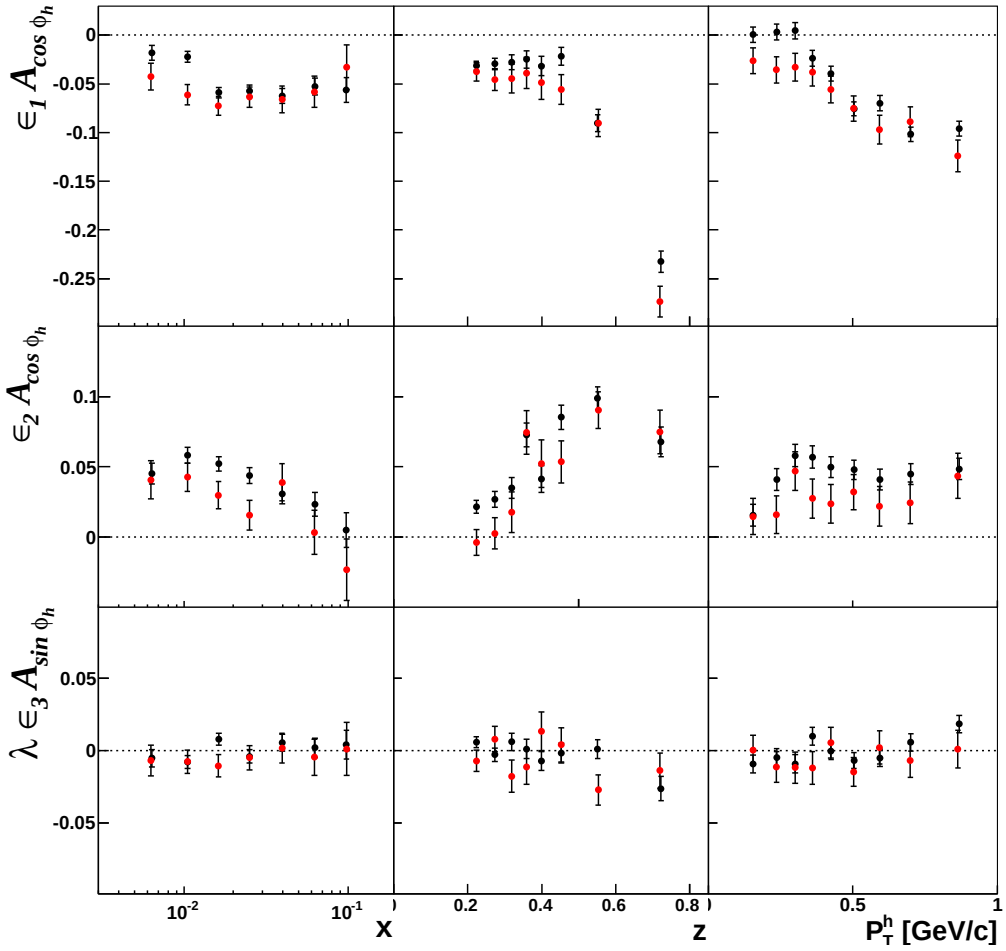

Figure 5.32: same as fig.5.31 but for negative hadrons.

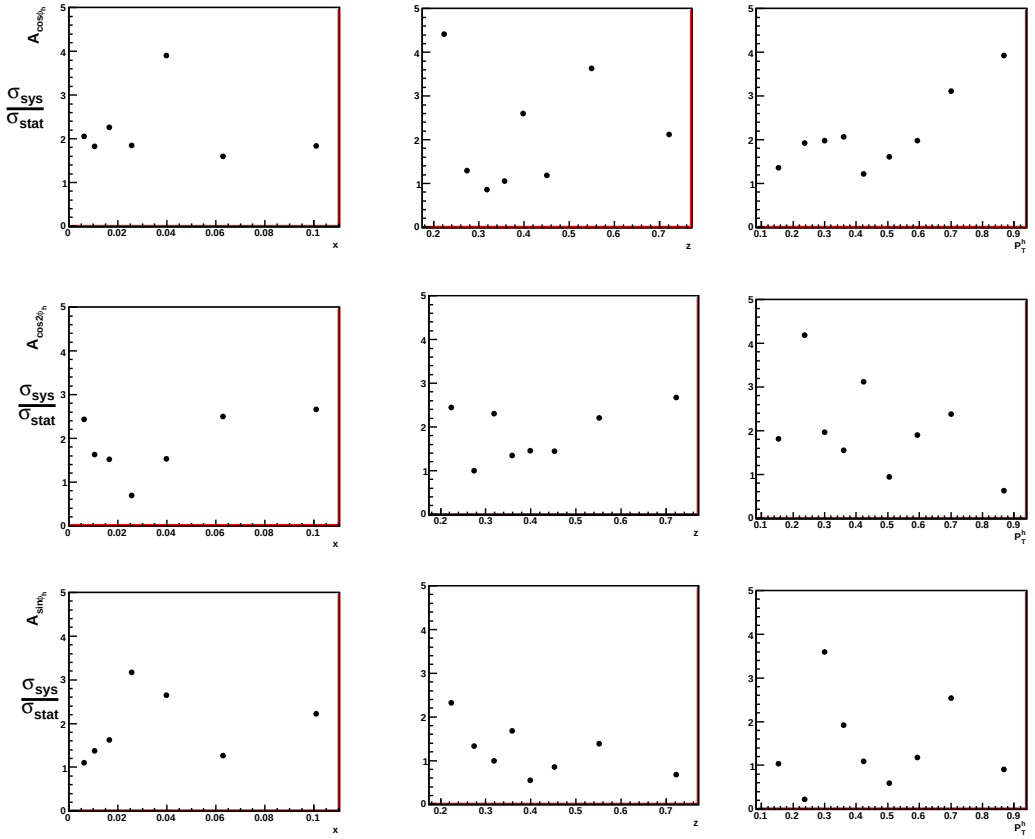

Figure 5.33: Estimation of the systematical error for positive hadrons for $A_{\cos\phi_h}$ (top row), for $A_{\cos 2\phi_h}$ (middle row) and $A_{\sin\phi_h}$ (bottom row) in the x (left column), z (middle column) and P_T^h (right column) kinematical bin.

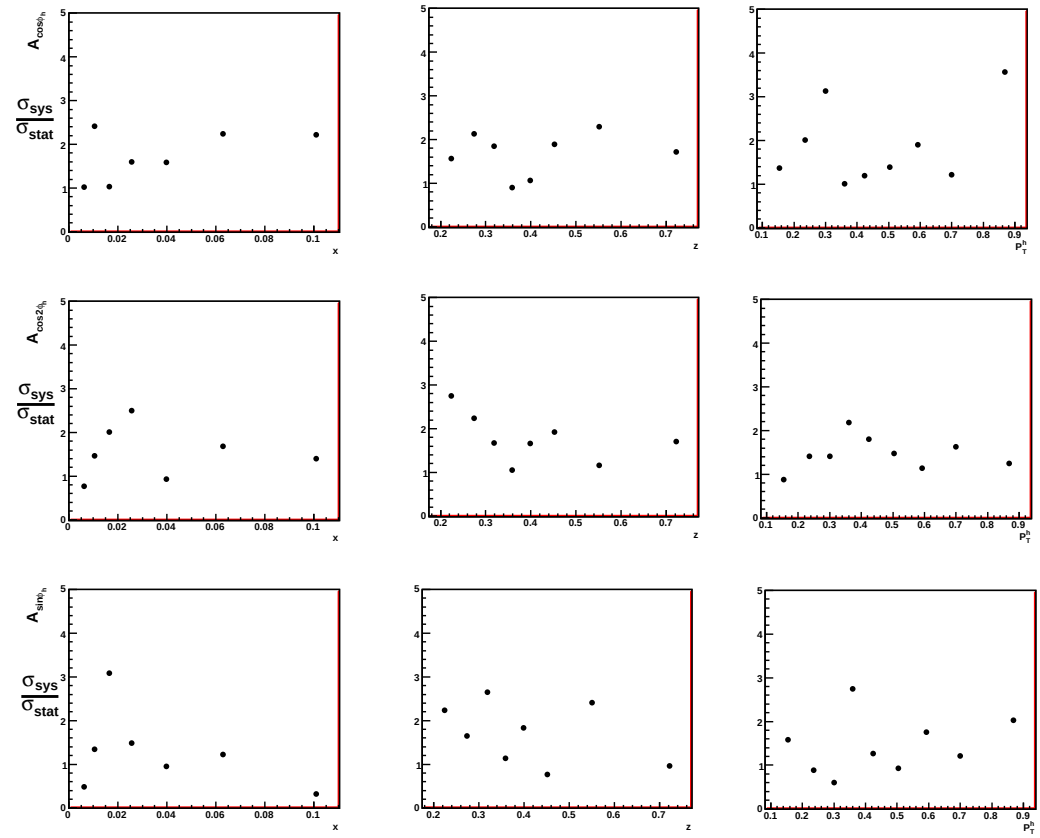

Figure 5.34: same as fig.5.33 but for negative hadrons.

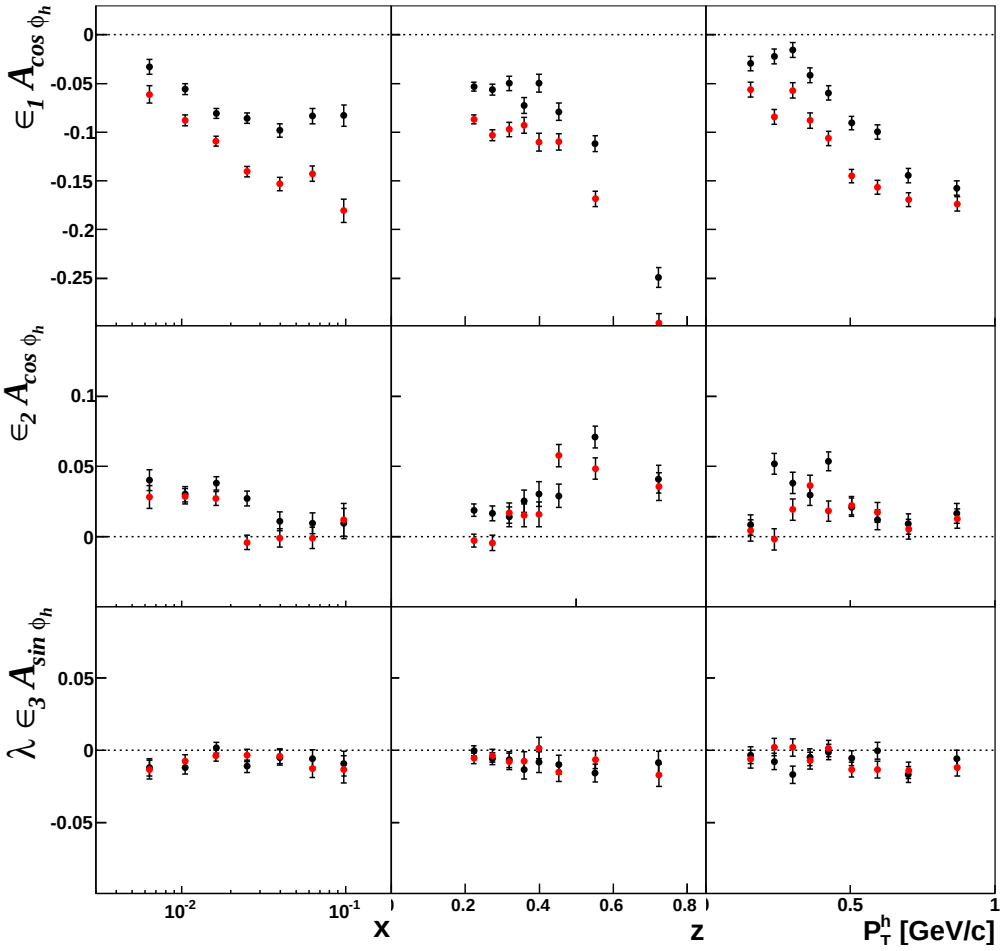

Figure 5.35: Comparison between the asymmetries extracted from 2004 transverse data (black points) and 2006 longitudinal data (red points). The amplitudes $\epsilon_1 A_{\cos\phi_h}$ (top row), $\epsilon_2 A_{\cos 2\phi_h}$ (middle row) and $A\epsilon_3 \sin\phi_h$ (bottom row) are shown as functions of x (left column), of z (central column) and of P_T^h (right column). The amplitudes have been extracted after the final kinematical selection.

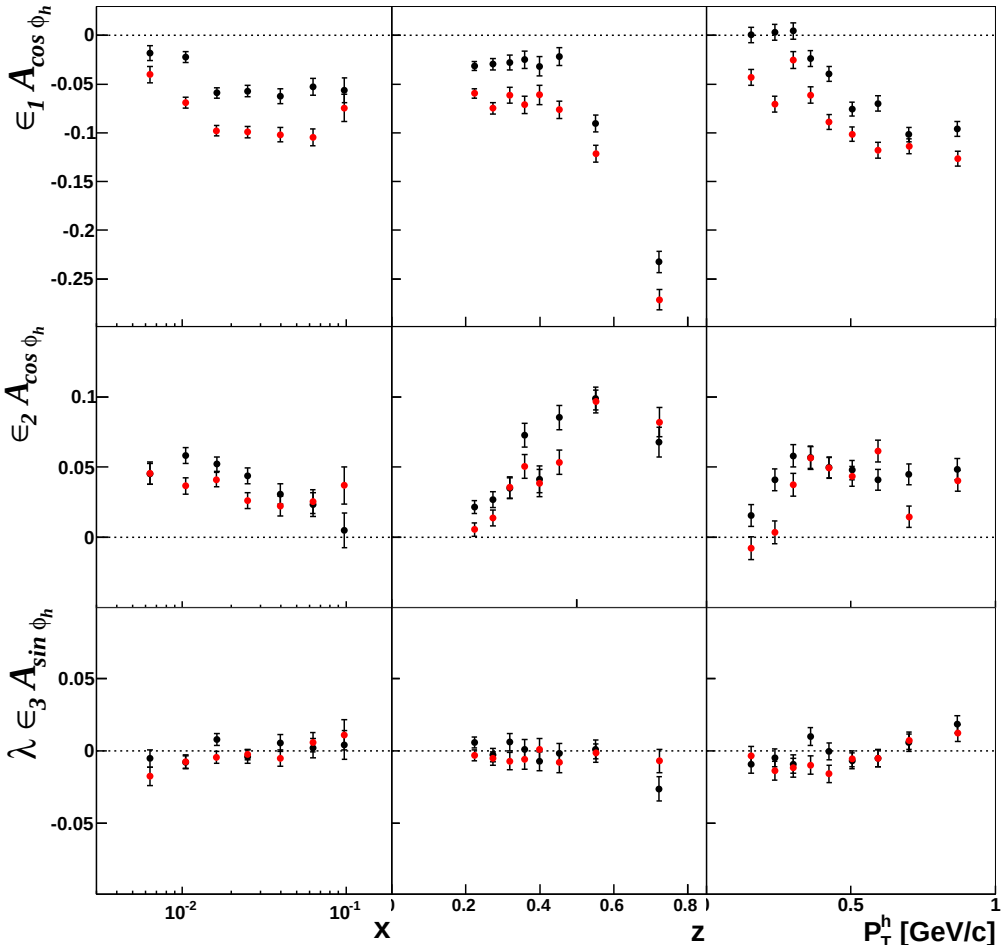

Figure 5.36: Same as fig. 5.35 but for negative hadrons

Chapter 6

Final results for the azimuthal asymmetries on unpolarized deuteron target

In this chapter the results on the azimuthal asymmetries on the unpolarised deuteron target, obtained as explained in chapter 5, will be illustrated and compared with the results of other experiments.

6.1 COMPASS results

The final azimuthal asymmetries have been measured using the data collected in 2004, during the last part of the run, with the transversely polarized ^{6}LiD target and which were the most stable data. Only events with primary vertex in the downstream target cell have been used to minimize acceptance effects. Data with opposite target polarization have been combined in order to compensate for possible transverse spin asymmetries which, by the way, have been measured from the same data and turned out to be compatible with zero [26]. The method described in section 5.4 has been used to extract the amplitudes and the hadrons have been selected requiring:

- $Q^2 > 1$ GeV^2 ,
- $W > 5$ GeV/c^2 ,
- $0.2 < y < 0.9$,
- $x < 0.13$ and $x > 0.003$,
- $0.1 < P_T^h < 1.$ GeV/c,
- $0.2 < z < 0.85$.

The results are shown in fig. 6.3 for the $A_{\cos\phi_h}$ amplitude, in fig. 6.4 for the $A_{\cos 2\phi_h}$ amplitude, and in fig. 6.5 for the $A_{\sin\phi_h}$ amplitude. They are shown separately for positive (top) and negative (bottom) hadrons and are given as functions of x, z or

P_T^h. The bands correspond to the systematic errors
The largest signal has been found in the $A_{\cos\phi_h}$ amplitude: negative, up to 15% in absolute value and with a strong dependence both on z and P_T^h. The dependence on x is less evident and its interpretation should take into account the correlation between x and Q^2, shown in fig. 6.1. The $A_{\cos\phi_h}$ asymmetry should be mainly due to the Cahn effect and the unexpected dependence of the results from the charge of the produced hadron could hint both to a different value of the intrinsic transverse momentum $k_\perp$ for the u and the d quarks or to the Boer-Mulders TMD PDF. This function appears in this asymmetry as an higher twist effect while comes at leading twist in the $A_{\cos 2\phi_h}$ amplitude, where it is expected to give a relevant contribution. Particularly interesting are the trend as function of z (almost constant for up to 0.5 and quickly increasing for $z > 0.5$) and P_T^h (constant, increasing, constant) not expected on the basis of equations 2.31 of chapter 2.
The $A_{\cos 2\phi_h}$ asymmetries are smaller and show a strong trend as function of all the three studied kinematical variables x, z or P_T^h. The dependence of $A_{\cos 2\phi_h}$ on the hadron charge is clearly seen and could be related to the Boer-Mulders function and thus to an important role of the correlation between the intrinsic transverse momentum and spin of the quarks inside the nucleon.

The $A_{\sin\phi_h}$ azimuthal asymmetries show a positive signal for the positive hadrons while they are compatible with zero for the negative ones. The strength of the signal for positive hadrons is roughly constant in x and increases from small to large z values.

6.2 Comparison with other experiments

First measurements of the azimuthal asymmetries in SIDIS on the unpolarized target have been done by the EMC Collaboration [36, 37]. In parallel the E665 [38] and ZEUS [39] Collaborations measured them at much higher energies and in a kinematical region where the pQCD corrections are expected to be dominant.

Recently, besides COMPASS, at lower energies also the HERMES [68,69] and the CLAS [71, 72] Collaborations measured those asymmetries in the small P_T^h region where the effects of the intrinsic transverse momentum of the quarks should be dominant.

6.2.1 EMC

Results has been published for two sets of data [36] obtained using 120 and 280 GeV/c μ^+ beam on unpolarized proton.

The first measurement have been done asking for $Q^2 > 2$ (GeV/c)^2 and $60 < W^2 < 160$ GeV^2/c^4 (this is the one with the kinematical range more similar to the one of COMPASS even if the range of P_T^h extends to almost 4 GeV/c) and for $Q^2 > 5$ (GeV/c)^2 and $160 < W^2 < 360$ GeV^2/c^4. The amplitudes $A_{\cos\phi_h}$ measured as function of z in the two different W^2 regions are shown in fig. 6.6 (no charge separation has been done due to the lack of statistics). The measured amplitudes are negative, of the order of 10% in absolute value. The z dependence is different in the two kinematical region: linear for lower W^2 and first increasing and then constant

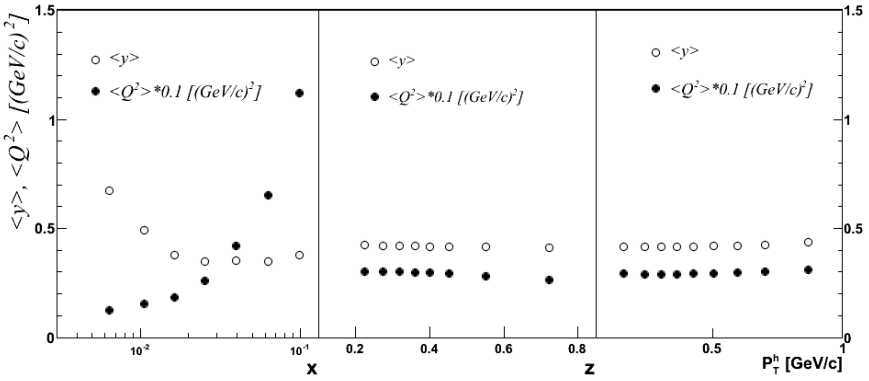

Figure 6.1: $< y >$ and $< Q^2 >$ mean values as functions of x, z and P_T^h. The $< Q^2 >$ mean value has been multiplied by a factor 10^{-1}.

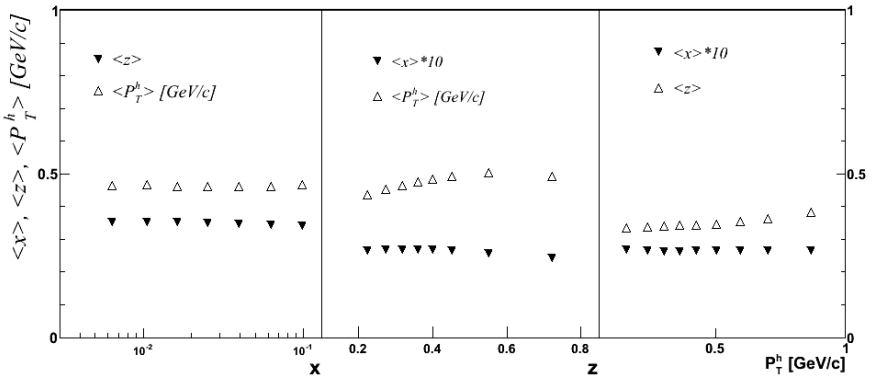

Figure 6.2: $< x >$ and $< z >$ and $< P_T^h >$ mean values calculated for the same intervals as in fig.6.1.

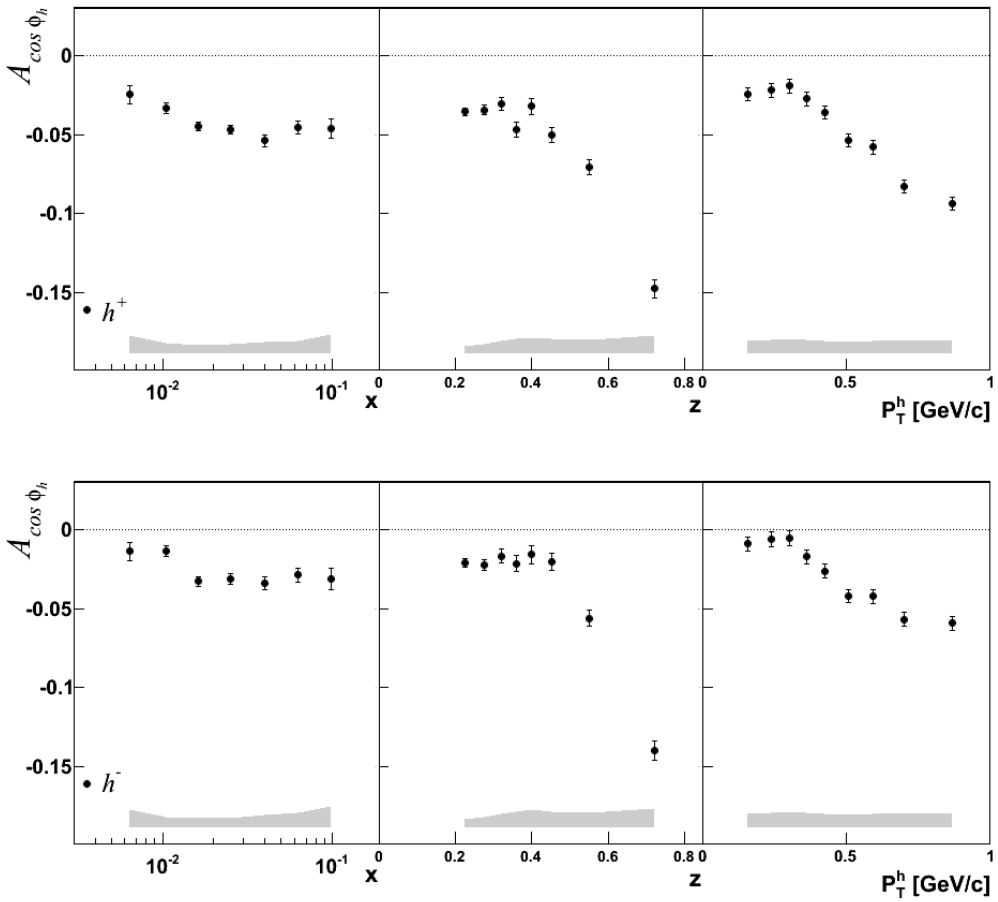

Figure 6.3: The $A_{\cos\phi_h}$ azimuthal asymmetries as functions of x, z and P_T^h, obtained for positive hadrons (upper plot) and negative hadrons (lower plot). Grey bands are the systematic error ($\sigma_{sys} = 2 \cdot \sigma_{stat}$).

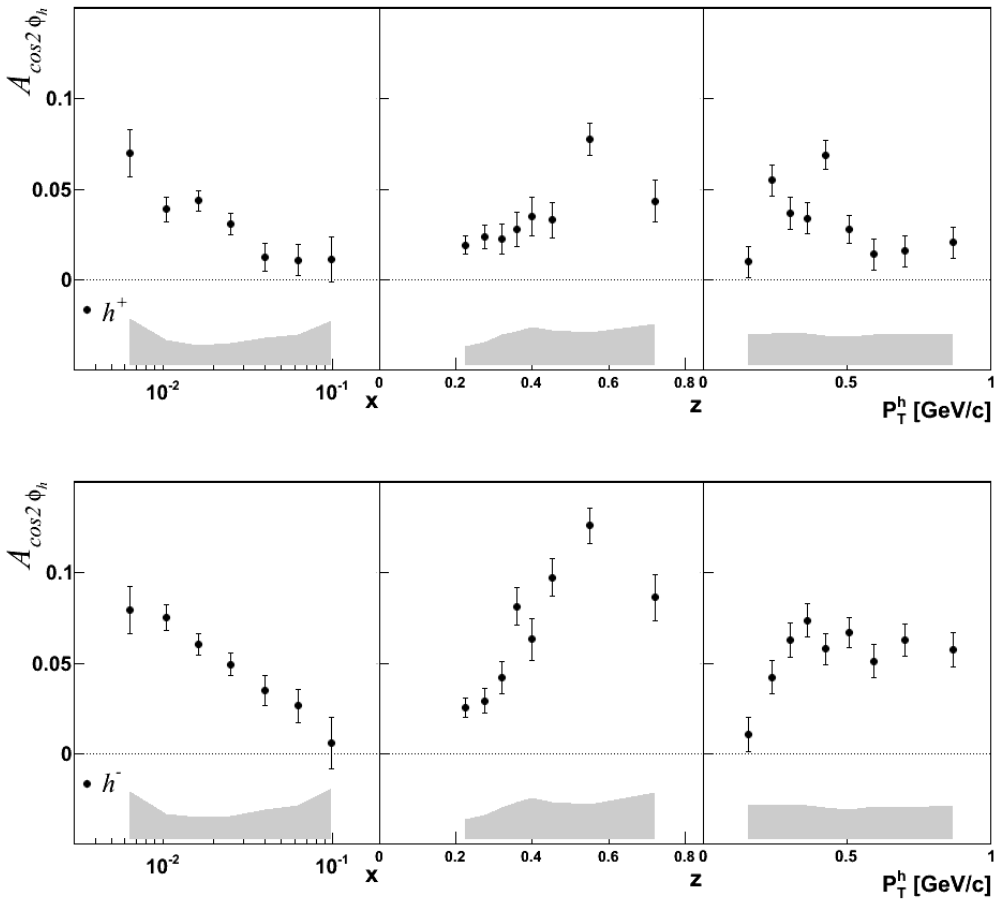

Figure 6.4: The $A_{\cos 2\phi_h}$ azimuthal asymmetries as functions of x, z and P_T^h, obtained for positive hadrons (upper plot) and negative hadrons (lower plot). Grey bands are the systematic error ($\sigma_{sys} = 2 \cdot \sigma_{stat}$).

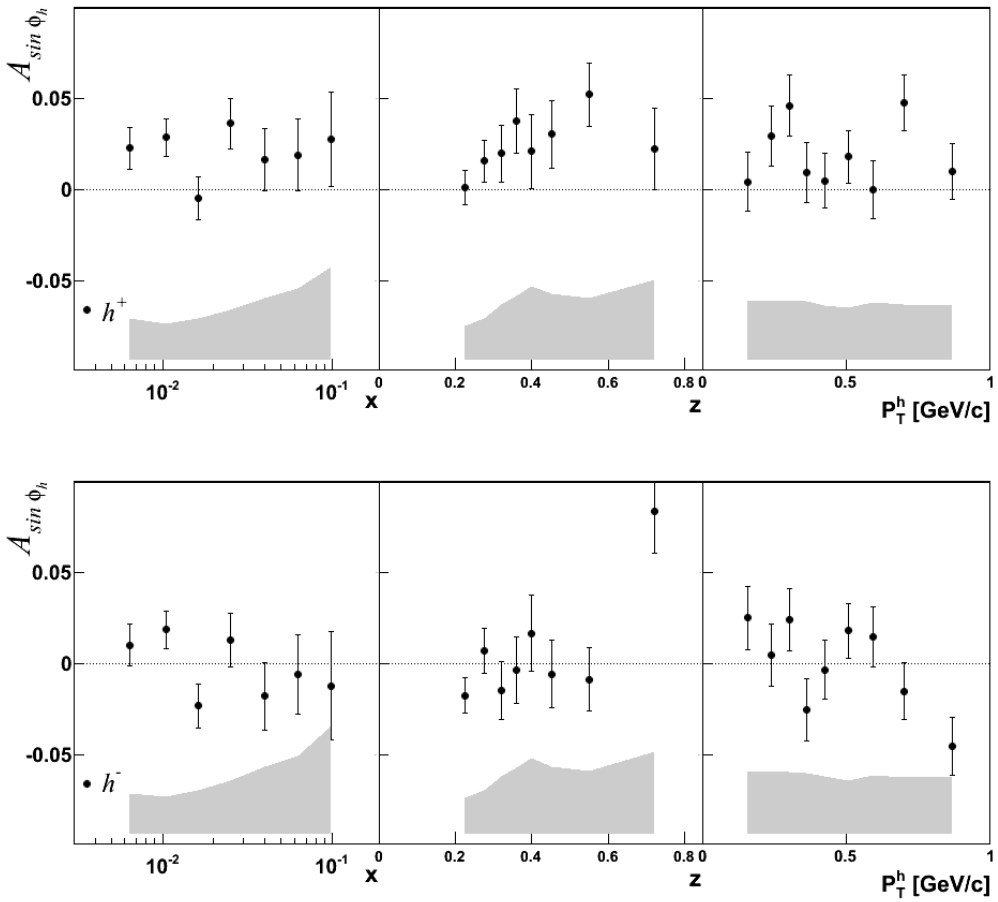

Figure 6.5: The $A_{\sin\phi_h}$ azimuthal asymmetries as functions of x, z and P_T^h, obtained for positive hadrons (upper plot) and negative hadrons (lower plot). Grey bands are the systematic error ($\sigma_{sys} = 2 \cdot \sigma_{stat}$).

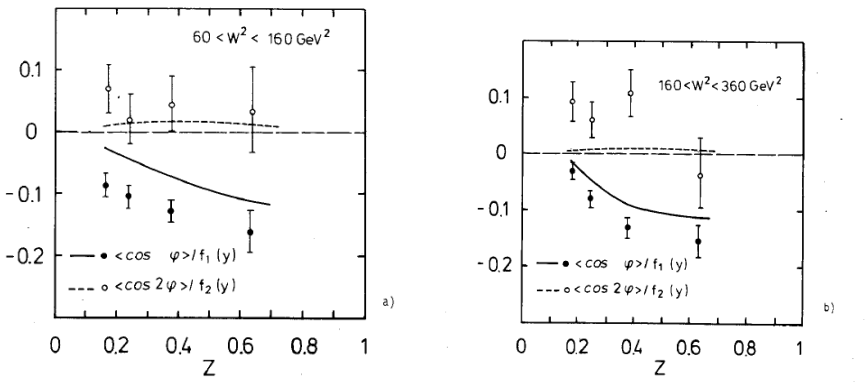

Figure 6.6: Amplitudes $A_{\cos\phi_h}$ measured as function of z at EMC [36] in the two different kinematical regions. The signal is negative and of the order of 10% in absolute value. The z dependence is different in the two kinematical region: linear for lower W^2 (left plot) and first increasing and then constant for the upper W^2 region (right plot).

for the upper W^2 region. The curves are theoretical calculation [33] taking into accounts pQCD effects and an intrinsic transverse momentum of the quark $< k_\perp^2 >$ of ~ 0.4 (GeV/c)^2. The sharp change at $z \sim 0.5$, observed in COMPASS, is not there and there is no evidence of the constant trend for the low z region.

A different picture seems to appear in the measurements of $A_{\cos\phi_h}$ [37] as function of $x_F = 2p_L/W$ (where p_L is the longitudinal momentum of the hadron relative to the virtual photon) which is strongly correlated with z (for positive x_F) in the $Q^2 > 4$ (GeV/c)^2, $40 < W^2 < 450$ GeV^2/c^4 kinematical region. It is interesting to see that the amplitudes, shown in fig. 6.7, are roughly constant in the region $0 < x_F < 0.4$ and seem to increase for $x_F > 0.5$.

Results for $A_{\cos 2\phi_h}$ and $A_{\sin\phi_h}$ have been found to be compatible with zero within the experimental statistical accuracy.

6.2.2 HERMES

The HERMES Collaboration has recently produced [68] preliminary results for the $\epsilon_1 \cdot A_{\cos\phi_h}$ and $\epsilon_2 \cdot A_{\cos 2\phi_h}$ on the unpolarized deuteron (and proton) target and using a 27.5GeV electron beam. The kinematical cuts applied in the event and hadron selection are: $Q^2 > 1$ (GeV/c)^2, $10 < W^2 < 50$ GeV^2/c^4 $0.023 < x < 0.27$, $0.3 < y < 0.85$, $0.2 < z < 0.75$, and $0.05 < P_T^h < 1.0$ GeV/c. To correct for acceptance of the spectrometer, detector smearing, and QED radiative effects, the data were analysed in a 5-dimensional grid in the variables x, y, z, P_T^h and ϕ_h. The released asymmetries are the one dimensional projections of the asymmetries in which the other four variables have been integrated over. The HERMES results also have been produced separately for positive and negative hadrons. The quoted systematic errors are $\lesssim 0.03$ for the $\epsilon_1 \cdot A_{\cos\phi_h}$ results and $\lesssim 0.02$ for $\epsilon_2 \cdot A_{\cos 2\phi_h}$ results. A more detailed evaluation of the HERMES systematics can be found in the reference [68].

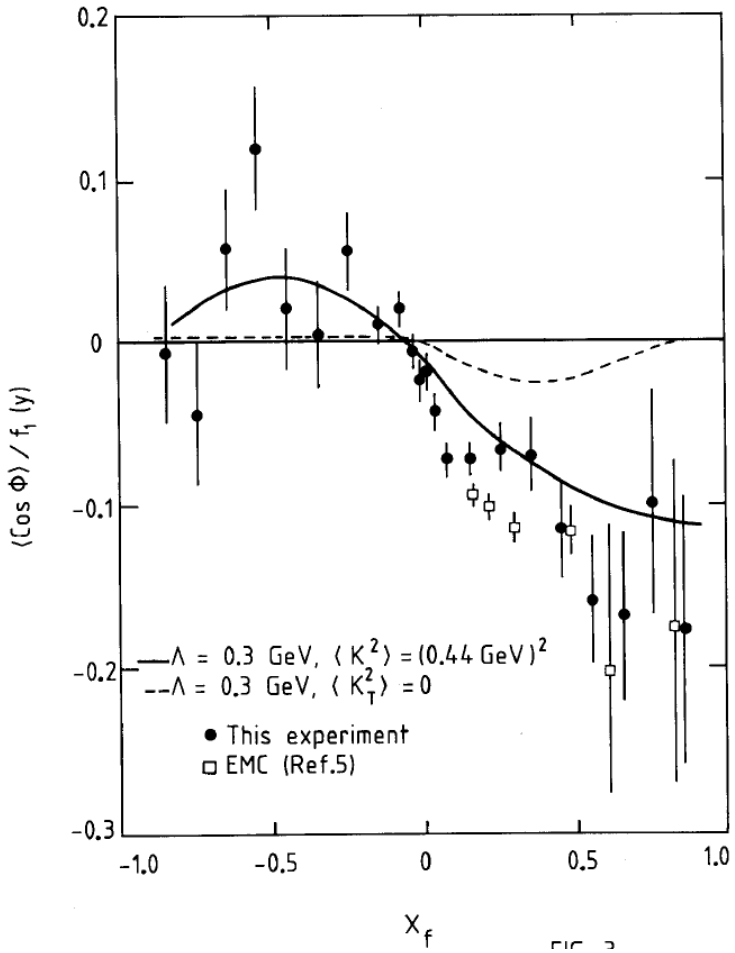

Figure 6.7: $A_{\cos\phi_h}$ amplitudes measured as function of x_F by EMC [37]. Since the strong correlation between x_F and z the trend of this results (in the $0.2 < x_F < 0.8$ region) can be compared with the $A_{\cos\phi_h}$ amplitudes of fig. 6.3, keeping in mind that the EMC results are extracted using positive and negative hadrons together.

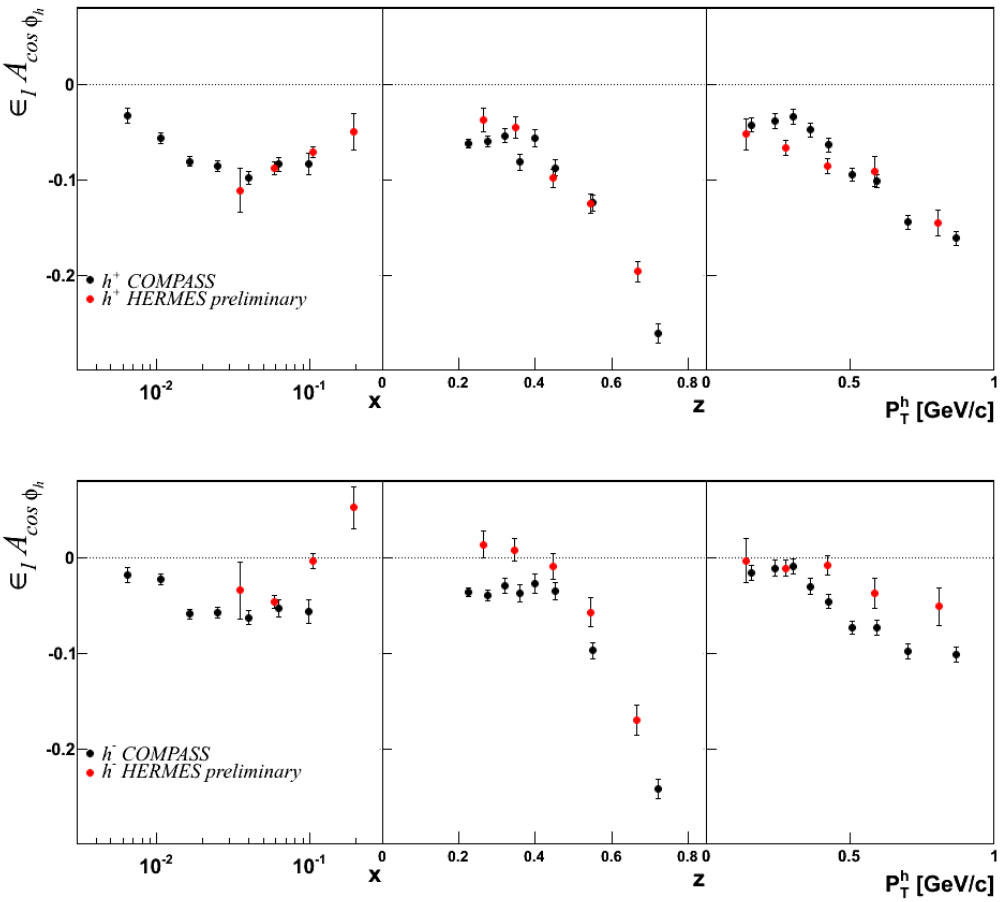

Figure 6.8: Comparison between COMPASS (black points) and HERMES (red points) results for $\epsilon_1 \cdot A_{\cos\phi_h}$ on the unpolarized deuteron target for positive (top) and negative (bottom) hadrons.

The comparison between the COMPASS (black points) and HERMES (red points) results on a deuterium unpolarized target are shown in fig. 6.8 for $\epsilon_1 \cdot A_{\cos\phi_h}$ and in fig. 6.9 for $\epsilon_2 \cdot A_{\cos 2\phi_h}$, as functions of x, z, and P_T^h. The results for positive hadrons are shown on the upper plots and the ones for the negative hadrons on the lower plots.

The $\epsilon_1 \cdot A_{\cos\phi_h}$ amplitudes for positive hadrons are very similar to the ones obtained by COMPASS. Those asymmetries show large and negative signals and the same strong dependencies on z, and P_T^h. The amplitudes measured for the negative hadrons are different in size and the COMPASS results show no hint of a change of sign at high x.

The $\epsilon_2 \cdot A_{\cos 2\phi_h}$ amplitudes for the negative hadrons are compatible in the overlapping x range and seem to have the same trend in z. The results obtained for positive hadrons as function of x are incompatible even if they show a similar kinematical trend as functions of z and P_T^h but the asymmetries have opposite sign. It is interesting to note that the difference between the COMPASS results obtained for positive and negative hadrons is smaller than the one observed by HERMES,

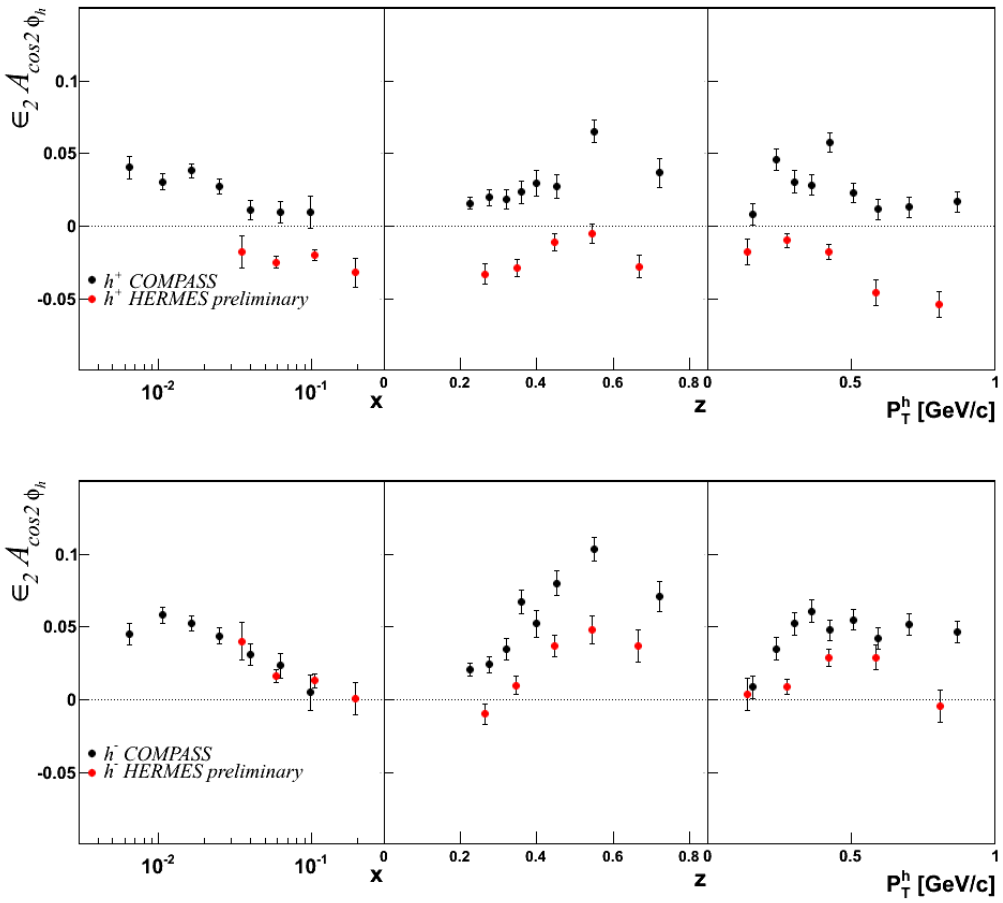

Figure 6.9: Comparison between COMPASS (black points) and HERMES (red points) results for $\epsilon_2 \cdot A_{\cos 2\phi_h}$ on the unpolarized deuteron target for positive (top) and negative (bottom) hadrons.

especially for the $\cos 2\phi_h$ modulation.

A positive signal of the $A_{\sin \phi_h}$ asymmetry for positive hadrons has been measured also by the HERMES Collaboration [70].

All in all there is agreement only for $\cos \phi_h$, positive hadrons, $\cos 2\phi_h$, negative hadrons and $\sin \phi_h$, negative hadrons, amplitudes. The different kinematical range covered by the two experiments must be taken into account when comparing the results. In particular in the region of overlapping, i.e. at high x, the mean value of Q^2 is quite different between the two experiments, being roughly a factor of 3 larger for COMPASS. This is important especially for the higher twist terms which have a $1/Q$ dependence for the twist three, (like the Cahn contribution and the Boer-Mulders one in the $\cos \phi_h$ modulation) or a $1/Q^2$ dependence for the twist four (like the Cahn contribution appearing in the $\cos 2\phi_h$ modulation together with the leading twist Boer-Mulders term). Also, the effect of the different kinematical cuts has to be evaluated. Still presently it is not obvious to understand the discrepancies.

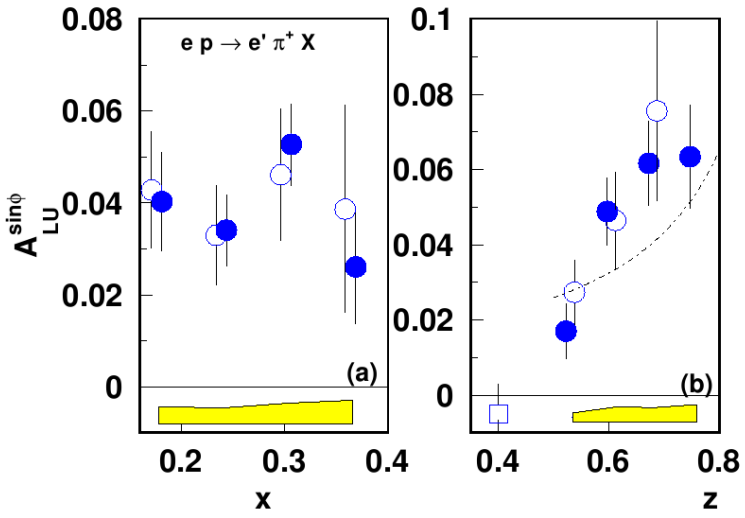

Figure 6.10: CLAS measurements [71] of the $\sin\phi_h$ asymmetry (on π^+) as function of x (left) and z (right).

6.2.3 CLAS

A measurement of the single beam spin asymmetry corresponding to the $\sin\phi_h$ modulation has been measured at CLAS in the electroproductions of positive pions in SIDIS, using a 4.3 GeV beam [71] ($Q^2 > 1$ (GeV/c)^2, $W^2 > 4$ GeV^2/c^4). They measured a small positive amplitude $A_{\sin\phi_h}$ of the order of 0.05, roughly the same strength of the signal measured at COMPASS, in a x region which is complementary to the smaller x region explored by COMPASS. CLAS measured these asymmetries in the $0.5 < z < 0.8$ range and, similarly to what have been observed at COMPASS, the signal increases with z. The amplitude of the $A_{\sin\phi_h}$ modulation has not a clear interpretation in terms of Parton Model and further theoretical work is needed to give an interpretation of this higher twist effect, on the basis of the experimental results.

The CLAS Collaboration has recently [72] produced results for the π^+ azimuthal asymmetries corresponding to the $\cos\phi_h$ and $\cos 2\phi_h$ modulations, using a 5.75 GeV electron beam on a proton target ($1.4 < Q^2 < 5.7$ (GeV/c)^2, $W^2 > 4$ GeV^2/c^4).

The asymmetries have been extracted as functions of z and P_T^h simultaneously and the results as functions of z extracted in different intervals of P_T^h are shown in fig. 6.11.The quantities measured at CLAS are not the same as the ones shown in section 6.1 and the relation (neglecting terms $\sim x^2/Q^2$) are: $A^{CLAS}_{\cos\phi_h} = A_{\cos\phi_h} \cdot \sqrt{1-y}/2 \cdot (2-y)$ (fig. 6.11, right plot) and $A^{CLAS}_{\cos 2\phi_h} = A_{\cos 2\phi_h}/2$ (fig. 6.11, left plot). It has to be noticed that the different energy beam implies a different W range in CLAS and COMPASS and the target and current fragmentation regions are very likely mixed in the CLAS results for $z < 0.4$, making the comparison more difficult.

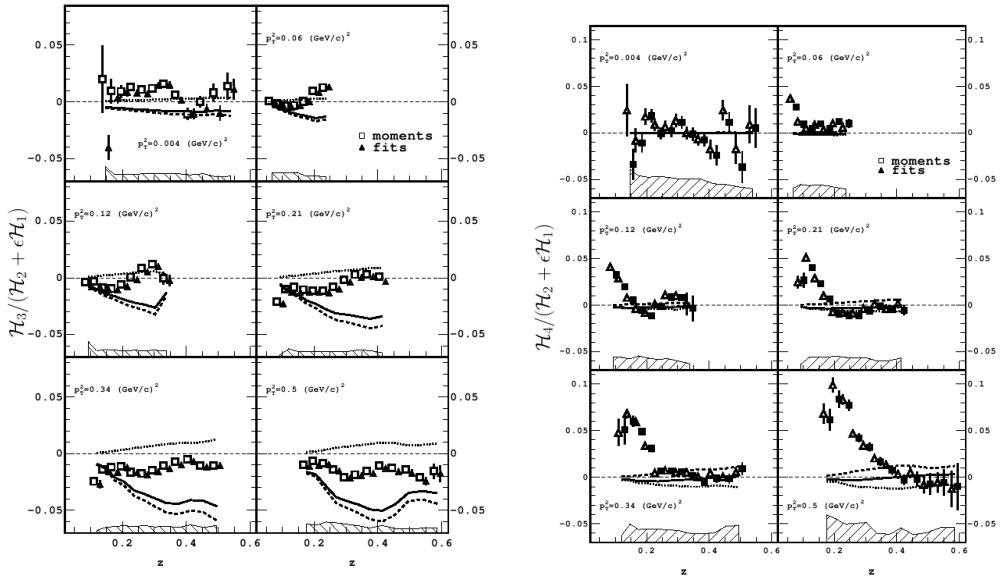

Figure 6.11: CLAS measurements [72] of the $\cos\phi_h$ (left) and $\cos 2\phi_h$ (right) asymmetries as functions of z extracted in different intervals of P_T^h.

6.3 Extraction of the intrinsic transverse momentum from $A_{\cos\phi_h}$

A theoretical calculation of the amplitudes of the $\cos\phi_h$ modulation expected from the Cahn effect in SIDIS (off the unpolarized nucleon) have been presented in [75] together with the first extraction of the mean intrinsic transverse momentum squared ($< k_\perp^2 >$) and of the squared transverse momentum ($< p_\perp^2 >$) in the fragmentation process, from EMC data [37]. The values of $< k_\perp^2 >= 0.25$ (GeV/c)^2 and $< p_\perp^2 >= 0.20$ (GeV/c)^2 have been obtained and checked to be compatible with the differential cross section $d\sigma/dP_T^{h^2}$ measured by EMC [40] in three z intervals. In [76] the effects of the perturbative QCD have been also computed and have been found to be negligible in the region $P_T^h < 1$ GeV/c. The amplitudes of the $\cos\phi_h$ modulation as functions of x, z and P_T^h have been calculated in the COMPASS kinematics for a deuteron target. They have been found sizable and to have a strong dependence on the kinematics. In particular the amplitudes calculated as function of z, calculated in the region $0.2 < z < 0.4$, are sizable and negative ($\sim -20\%$) and show a linear z dependence. This trend is not seen in the COMPASS results, as stressed in section 6.1: the $A_{\cos\phi_h}$ amplitudes extracted as function of z are more or less constant up to $z \simeq 0.5$, where there is an evident increase of the magnitude of the asymmetry. A similar effect has been also seen by EMC [37] for $x_f \simeq 0.5$ as shown in fig. 6.7 and also by HERMES as shown in fig. 6.8.

The interpretation of the results for the $\cos\phi_h$ modulation is not straightforward. An attempt to calculate the contribution coming from the Boer-Mulders function convoluted with the Collins FF has not been made yet, since it is has been thought to be much smaller than the Cahn effect. However the COMPASS (and HERMES) results show a strong dependence of the asymmetries from the charge

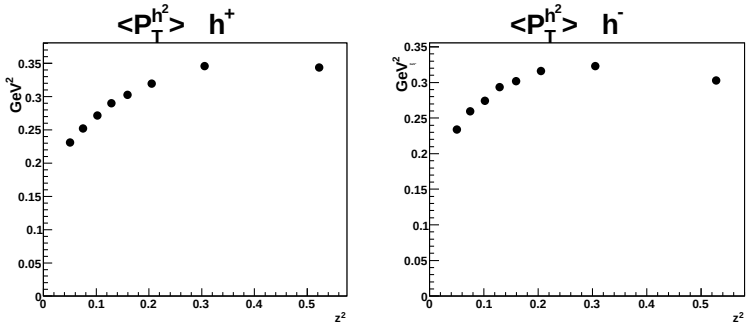

Figure 6.12: $< P_T^{h^2} >$ extracted from the analysed data for positive (left) and negative hadrons (right).

of the hadrons, which could be due to a dependence of the intrinsic transverse momentum of the quark from the flavour or to a contribution from the Boer-Mulders function, different from u and d quarks. Moreover the z dependence of the measured transverse momentum of the hadron expected from the relation of eq. 2.38 $< P_T^{h^2} >= z^2 < k_\perp^2 > + < p_\perp^2 >$ seems to not fit the COMPASS data. The plots of fig. 6.12 show the mean values $< P_T^{h^2} >$ extracted [1] from the analysed data for positive and negative hadrons separately, as function of z^2. It can be seen that there is a qualitative agreement with a linear trend for the first part of the range in z, but it fails for for $z \gtrsim 0.5$.

Similar deviations from that relation has been observed by EMC [35] (as already mentioned in chapter 2) and HERMES [74].

It is anyway interesting to calculate $< k_\perp^2 >$, and eventually $< p_\perp^2 >$, from the amplitudes of the $\cos\phi_h$ modulation measured by COMPASS as a function of z. Starting from the equation of the SIDIS differential cross section 2.6 of chapter 2, after having integrated on ϕ_S, the amplitude $a_{\cos\phi_h}$ ($a_{\cos\phi_h} = \epsilon_1 A_{cos\phi_h}$ in the notation used in chapter 5) can be written as

$$a_{\cos\phi_h} = \frac{\int \frac{2\pi\alpha^2}{xyQ^2}\, 2(2-y)\sqrt{1-y}\, F_{UU,Cahn}^{\cos\phi_h}\, dx\, dy\, dP_T^{h^2}}{\int \frac{2\pi\alpha^2}{xyQ^2}\, \frac{1+(1-y)^2}{2}\, F_{UU}\, dx\, dy\, dP_T^{h^2}}, \tag{6.1}$$

where the integration is performed on the variables x, y and $P_T^{h^2}$ separately in the numerator (NUM) and in the denominator (DEN). Using the relation (from eq. 2.40)

$$F_{UU,Cahn}^{\cos\phi_h} = -\frac{2\, z\, P_T^h\, < k_\perp^2 >}{Q\, < P_T^{h^2} >} \cdot F_{UU} \tag{6.2}$$

[1] The measured values of $< P_T^{h^2} >$ have been divided by a factor I (calculated in appendix A, at the end of this chapter) to be better compared with $z^2 < k_\perp^2 > + < p_\perp^2 >$. This corrections is done because the $P_T^{h^2}$ range in which the means are calculated is limited by the cuts $0.1 < P_T^{h^2} < 1$GeV/c applied in the analysis.

The numerator NUM of eq. 6.1 becomes

$$NUM = < k_\perp^2 > \int \frac{4(2-y)\sqrt{(}1-y)}{1+(1-y)^2} \frac{z\, P_T^h}{Q < P_T^{h^2} >} \tag{6.3}$$

$$\frac{2\pi\alpha^2}{xyQ^2} \frac{1+(1-y)^2}{2} F_{UU}\, dx\, dy\, dP_T^{h^2} \tag{6.4}$$

$$\tag{6.5}$$

where the integrand in eq. 6.4 is proportional (by a factor 2π) to the SIDIS cross section integrated over the azimuthal angles of the hadron ϕ_h and of the spin ϕ_S (denoted as $d^4\sigma$ in the following) and it is the same term which is integrated in the denominator. Thus the amplitude $a_{\cos\phi_h}$ calculated as function of z can be written as

$$a_{\cos\phi_h} =< k_\perp^2 > \frac{\int \frac{4(2-y)\sqrt{(}1-y)}{1+(1-y)^2} \frac{z\, P_T^h}{Q<P_T^{h^2}>} d^4\sigma\, dx\, dy\, dP_T^{h^2}}{\int d^4\sigma\, dx\, dy\, dP_T^{h^2}}, \tag{6.6}$$

and the mean value of the intrinsic transverse momentum of the quark squared can be calculated as

$$< k_\perp^2 >= \frac{a_{\cos\phi_h} < P_T^{h^2} >}{z < 2\,\epsilon_1\, P_T^h/Q >} \tag{6.7}$$

where the definition of ϵ_1 of chapter 5 has been used and the quantities $< 2\,\epsilon_1\, P_T^h/Q >$ and $< P_T^{h^2} >$ are calculated from the hadron distributions measured in each bin of z (possible acceptance effects have been shown to be small in chapter 5 and thus are here neglected).

The results for $< k_\perp^2 >$ extracted using eq. 6.7 are shown in fig. 6.13 (left plot) for positive hadrons (black points) and negative hadron (red triangles). The difference between the $< k_\perp^2 >$ extracted from positive and negative hadrons are a consequence of having considered only the Cahn effect in this calculation and so the different results measured for $a_{\cos\phi_h}$ for different hadron charges can only be due to the flavour dependence of the intrinsic transverse momentum. A dependence of $< k_\perp^2 >$ from the quark flavour has been also been obtained from the $P_T^{h^2}$ dependence of the unpolarized differential cross section measured at COMPASS [81]. The values do not show any particular trend in z and $< k_\perp^2 >$ should not depend upon z as expected from the factorization theorem. Surprisingly the size is of the order of $0.05(\mathrm{GeV/c})^2$, smaller than the values found in [76], $< k_\perp^2 >= 0.28$ $(\mathrm{GeV/c})^2$, and in [77], $< k_\perp^2 >= 0.33$ $(\mathrm{GeV/c})^2$ or used f.i. in the phenomenological analysis of the Sivers asymmetries [78].

Using the values found for $< k_\perp^2 >$, $< p_\perp^2 >$ can be also extracted rearranging equation 6.6 as

$$\frac{z < k_\perp^2 >}{z^2 < k_\perp^2 > + < p_\perp^2 >} \cdot < 2\,\epsilon_1\, P_T^h/Q >= a_{\cos\phi_h} \tag{6.8}$$

thus leading to

$$< p_\perp^2 >= \frac{z < k_\perp^2 >}{a_{\cos\phi_h}} \cdot < 2\,\epsilon_1\, P_T^h/Q > - z^2 < k_\perp^2 > \tag{6.9}$$

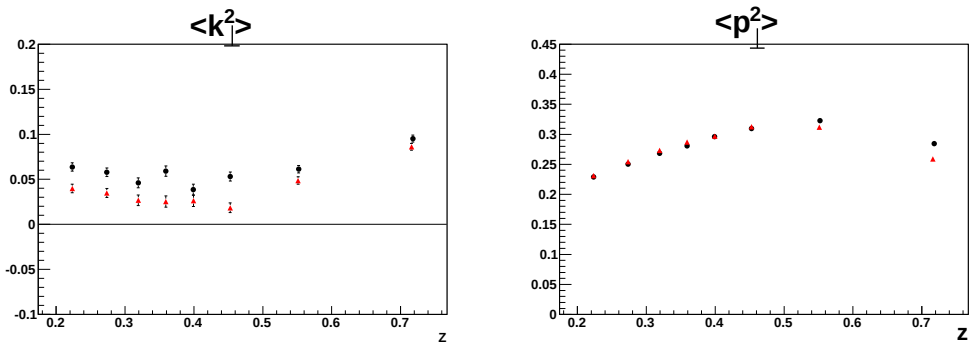

Figure 6.13: Intrinsic transverse momentum of the quark $< k_\perp^2 >$ (left) and transverse momentum of the hadron in the fragmentation $< p_\perp^2 >$ (right) extracted from the measured amplitudes $a_{\cos\phi_h}$ using eq. 6.7 eq. 6.9 respectively as function of z. Black points are the results for positive hadrons and red triangles are for negative hadrons.

The results for $< p_\perp^2 >$ extracted using eq. 6.9 are shown in fig. 6.13 (left plot for positive, black points, and negative, red triangles, hadrons) where a z dependence is clearly seen. The values go from ~ 0.20 (GeV/c)^2) to ~ 0.30 (GeV/c)^2, quite in agreement with the results of [76], $< p_\perp^2 >= 0.25$ (GeV/c)^2 and the values found in [77] $< p_\perp^2 >= 0.28$ (GeV/c)^2. However a dependence of $< p_\perp^2 >$ on z has been not taken into account in these works. It is interesting to note also that the values extracted for positive and negative hadrons are very similar up to $z \gtrsim 0.5$ and the values extracted for negative hadrons are lower for the last two z points.

A somehow unexpected dependence of $< p_\perp^2 >$ on z has already been observed in COMPASS. In [81] a more complex dependence of $< P_T^{h^2} >$ on z has been introduced, allowing a $< p_\perp^2 >$ dependence of the type $(z \cdot (z-1))$, deduced from the acceptance corrected COMPASS data. Such a trend seems to be qualitatively agreement with the ones observed here.

To summarise, the COMPASS data allow to extract $< k_\perp^2 >$ and $< p_\perp^2 >$ with very good precision and for different charges of the hadrons. The result on $< p_\perp^2 >$ shown here is in line with different analysis, both on COMPASS data and data from other experiments. The result on $< k_\perp^2 >$, on the other hand, are somewhat surprising, and considerably smaller than those obtained from other authors. Although some model calculations [79, 80] foresee values as small as 0.08 (GeV/c)^2, it has to be stressed that the work presented here has been finalised only recently and more checks are needed on this part of the analysis.

6.4 Predictions for the Boer-Mulders function

The amplitudes of the $\cos 2\phi_h$ modulation have three different contributions: the correlation between the intrinsic transverse momentum and the spin of the quark, described by the Boer-Mulders function, the twist-4 Cahn effect and the gluon radiation. In [41] all these effects have been separately calculated for a deuteron target

and for the COMPASS kinematics (the cuts used in [41] are also the same as the ones shown in section 6.1, apart from $y > 0.1$ and $z < 1$ cuts, also no upper cut on P_T^h has been used). The contribution coming from the gluon radiation is negligible at small P_T^h ($P_T^h \lesssim 1$GeV/c) while the other two enter with roughly the same magnitude, but with a different hadron charge dependence. The amplitude generated is given by the convolution between the Boer-Mulders TMD PDF $h_1^\perp$ and the Collins FF $H_1^\perp$. Considering only the contributions of the u and d quarks and using the general rule to distinguish *favoured* and *unfavoured* Fragmentation Functions ($D_{fav} \equiv D_{1\,u}^{\pi^+} = D_{1\,d}^{\pi^-}$ and $D_{unfav} \equiv D_{1\,u}^{\pi^-} = D_{1\,d}^{\pi^+}$), the Boer-Mulders (B-M) contribution to the amplitude of the $\cos 2\phi_h$ modulation has been written

$$\begin{aligned} A_{\cos 2\phi_h, B-M}^{\pi^+} &\simeq (h_1^{\perp u} + h_1^{\perp d}) \cdot (4\, H_{1fav}^\perp + H_{1unfav}^\perp) \\ A_{\cos 2\phi_h, B-M}^{\pi^-} &\simeq (h_1^{\perp u} + h_1^{\perp d}) \cdot (H_{1fav}^\perp + 4\, H_{1unfav}^\perp) \end{aligned} \tag{6.10}$$

for the different charges of the produced pions which are more than 90% of the hadrons sample. The azimuthal asymmetries in $e^+\,e^- \to$ hadrons, and of the Collins FFs $H_1^\perp$ have been taken from the global analysis of the BELLE, HERMES and COMPASS measurements of the Collins asymmetries [43] which gave $H_{1unfav}^\perp \simeq -H_{1fav}^\perp$. In reference [41] the parametrization of the Boer-Mulders function has been chosen in analogy to the one used to extract the Sivers function in [42] on the basis of some models calculations, [82] [83] [84] [45], from which the Boer-Mulders function is expected to be have roughly the same (negative) size for the u and d quark. Thus, accordingly to eq. 6.10, the contribution to the amplitude of the $\cos 2\phi_h$ coming from the Boer-Mulders function is expected to have opposite sign for positive and negative hadrons (and also similar size). The amplitude generated by the Cahn effect is given by the convolution between the unpolarized PDF f_1 and the unpolarized FF D_1 and no dependence on the charge is introduced. In reference [41] the intrinsic transverse momentum is assumed to be the same for the u and d quark and the used values are $< k_\perp^2 >= 0.25$ (GeV/c)^2 (and $< p_\perp^2 >= 0.20$ (GeV/c)^2). It has been also shown that a 50% variation of the $< k_\perp^2 >$ value (between 0.125 (GeV/c)^2 and 0.375 (GeV/c)^2) does not change significantly the predictions.

The $\epsilon_2 A_{\cos 2\phi_h}$ amplitudes predicted for positive and negative pions in reference [41] for deuteron target and in the COMPASS kinematics are shown in fig. 6.14 together with the new COMPASS results. The dotted lines are the contributions coming from each effect and the solid red line is their sum. The order of magnitude of the measured asymmetries and of the predicted ones is the same. The predicted kinematical dependence and charge dependence are in good agreement with the measurements and the effect of the correlation between the transverse spin and the transverse momentum of the quark seems to be there.

However it seems to be difficult to reproduce the P_T^h behaviour of $\epsilon_2 A_{\cos 2\phi_h}$ (increasing signal for low P_T^h and then constant), as emerged from [85] where the HERMES results and the COMPASS preliminary results [61] has been used for a first extraction of the Boer-Mulders function.

All in all these first results for the amplitudes of the $\cos 2\phi_h$ modulation are very promising and in general good agreement with the theoretical predictions. Both

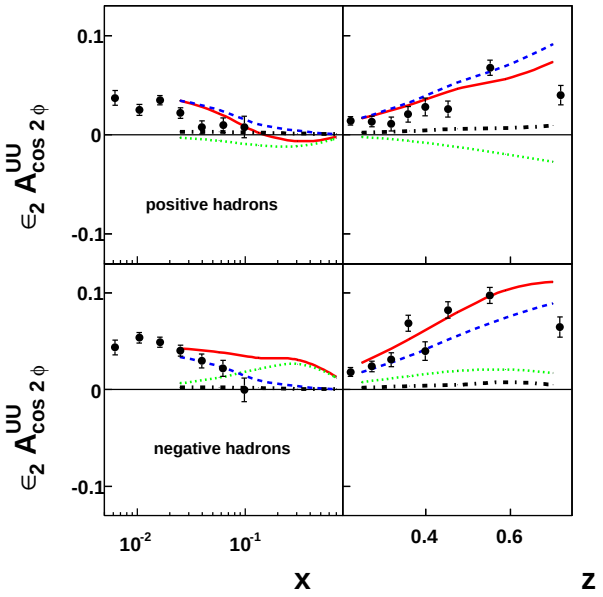

Figure 6.14: Theoretical calculations for the $\epsilon_2 A_{\cos 2\phi_h}$ amplitude as functions of x (left) and z (right) for positive (top) and negative (bottom) pions ($\gtrsim 90\%$ of the analysed hadrons): predictions from [41]. The red solid line is the sum of three different contributions: Boer-Mulder function (green, dotted), Cahn effect (blue, dotted) and pQCD (black-dotted).

the sign and the order of magnitude of the measured signals are as expected, both for positive and negative hadrons, confirming the existence of the Boer-Mulders function. The dependence of the amplitudes from the kinematical variables x and z seems to be at least qualitatively understood, while the P_T^h dependence shows a presently unexpected trend. These results are thus a very interesting input for a more effort to reach a satisfactory description of the mechanism which give the correlation between the intrinsic transverse momentum of the quark and its transverse spin.

6.5 Final considerations

First results on the azimuthal asymmetries in SIDIS, obtained for positive and negative hadrons separately, have been presented in this chapter. The amplitudes of the $\cos\phi_h$, $\cos 2\phi_h$ and $\sin\phi_h$ modulations have been measured in the unique kinematical range explored by the COMPASS experiment, on the ^{6}LiD target. They are related to the inner structure of the nucleon and in particular to the intrinsic transverse momentum of the quark $\vec{k}_\perp$ trough the Cahn effect, and to its correlation with the quark transverse spin, described by the Boer-Mulders TMD PDF.

The measured amplitudes of the $\cos\phi_h$ modulations have been found to be negative and to have the largest signal, as expected from theoretical considerations. However their magnitude, their peculiar dependence on the kinematical variables (especially on z and P_T^h) and the difference for positive and negative hadrons do not have a clear interpretation. The measurements could suggest a more complex role of $\vec{k}_\perp$ in the description of the nucleon and a dependence from the quark flavour, or a possible kinematical dependence (from z) of the transverse momentum of the produced hadron, in the fragmentation process, or a non negligible contribution of the Boer-Mulders term.

A smaller, but definitively different from zero, signal has been measured for the amplitudes of the $\cos 2\phi_h$ modulations. There is room for the existence of a correlation between $\vec{k}_\perp$ and the transverse quark spin, described by the famous and still unknown Boer-Mulders TMD PDF. An accurate analysis, taking into account possible dependence of $< {k^2}_\perp >$ from the quark flavour, could tells if the measured dependence from the hadron charge has to be ascribed to the Boer-Mulders term. Morover the theoretical calculations seem to be in agreement both with the size of the measured asymmetries and their dependence from the kinematical variables, apart for the P_T^h dependence, thus needing more theoretical effort to understand it.

Both for the $\cos\phi_h$ and the $\cos 2\phi_h$ amplitudes preliminary results have been produced by the HERMES experiment for proton and deuteron target. They confirm the large values, the differences for positive and negative hadrons, and the strong z and P_T^h dependence. Still, in some cases, there are discrepancies which need to be understood and higher twist terms, other than the Cahn effect, has still to be calculated.

The amplitudes of the $\sin\phi_h$ modulations, the ones proportional to the beam longitudinal polarization, and related to higher twist effects have not yet a clear interpretation in terms of Parton Model. Thus their measurement is very interesting as it allows to further investigate the complex structure of the nucleon. Particularly

interesting is the small, but positive signal measured for the positive hadrons both at the COMPASS, HERMES and the CLAS experiments, at very different beam energies. Again something which is not well understood by the current theoretical knowledge.

Of course these COMPASS results are very important as they give further inputs for a better understanding of the dynamics of the quarks inside the nucleon. More theoretical efforts are needed to fully explain them together with the recent measurements coming from the other SIDIS experiments (HERMES and CLAS) and a global analysis of these results can hopefully improve the current knowledge of the nucleon structure.

APPENDIX A

The mean value of $P_T^{h^2}$ can be written as

$$< P_T^{h^2} > \;=\; \frac{\int_{P_{T,min}^{h^2}}^{P_{T,max}^{h^2}} dP_T^{h^2}\; P_T^{h^2}\, \frac{d^2\sigma}{dz dP_T^{h^2}}}{\int_{P_{T,min}^{h^2}}^{P_{T,max}^{h^2}} dP_T^{h^2}\, \frac{d^2\sigma}{dz dP_T^{h^2}}} \tag{6.11}$$

where, defining

$$a = z^2 < k_\perp^2 > + < p_\perp^2 > , \tag{6.12}$$

it is

$$\begin{aligned} \frac{d^2\sigma}{dz dP_T^{h^2}} &= C \cdot \frac{e^{-P_T^{h^2}/a}}{\pi\, a} , \\ C &= \int dx\, dy\, d\phi_h\, \frac{d^5\sigma}{dx dy dz d\phi_h dP_T^{h^2}} . \end{aligned} \tag{6.13}$$

Thus

$$< P_T^{h^2} >= \frac{\int_{P_{T,min}^{h^2}}^{P_{T,max}^{h^2}} dP_T^{h^2}\; P_T^{h^2} \cdot \frac{e^{-P_T^{h^2}/a}}{\pi\, a}}{\int_{P_{T,min}^{h^2}}^{P_{T,max}^{h^2}} dP_T^{h^2}\, \frac{e^{-P_T^{h^2}/a}}{\pi\, a}} , \tag{6.14}$$

and using $y = P_T^{h^2}\; a$, $M = P_{T,max}^{h^2}/a$ and $m = P_{T,min}^{h^2}/a$, one has

$$< P_T^{h^2} >= \frac{a\, \int_m^M dy\, y\, e^{-y}}{\int_m^M dy\, e^{-y}} . \tag{6.15}$$

Finally

$$< P_T^{h^2} >= I \cdot \{ z^2 < k_\perp^2 > + < p_\perp^2 > \} , \tag{6.16}$$

where

$$I = \frac{(M+1) \cdot e^{-M} - (m+1) \cdot e^{-m}}{e^{-M} - e^{-m}} \tag{6.17}$$

depends on the limit of integration $M = 1/(z^2 < k_\perp^2 > + < p_\perp^2 >)$ and $m = 0.01/(z^2 < k_\perp^2 > + < p_\perp^2 >)$ which depend on z. Note that $I = 1$ in the case $M = \infty$ and $m = 0$ (and the result for $< P_T^{h^2} >$ is the same as the one derived in appendix A of chapter 2).

Chapter 7

Azimuthal asymmetries on longitudinally polarized target

The measurement of the azimuthal asymmetries expected in the cross section of SIDIS off a longitudinally polarized target is described in this chapter. The data used for this analysis have been collected in COMPASS from 2002 to 2004 using a 160 GeV/c longitudinally polarized muon beam and a ^{6}LiD target with a polarization P_L parallel or anti-parallel to the beam direction. The target polarization P_L almost fully translates into a longitudinal polarization of the nucleon S_L, with respect to the virtual photon direction, but gives also a kinematical suppressed contribution to the transverse component $S_T = P_L \sin(\theta_\gamma)$, where $\sin(\theta_\gamma) \simeq 2M_h/Q\, x\sqrt{(}1-y)$.

In total there are four expected independent azimuthal modulations which can be measured: $\sin\phi_h$, $\sin 2\phi_h$, $\sin 3\phi_h$ and $\cos\phi_h$. The structure functions appearing in the corresponding amplitudes are described in chapter 2. They will be further discussed together with the results, in section 7.5.

7.1 Description of the measurement

The method of the analysis takes advantage of the COMPASS polarized target configuration and data taking procedure. The two target cells are polarized in opposite directions with respect the direction of the target solenoid field which can be set either parallel or anti-parallel to the nominal beam axis. To minimize systematic effects caused by possible time dependent variations of the apparatus acceptance, the polarization of the cells are reversed three times a day by inverting the solenoid field. Every three weeks the cell polarization relative to the field is reversed to avoid possible systematic acceptance effects connected with the solenoid field orientation. Using the hadrons azimuthal distributions coming from each cells the following quantity has been built:

$$R_f(\phi_h) = \frac{N^U_{+,f}(\phi_h)}{N^D_{-,f}(\phi_h)} \cdot \frac{N^D_{+,f}(\phi_h)}{N^U_{-,f}(\phi_h)}, \tag{7.1}$$

where $N^{t=(U,D)}_{p=(+,-),f}(\phi_h)$ is the azimuthal distribution of the hadrons coming from the upstream(downstream) cell positively(negatively) polarized for a given solenoid magnetic field orientation in the target (parallel, +, or anti-parallel, −, to the beam).

The number of the detected hadrons as a function of ϕ_h can be factorized in three terms: the luminosity L, the acceptance Acc and the cross section $B \pm P \cdot A$, and can be written as

$$N^t_{p,f}(\phi_h) = L^t \cdot Acc^t_f(\phi_h) \cdot [B(\phi_h) \pm P^t_{p,f} A(\phi_h)]. \tag{7.2}$$

$P^t_{p,f}$ is the absolute value of the product of the measured cell polarization and the calculated dilution factor averaged over the period, $B(\phi_h) = B_0 + B_1 \cos(\phi_h) + B_2 \cos(2\phi_h) + B_3 \sin(\phi_h)$ is the unpolarized part of the cross section (which is addressed in chapter 5) and $A(\phi_h) = A_0 + A_1 \sin(\phi_h) + A_2 \sin(2\phi_h) + A_3 \sin(3\phi_h) + A_4 \cos(\phi_h)$ is the spin dependent part.

In the expression 7.1 the acceptance Acc^t_f, which is different for the two cells, cancels out assuming the stability of the spectrometer through time. The muon fluxes of the upstream and downstream cells are equalized in the analysis so that $R_f(\phi)$ does not depend on the luminosity. For each direction $f = \pm$ of the target magnetic field one can build the following quantity:

$$a_f(\phi_h) = \frac{R_f(\phi_h) - 1}{P^U_{+,f} + P^D_{+,f} + P^U_{-,f} + P^U_{-,f}} \tag{7.3}$$

where, at first order, only the physical azimuthal modulations appear.

Let's consider an example to better explain the reasoning behind the method which leads to build the quantity defined in eq. 7.1 (double ratio in the following, as it is called in the analysis of the transverse spin data, where it is used since quite a long time). Without losing the general meaning, only the $\cos\phi_h$ azimuthal modulation can be considered as it is expected to contribute to the acceptance, to the unpolarized cross-section and to the longitudinally polarized cross-section. Thus the spin independent and the spin dependent part can be written as:

$$B = B_0 + B_1 \cdot \cos\phi_h, \tag{7.4}$$

$$A = A_0 + A_4 \cdot \cos\phi_h. \tag{7.5}$$

By substituting in the first term appearing in the eq. 7.1 the azimuthal dependence of the hadron distributions $N^t_{p,f}$, expressed in eq. 7.2, one has:

$$\frac{L \cdot Acc^U(\phi_h) \cdot \Big[B_0 + B_1 \cdot \cos\phi_h + P^U \cdot (A_0 + A_4 \cdot \cos\phi_h)\Big]}{L \cdot Acc^D(\phi_h) \cdot \Big[B_0 + B_1 \cdot \cos\phi_h - P^D \cdot (A_0 + A_4 \cdot \cos\phi_h)\Big]}, \tag{7.6}$$

where all the quantities are referred to the same period (typically between 8 hours) of data taken with the same cells polarization and same target solenoid magnetic field. Similarly the second term of eq. 7.1, is written as:

$$\frac{L \cdot Acc^D(\phi_h) \cdot \Big[B_0 + B_1 \cdot \cos\phi_h + P^D \cdot (A_0 + A_4 \cdot \cos\phi_h)\Big]}{L \cdot Acc^U(\phi_h) \cdot \Big[B_0 + B_1 \cdot \cos\phi_h - P^U \cdot (A_0 + A_4 \cdot \cos\phi_h)\Big]}, \tag{7.7}$$

In the double ratio the luminosities L cancel out, and assuming the stability of the spectrometer over the analyzed periods of data taking, it is reasonable to assume

that the ratio $\frac{Acc^U(\phi_h)}{Acc^D(\phi_h)}$ is the same in eq. 7.6 and in eq. 7.7. Thus also the acceptance terms cancel out and the double ratio can be written as:

$$\frac{C_+^U C_+^D}{C_-^U C_-^D} \cdot \frac{(1+\alpha_+^U \cdot \cos\phi_h)\cdot(1+\alpha_+^D \cdot \cos\phi_h)}{(1-\alpha_-^U \cdot \cos\phi_h)\cdot(1-\alpha_-^D \cdot \cos\phi_h)}, \tag{7.8}$$

where $C_\pm^{U,D} = B_0 \pm P^{U,D} A_0$ and $\alpha_\pm^{U,D} = \frac{B_1 \pm P^{U,D} A_4}{C_\pm^{U,D}}$.

Let's assume that the spin dependent part of the cross section A_0 and A_4 as well as B_1 are much smaller than the the spin independent part B_0, allowing an expansion on all the terms like A_0/B_0, A_4/B_0 and B_1/B_0. By keeping only the terms up to the first order the double ratio becomes:

$$\begin{aligned} R_f(\phi_h) &= K \cdot \Big[1 + (\alpha_+^U + \alpha_+^D + \alpha_-^U + \alpha_-^D)\cdot\cos\phi_h\Big] \\ &= K \cdot \Big[1 + (\frac{B_1}{B_0} + P^U\frac{A_4}{B_0} + \frac{B_1}{B_0} + P^D\frac{A_4}{B_0} - \frac{B_1}{B_0} + P^U\frac{A_4}{B_0} - \frac{B_1}{B_0} + P^D\frac{A_4}{B_0})\cdot\cos\phi_h\Big] \\ &= K \cdot \Big[1 + \frac{A_4}{B_0}\cdot P_{SUM}\Big], \end{aligned} \tag{7.9}$$

where P_{SUM} is the sum of the absolute values of the target cell polarization times dilution factor and A_4/B_0 is the azimuthal asymmetry given by the $\cos\phi_h$ modulation proportional to the longitudinal target polarization.

The ϕ_h independent term K of eq. 7.9 can be written as:

$$\begin{aligned} K &= \frac{C_+^U C_+^D}{C_-^U C_-^D} \\ &= \frac{B_0^2\cdot(1+P^U\frac{A_0}{B_0})\cdot(1+P^D\frac{A_0}{B_0})}{B_0^2\cdot(1-P^U\frac{A_0}{B_0})\cdot(1-P^D\frac{A_0}{B_0})} \\ &= \simeq 1 + \frac{A_0}{B_0}\cdot P_{SUM}, \end{aligned} \tag{7.10}$$

where A_0/B_0 is the asymmetry given by the doubly longitudinally polarized cross section.

The quantity shown in eq. 7.3 has been extracted binning alternatively the data in the kinematical variables x, z and P_T^h. The corresponding amplitudes of the azimuthal modulations have been simultaneously extracted by a fit performed in each bin.

7.2 Analysis

7.2.1 Data selection

The data used are the data collected in $2002-2004$ with the longitudinally polarized deuterium target. Starting from the SIDIS kinematical selection, described in section 4.2, further cuts have been applied: $z < 0.9$ to exclude the region of exclusive hadronic production and $P_T^h < 1$ GeV/c to cut out pQCD effects. The tracks originating from the primary vertex have been further identified as hadrons using

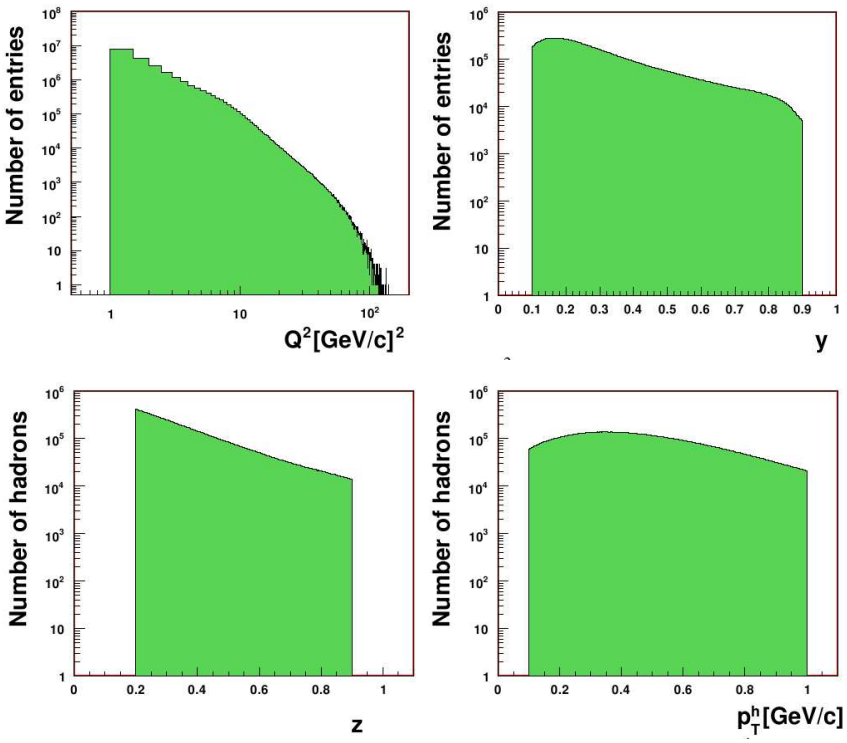

Figure 7.1: Distribution after the analysis cuts, of the events (top plot) for Q^2 (right) and y (left) and of the hadrons (lower plot) for z (left) and P_T^h (right).

the information from the two hadronic calorimeters HCAL1 and HCAL2. A hadron is selected if its track hits one of the calorimeters. The associated cluster must have an energy larger than 5 GeV in HCAL1 or larger than 7 GeV in HCAL2. Then the compatibilities between the position of the cluster and the track, and between the energy of the cluster and the momentum of the track, are checked. For historical reasons the selection criteria used for this analysis are slightly different from the standard one, described in section 4.2 and the main difference concerns the use of the hadronic calorimeters. In section 7.4 it is shown that the results are essentially the same applying the standard selection. The distributions of the events and hadrons, after all the cuts, are shown in fig. 7.1.

7.2.2 Asymmetries extraction

For each year and solenoid field direction the azimuthal distributions of the hadrons have been built summing over all events coming from the same cell, e.g. upstream cells polarized in the same direction of the beam momentum. The cell the event belongs to is determined by the coordinates of the reconstructed interaction vertex. The distributions have been extracted separately for positive and negative hadrons and for each kinematical bin. The distributions obtained for the four cells combinations with the same solenoid field direction have been used to build the double ratio 7.1. The quantities $a_f(\phi_h)$ of eq. 7.3 have been then calculated using a dilution

factor of 0.35 and the measured mean cell polarization. The weighted sum

$$a(\phi_h) = (a_+(\phi_h) \oplus a_-(\phi_h))_{2002} \oplus (a_+(\phi_h) \oplus a_-(\phi_h))_{2003} \oplus (a_+(\phi_h) \oplus a_-(\phi_h))_{2004} \quad (7.11)$$

has been calculated in each kinematical bin separately for positive and negative hadrons and it has been fitted with the function:

$$f(\phi_h) = a_{const} + a_{\sin\phi_h} \cdot \sin\phi_h + a_{\sin 2\phi_h} \cdot \sin 2\phi_h + a_{\sin 3\phi_h} \cdot \sin 3\phi_h + a_{\cos\phi_h} \cdot \cos\phi_h, \quad (7.12)$$

with four free parameters.

7.3 Results

The results for the amplitudes of the azimuthal modulations $a_{\sin\phi_h}$, $a_{\sin 2\phi_h}$, $a_{\sin 3\phi_h}$ and $a_{\cos\phi_h}$ are shown in figures 7.2-7.5. Each amplitude is shown as function of x, z and P_T^h and the results for positive and negative hadrons are superimposed on the same plot. Only the statistical errors are shown as the systematic uncertainties are estimated to be much smaller then the statistical ones (see sec. 7.4). The general picture shows that these asymmetries are small and compatible with zero within the statistical accuracy.

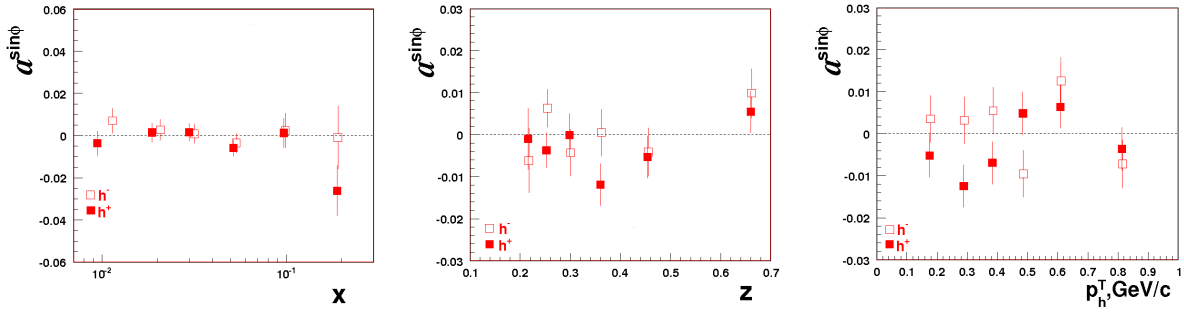

(a) **(b)** **(c)**

Figure 7.2: Amplitudes of $\sin\phi_h$ as function of x, **(a)**, z, **(b)**, and P_T^h, **(c)**. Results from positive (full squares) and negative (open squares) are superimposed.

7.4 Systematic studies

The results of the fits performed for each year of data taking have been also extracted and the χ^2 distribution has been checked to be compatible with the one expected from a 16 degrees of freedom theoretical χ^2 distribution. The compatibility between the results extracted from each year of data taking has also been checked.

From the data, a small difference was found between the $\sin\phi_h$ asymmetries extracted from the data taken with a positive or negative direction solenoid field direction, a_+ and a_- respectively. This difference is due to a dependence of the acceptance on the target magnetic field which results in an azimuthal modulation

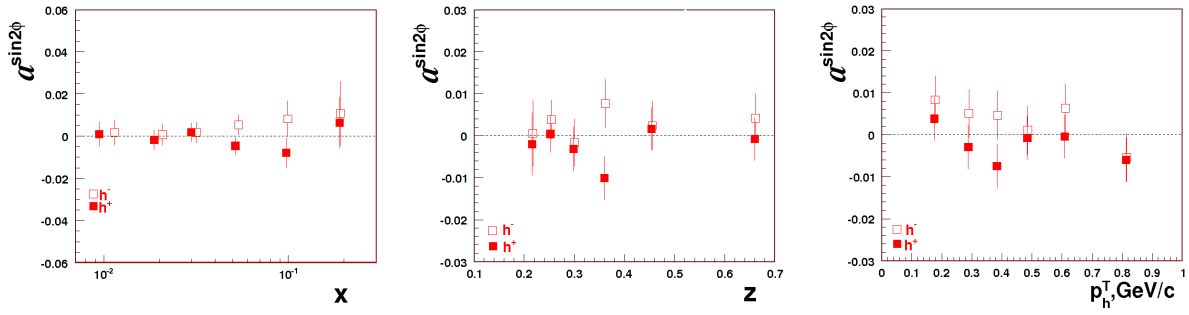

(a) **(b)** **(c)**

Figure 7.3: Amplitudes of $\sin 2\phi_h$ as function of x, **(a)**, z, **(b)**, and P_T^h, **(c)**. Results from positive (full squares) and negative (open squares) are superimposed.

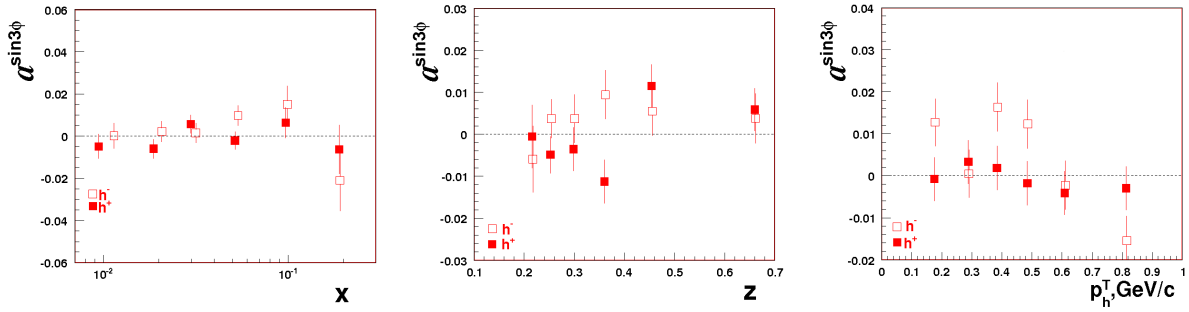

(a) **(b)** **(c)**

Figure 7.4: Amplitudes of $\sin 3\phi_h$ as function of x, **(a)**, z, **(b)**, and P_T^h, **(c)**. Results from positive (full squares) and negative (open squares) are superimposed.

with an amplitude that changes sign as the solenoid field is reversed. However, it has been checked by Monte Carlo simulations that this term cancels out in the weighted sum $a_+ \oplus a_-$.

7.4.1 Consistency with $A_{1,d}^h(x)$ COMPASS results

The extracted parameter a_{const} divided by the average muon polarisation and the virtual-photon depolarisation factor

$$D_0 \simeq |P_\mu| \frac{y\,(2-y)}{2\,(1-y)+y^2}$$

has been calculated as a function of x. By definition $a_{const}(x)/D_0$ is the asymmetry $A_{1,d}^h(x)$ already measured by COMPASS [86], with a completely different analysis.

The comparison between $a_{const}(x)/D_0$ and the results for $A_{1,d}^h(x)$ proves the stability of the apparatus and the reliability of the method. The results obtained with different analysis are well compatible as it is shown in fig 7.6.

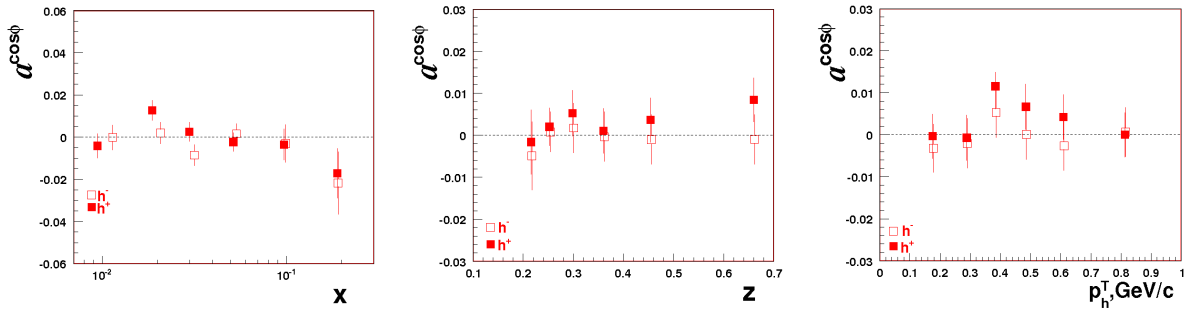

(a) (b) (c)

Figure 7.5: Amplitudes of $\cos\phi_h$ as function of x, **(a)**, z, **(b)**, and P_T^h, **(c)**. Results from positive (full squares) and negative (open squares) are superimposed.

7.4.2 Time stability of the results

The stability of the results extracted within the year has been studied.

The data collected during each year have been divided in 2 different configurations: with parallel (configuration 1) and anti-parallel (configuration 2) upstream cell polarization and solenoid field. For each configuration, different double ratios are built using the data coming from the different "slices". To have enough statistics the azimuthal distributions have been evaluated integrating over all the kinematical variables and the results have been extracted fitting the quantity of eq. 7.3 using the function given in eq. 7.12.

As an example the results for the year 2004 are shown in fig. 7.7 for positive hadrons. In the abscissa the parameters extracted from the fit function are plotted for each slice of configuration 2, on the left, and of configuration 1, on the right.

To check the compatibility for the 5 parameters the quantities ("pulls")

$$\frac{\alpha_i - \frac{\sum_i \alpha_i}{n}}{\sigma_i} \tag{7.13}$$

have been calculated. α_i is the parameter extracted for each subsample i and σ_i is the corresponding statistical error. In this formula the statistical error of the mean has been neglected since the number of subsamples n is around large. The pulls for the amplitudes of the azimuthal modulations are shown in fig. 7.8. They all have mean values compatible with zero as expected as no evidence of any physical azimuthal modulations has been seen from the quantities 7.3 integrated over all the kinematic range. Also, the RMS values are all compatible with 1. No evidence of a systematic effect is given by this test.

7.4.3 Consistency checks

As a further check the amplitudes of the azimuthal modulations as functions of x, z and P_T^h have been obtained with the hadron selection described in section 4.2.

The comparison between the present results (black points) and the ones extracted using the standard cuts (red points) is shown for positive hadrons in fig. 7.9. As can

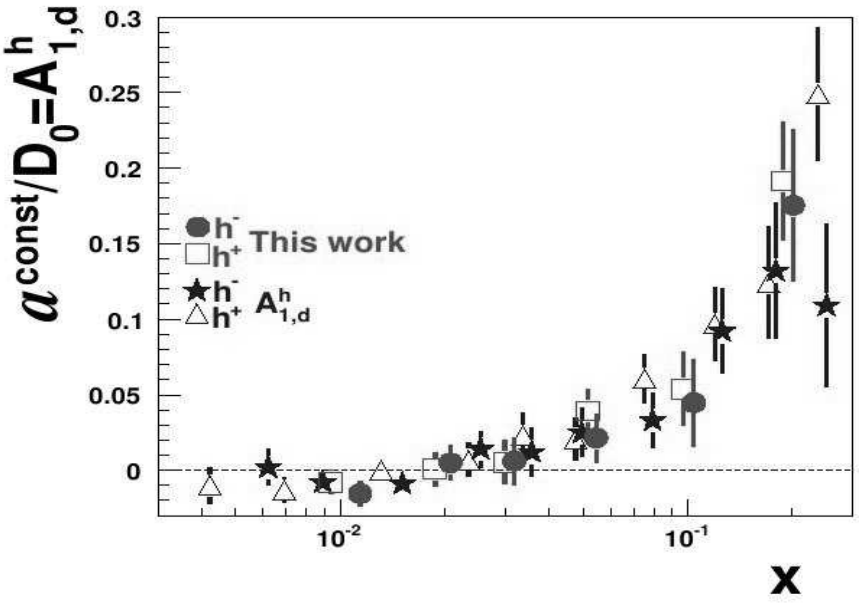

Figure 7.6: Comparison between $a_{const}(x)/D_0$ and $A^h_{1,d}(x)$ from [86] for positive hadrons (open squares and open triangles) and negative hadrons (full circles and full stars).

be seen the agreement is very good.

7.5 Discussion of the results

The $\sin\phi_h$ amplitude is a combined effect of the $F_{UL}^{\sin\phi_h}$ structure functions and also from the Collins and Sivers asymmetries ($F_{UT}^{\sin\phi_h+\phi_S}$ and $F_{UT}^{\sin\phi_h-\phi_S}$), already measured at COMPASS [26] and found to be compatible zero on deuteron. In fig. 7.10 the comparison of the results for $a_{\sin\phi_h}$ and the ones obtained by the HERMES Collaboration [87] is shown. While the COMPASS results show a small signal, compatible with zero, HERMES measured a signal different from zero, negative for both positive and negative hadrons, and increasing with x. In the comparison, one has to take into account the different kinematics of the experiments. In particular, in the high x region of COMPASS, the mean value of Q^2 is roughly three times bigger for COMPASS than for HERMES, thus higher twist effects should be smaller at the COMPASS energies.

The amplitude of the $\sin 2\phi_h$ modulation is given by the leading twist contribution coming from the $F_{UL}^{\sin 2\phi_h}$ structure function. The asymmetries are small and compatible with zero within the statistical errors. However the points obtained from the positive hadrons are systematically lower than the ones obtained from the negative hadrons.

A small difference between the results obtained for positive and negative hadrons is expected in some model calculations [88], but the predicted asymmetries are in

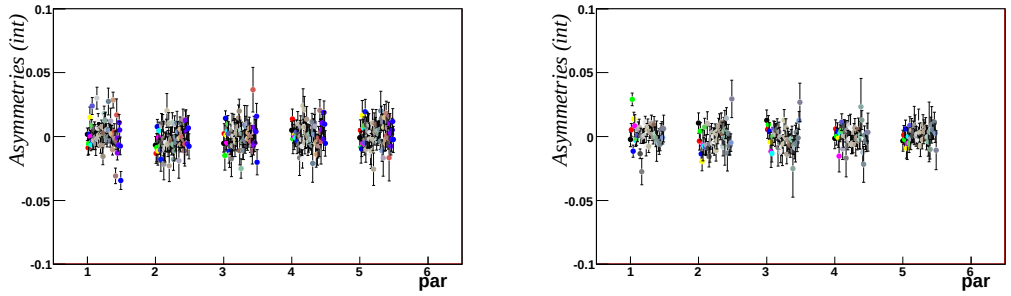

Figure 7.7: Results extracted using slices of data taken in 2004 (positive hadrons). The 5 bunches of points correspond to the 5 parameters in the function 7.12. The points of each bunch correspond to the slices in which the data coming from a configuration have been divided into (configuration 2 and 1 are, respectively, on the left and on the right). The number of slices is 30 to 50.

any case very small, of the order of 10^{-3}, and a very precise measurement is needed to confirm the effect.

The results obtained by HERMES [87] are compatible with zero with no particular difference between the asymmetries extracted for positive and negative hadrons.

Slightly negative amplitudes of the $\sin 2\phi_h$ modulation in SIDIS have been measured at CLAS [89], both from positive and negative pions. These measurements have been performed using a $5,7$ GeV electron beam on the longitudinally polarized proton target, covering an x region which is complementary to the smaller x region explored by COMPASS.

The amplitudes of the $\cos\phi_h$ azimuthal modulation for a longitudinally polarised target have been measured for the first time. The amplitudes turned out to be small and compatible with zero for both positive and negative hadrons as functions of x, z and P_T^h. A possible interpretation is given by the doubly longitudinally polarized Cahn effect [34], where the expected magnitude of the asymmetries for deuteron is of the order 10^{-2}, i.e. very difficult to be measured.

Summarizing, the results presented here and published in ref. [90], complete the measurements of the amplitudes of all the SIDIS azimuthal asymmetries for the deuteron target (unpolarized, longitudinally polarized and transversely polarized) and a phenomenological analysis of all the different contributions of the TMD PDFs can be done. In the next future, the same amplitudes from the data collected in 2006 (with ^{6}LiD as target material) and in 2007 with the longitudinally polarized NH_3 target will be measured, giving more information on the higher twist effects and on the TMD PDFs. Further data will be collected in 2011, with the longitudinally polarized NH_3 target. These new measurements, together with the measurements with the transversely polarized NH_3 target, will give new important input for the understanding of the nucleon structure.

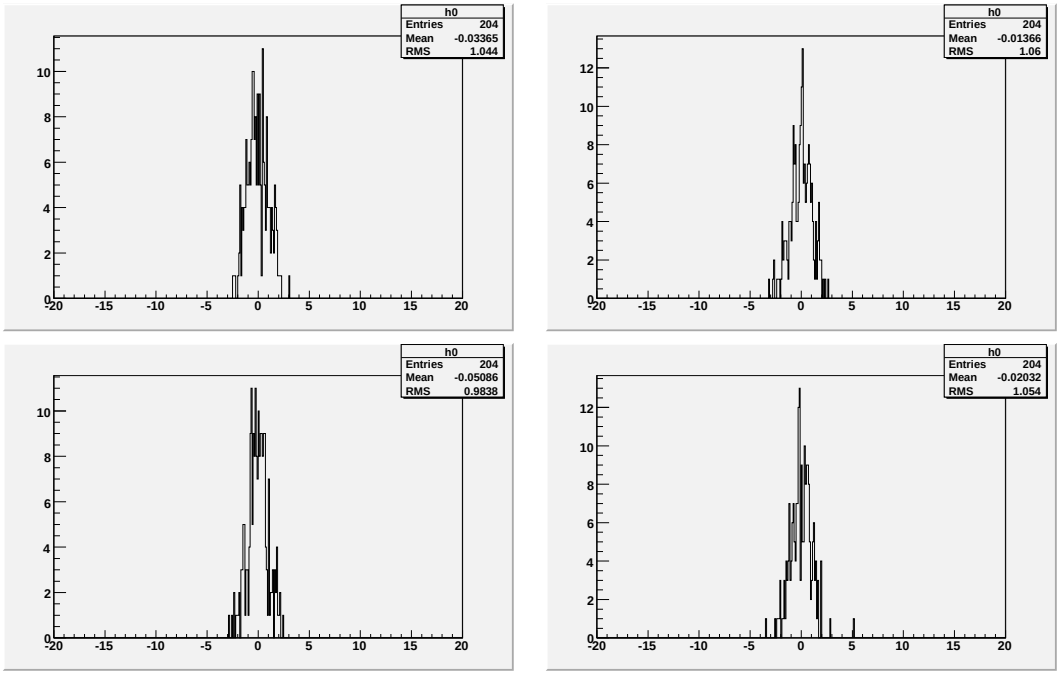

Figure 7.8: Pulls calculated as in eq. 7.13 using all the results, for the amplitudes of the azimuthal modulations in 7.12, extracted from the 3 years of data taking (positive hadrons).

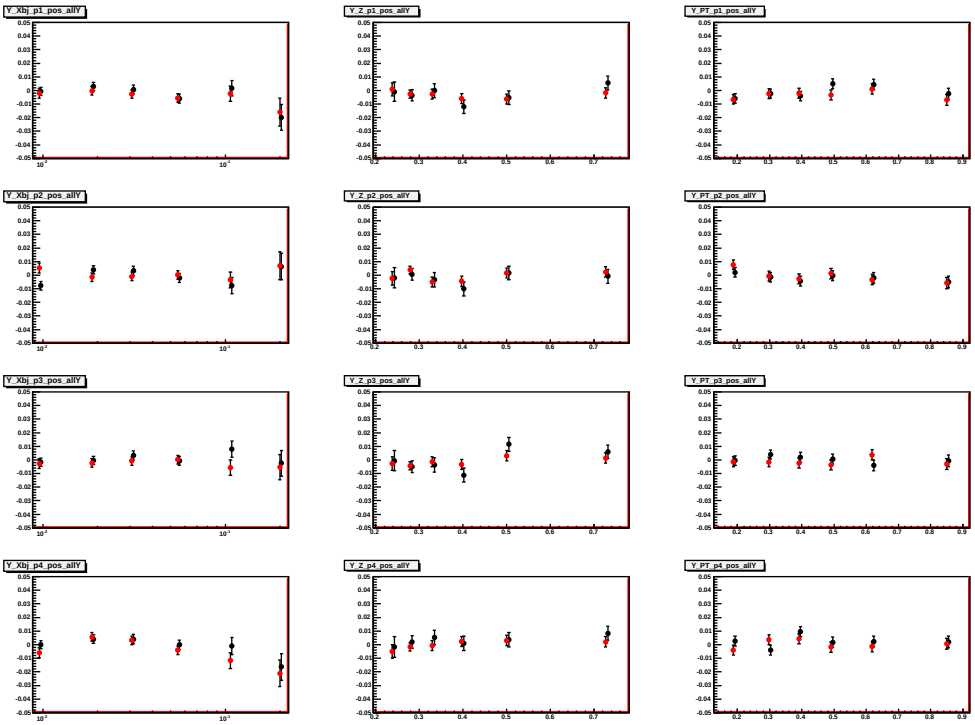

Figure 7.9: Comparison between the final results of this analysis shown in sec. 7.3 (black points) and the ones obtained using the hadron selection of section 4.2 (red points) for positive hadrons. The $a_{\sin\phi_h}$ amplitudes are in the first row, $a_{\sin 2\phi_h}$ in the second, $a_{\sin 3\phi_h}$ in the third and $a_{\cos\phi_h}$ in the last row. The amplitudes are shown as functions of x (left column), z(central column) and P_T^h(right column).

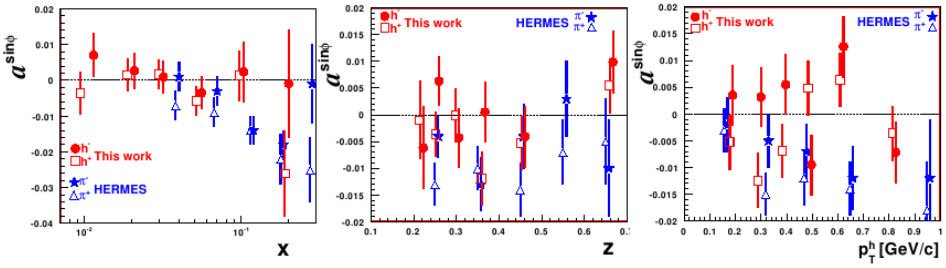

Figure 7.10: Dependence of the amplitude $a_{\sin\phi_h}$ on the kinematical variables (red points) and the ones measured by HERMES [87] (blue points).

Chapter 8

Conclusions

8.1 Conclusions

The measurement of the azimuthal asymmetries in SIDIS off unpolarized and longitudinally polarized targets, together with the transverse spin asymmetries allows to extract information on the inner structure of the nucleons and in particular on the effects given by the intrinsic transverse momentum of the quarks, which is now thought to have a main role in the description of the nucleon dynamics. Actually SIDIS is today the process which allows the most direct access to this information since the amplitudes of the azimuthal modulations are, in the parton model, the convolution of the (Transverse Momentum Dependent) PDFs with the FFs.

Results for the transverse spin asymmetries have already been produced by the COMPASS, HERMES and JLab E06-010 Collaborations and are not discussed here.

In this thesis the results for the azimuthal asymmetries in SIDIS on the unpolarized and longitudinally polarized target are presented. They have been obtained using the COMPASS data collected until 2004 with the ^{6}LiD target. They are the first measurements of this kind in the COMPASS experiment, and a great care has been devoted to the evaluation of the systematic effects since the expected signals are small, a few percent, in most of the cases. In particular the measurement with the unpolarized target asymmetries require a very good knowledge of the effects introduced by the acceptance and efficiency of the experimental apparatus, since the measured azimuthal distributions have to be corrected for these effects by means of Monte Carlo simulations. Thus this measurement is more difficult than the measurement of the spin azimuthal asymmetries, for which the stability of the apparatus is an important point.

For the longitudinal spin asymmetries the amplitudes of the $\sin\phi_h$, the $\sin 2\phi_h$, the $\sin 3\phi_h$ and, for the first time, the $\cos\phi_h$ modulation, have been measured. The values turned out to be essentially compatible with zero within the statistical accuracy, which is at the level of a few percent, for both positive and negative hadrons. This is true also for the $\sin\phi_h$ amplitude, measured to be different from zero by the HERMES experiment, suggesting that the higher twist effects seem to be less relevant at the COMPASS energy. In the next future, results will be produced by the data collected, at the same μ beam energy, in 2006 with the longitudinal polarized ^{6}LiD target. Also, the same amplitudes will be measured using the 2007

data collected with the longitudinally polarized NH_3 (polarized protons) target and using the data which will be collected in 2011. These new measurements will allow to single out the measurable effects in high energy SIDIS.

With the unpolarized ^{6}LiD target the amplitudes of the $cos\phi_h$, $cos2\phi_h$ and $sin\phi_h$ in SIDIS have been measured separately for positive and negative hadrons. A somewhat unexpected and interesting result is different from zero signal measured for the unpolarized nucleon $\sin\phi_h$ asymmetries, obtained for the positive hadrons. This asymmetry is given by higher twist effects and thus expected to be negligible at the COMPASS energies, on the contrary it seems to have the same strength and the sign of the one measured at CLAS and HERMES, at lower energies.

The results obtained for the unpolarized nucleon asymmetries for the $\cos\phi_h$ and $\cos 2\phi_h$ modulations, are also very interesting. Both the size and the dependence from the kinematical variables are, in general, in good agreement with the theoretical predictions, but there are also unexpected results. For example, the asymmetries are different for positive and negative hadrons, and the z dependence of the $\cos\phi_h$ asymmetry (constant until ~ 0.5, and then rapidly increasing with z) seems to be unexpected. Also the preliminary result for the quark intrinsic transverse momentum extracted from the measured $cos\phi_h$ amplitude is smaller than the values which can be found in literature extracted from the EMC and HERMES data.

The results for the $cos2\phi_h$ amplitudes, which show a clear dependence from the hadron charge, can be a signature of the Boer-Mulders function in SIDIS and show a P_T^h trend which seems to be difficult to be reproduced. Those measurements have to be analysed together with the results for the $cos\phi_h$ amplitudes to take into account also a possible quark flavour dependence of the intrinsic transverse momentum.

The measurements of the unpolarized nucleon asymmetries from the data collected in 2006, with the polarized ^{6}LiD target, are just started and a first analysis looks promising. The larger acceptance of the apparatus should allow to extract these asymmetries in a broader kinematical range and thus to reduce the systematic uncertainties related to the acceptance corrections.

In the future the measurement of these asymmetries on a liquid hydrogen target is foreseen at COMPASS-2, allowing to perform a combined analysis of the proton and deuteron amplitudes at high energy. Complementary information on the role of transverse momentum will come from the Drell-Yann measurements at COMPASS-2.

In conclusion, the results presented in this thesis are an important part of the COMPASS contribution to the study of the nucleon structure, completing the measurements of the transverse spin asymmetries. Already by now the set of measurements is large enough to allow for a quantitative study of the contributions of the TMD PDFs to the SIDIS cross section.

Bibliography

[1] F.Halzen, A.D.Martin, "Quarks and leptons: an introductory course in modern particle physics", NewYork, NY: Wiley, 1984.

[2] A.Bacchetta, U.D'Alesio, M.Diehl and C.A. Miller, Phys. Rev. **D70** (2004) 117504.

[3] M. Anselmino, A. Efremov, E. Leader, Phys. Rep. 261, 1 (1995).

[4] E. Leader and E. Predazzi, "An Introduction to Gauge Theories and the New Physics", Cambridge University Press (1985).

[5] A.Bacchetta, M. Diehl, K.Goeke, A.Metz, P.Mulders and M.Schlegel JHEP 0702 (2007)

[6] A.Kotzinian, Nucl. Phys. **B441**, (1995) 234

[7] R.P.Feynman, Photon-Hadron interactions, Benjamin, 1972

[8] J.P.Ralston and D.E.Soper, Nucl. Phys. **B152** (1979) 109

[9] X. Artru and M. Mekhfi, Z. Phys. **C45**, (1990) 669.

[10] R. L. Jaffe and X. D. Ji, Phys. Rev. Lett. **67**, (1991) 552.

[11] R.L. Jaffe, hep-ph/9602236.

[12] P.J.Mulders and R.D.Tangerman, Nucl. Phys. **B461**, (1996) 197

[13] D.Boer and P.J.Mulders, Phys.Rev.**D57**, (1998) 5780

[14] S.J.Brodsky, D.S.Hwang, I.Schmidt, Phys. Lett. **B530** (2002) 99.

[15] D.Boer, Phys.Rev.**D60**, (1999) 014012

[16] J.C.Collins, Phys. Lett. **B536**, (2002) 43

[17] D.W.Sivers, Phys.Rev.**D41**, (1990) 83

[18] A.Bacchetta, A.Scaefer and J.-J.Yang Phys. Lett. **B578** (2004) 109.

[19] A.Bacchetta, F.Conti and M.Radici Phys. Rev. **D78** (2008) 074010.

[20] J.R.Ellis, D.S.Hwang and A.Kotzinian Phys. Rev. **D80** (2009) 074033.

[21] J.C.Collins, Nucl. Phys. **B396**, (1993) 161

[22] H.Avakian *et al.* Phys. Rev. **D78**, (2008) 114024

[23] V.Barone, T.Calarco and A.Drago Phys. Lett. **B390** (1997) 287.

[24] X.Artru, J.Czyzewski, H.Yabuki, Z. Phys. C**73** (1997) 527

[25] A.Airapetian *et al.*, (The HERMES Collaboration) Phys. Rev. .Lett. **94** (2005) 012002.

[26] V.Y.Alexakhin *et al.*, (The COMPASS Collaboration) Phys. Rev. .Lett. **94** (2005) 202002.

[27] M.G.Alekseev *et al.*, (The COMPASS Collaboration) Phys. Lett. **B692** (2010) 240.

[28] X.-d.Ji, J.-P.Ma and F.Yuan, Phys. Lett. **B597** (2004) 299.

[29] J.C.Collins, T.C.Rogers and A.M.Stasto, Phys. Rev. **D77** (2008) 085009.

[30] V.Barone, F.Bradamante and A.Martin, Prog. Part. Nucl. Phys. **65** (2010) 267.

[31] H.Georgi, H.D.Politzer, Phys. Rev .Lett. **40** (1978) 3

[32] R.N. Cahn, Phys. Lett. B **78** (1978) 269.; Phys.Rev.D **40** (1989) 3107

[33] A.Konig, P.Kroll, Z. Phys. **C16** (1982) 89

[34] M.Anselmino, A.Efremov, A.Kotzinian, B.Parsamyan, Phys. Rev. **D74** (2006) 074015

[35] EMC Collaboration (J.J.Aubert et al.) Phys. Lett. **B95** (1980) 306

[36] EMC Collaboration (J.J.Aubert et al.) Phys. Lett. **B130** (1983) 118

[37] EMC Collaboration (M.Arneodo et al.) Z. Phys. **C34** (1987) 277

[38] E665 Collaboration, M.R.Adams *et. al* Phys. Rev. **D48** (1993) 5057.

[39] ZEUS Collaboration, J. Breitweg *et al.*, Phys. Lett. **B481** (2000) 199.

[40] EMC Collaboration (J.Ashman et al.) Z. Phys. **C52** (1991) 361

[41] V.Barone, A.Prokudin, B.-Q.Ma, Phys. Rev. **D78** (2008) 045022

[42] M.Anselmino *et al.*, Phys. Rev. **D72**, (2005) 094007

[43] M.Anselmino *et al.*, Phys. Rev. **D75**, (2007) 054032

[44] B.Zhang, Z.Lu, B.-Q.Ma and I.Schmidt, Phys. Rev. **D78**, (2008) 034035

[45] L.P.Gamberg, G.R.Goldstein and M.Schlegel, Phys. Rev. **D77**, (2008) 094016

[46] H.Avakian *et al.* Phys. Rev. **D77**, (2008) 014023

[47] A.Airapetian *et al.* (The HERMES Collaboration) Phys. Lett. **B622** (2005) 14

[48] N. W. Schellingerhout *et al.*, "Nucleon polarization in three-body models of polarized ^{6}Li", Phys. Rev. C**48** (1993) 2714.

[49] A. Abragam, The Principles of Nuclear Magnetism, The Clarendon Press, Oxford, 1961.

[50] L. Schmitt *et al.*, IEEE Trans. Nucl. Sci. **51** (439) 2004.

[51] P. Abbon *et al.* [COMPASS Collaboration], Nucl. Instrum. Meth. A **577**, 455 (2007) [arXiv:hep-ex/0703049].

[52] http://coral.web.cern.ch/coral/.

[53] R. Brun and F. Rademakers, Nucl. Instrum. Meth. A **389** (1997) 81. See also http://root.cern.ch/.

[54] http://ges.home.cern.ch/ges/phast/index.html

[55] G.Sbrizzai Diploma thesis (*in italian*) http://wwwcompass.cern.ch/compass/publications/theses/

[56] GEANT - detector description and simulation tool, CERN Program Library Long Writeup W5013, http://wwwasdoc.web.cern.ch/wwwasdoc/geant_html3/geantall.html

[57] G. Ingelmann, et al., Comput. Phys. Commun. 101 (1997) 108.

[58] G. Ingelmann, et al., Comput. Phys. Commun. 101 (1997) 135.

[59] T. Sjostrand, et al., Comput. Phys. Commun. 135 (2001) 238.

[60] I. Akushevic, et al., RADGEN 1.0, hep-ph/9906408 (1999).

[61] W.Kaefer on behalf of the COMPASS collaboration, TRANSVERSITY 2008, proceedings, arXiv:0808.0114v1 [hep-ex]

[62] H. L. Lai, J. Huston, S. Kuhlmann, J. Morfin, F. Olness, J. F. Owens, J. Pumplin and W. K. Tung Eur.Phys.J. C**12** (2000) 375-392

[63] A.D. Martin, W.J. Stirling, R.S. Thorne and G. Watt, Eur.Phys.J. C**63** (2009) 189-285

[64] Andrei Afanasev, presentation at COMPASS Analisys Meeting (2010) http://wwwcompass.cern.ch/compass/software/analysis/transparencies/2010/am_100907/ afanasev_compass_10.ppt

[65] A.Afanasev, private comunication.

[66] G.Sbrizzai, presentation at the COMPASS Analysis Meeting (May 2010) http://wwwcompass.cern.ch/compass/software/analysis/transparencies/2010/am_100506/sbrizzai_100506.pdf

[67] Giulio Sbrizzai for the COMPASS Collaboration
To appear in the proceedings of the SPIN 2010 conference,
Julich, Germany, September 27th- October 2nd 2010.
arXiv:1012.4910 [hep-ex]

[68] HERMES collaboration, (Francesca Giordano, Rebecca Lamb). To appear in the proceedings of the SPIN 2010 conference, Julich, Germany, September 27th-October 2nd 2010.

[69] A.Airapetian *et al.* (The HERMES collaboration) Phys. Rev. Lett. **84**, (2000) 4047

[70] A.Airapetian *et al.* (The HERMES collaboration), Phys. Lett. **B648** (2007) 164.

[71] H.Avakian *et al.* (The CLAS Collaboration) Phys. Rev. **D69**, (2004) 112004

[72] M.Osipenko *et al.* (The CLAS Collaboration) Phys. Rev. **D80**, (2009) 032004

[73] E.L.Berger, ANL-HEP-CP-87-45, Apr 1987

[74] Anton Jgoun, for the HERMES collaboration, arXiv:hep-ex/0107003

[75] M. Anselmino et al., Phys. Rev. **D71** (2005) 074006.

[76] M. Anselmino et al., Eur. Phys. J. A **31** (2007) 373.

[77] P.Schweitzer, T.Teckentrup and A.Metz, Phys. Rev. **D81**, (2010) 094019

[78] J.C.Collins, A.V.Efremov, K.Goeke, S. Menzel, A. Metz and P.Schweitzer, Phys. Rev. **D73**, (2006) 014021.

[79] B.Pasquini and F.Yuan, Phys. Rev. **D81**, (2010) 114013.

[80] H. Avakian, A.V.Efremov, P.Schweitzer and F.Yuan, Phys. Rev. **D81**, (2010) 074035.

[81] J.F.Rajotte for The COMPASS Collaboration arXiv:hep-ex/1008.5125v1
To appear in the proceedings of SPIN-Praha-2010

[82] F.Yuan, Phys. Lett. **B575**, (2003) 45

[83] B.Pasquini, M.Pincetti and S.Boffi, Phys.Rev. **D72** (2005) 0940007

[84] M.Burkardt and B.Hannafious Phys. Lett. **B658**, (2008) 130

[85] V.Barone, S.Melis and A.Prokudin, Phys. Rev. **D81** (2010) 114026.

[86] M.Alekseev *et al.* (The COMPASS Collaboration), Phys. Lett. **B660** (2008) 458.

[87] HERMES Collaboration (A. Airapetian et al.), Phys. Lett. B**562** (2003) 182

[88] H.Avakian, A.V.Efremov, K. Goeke, A. Metz, P. Schweitzer and T.Teckentrup, Phys.Rev. **D77** (2008) 014023

[89] H.Avakian *et al.* (The CLAS Collaboration) Phys. Rev. Lett. **105** (2010) 262002

[90] M.G.Alekseev *et al.* (The COMPASS Collaboration), arXiv:1007.1562 [hep-ex] accepted for publication in Eur. Phys. J. C.

Acknowledgments

I would like to thank prof. Anna Martin my PhD tutor and supervisor of this thesis, who has always followed my activity in these years and who has taught me a lot, thanks for all the discussions and explanations and for her enthusiasm on the subject.

Thanks to all the colleagues of the Trieste COMPASS group, in particular to Franco Bradamante, who always supported my work, to Andrea Bressan, for his help and support during the analysis and to prof. Paolo Schiavon for his precious advice.

Thanks to Renato Birsa and Benigno Gobbo for being always ready to solve any computing problem. Thanks to all the people with whom I share the office: Vinicio Duic, Carmine Elia, Stefano Levorato, Giulia Pesaro and Federica Sozzi.

Thanks to all COMPASS people with whom I have worked along these years, in particular to Eva-Maria Kabuss, Ewa Rondio, Jean-Froncoise Rajotte and Nour Makke. Special thanks to the Dubna group, in particular to Anatoly Efremov and to Yura Ivanshin for thier collaboration.

I would like to thank for their help and fruitful discussions Alessandro Bacchetta, Vincenzo Barone, Maria-Elena Boglione, Stefano Melis and Alexei Prokudin.

I also would like to thank the HERMES Collaboration for providing me the numerical results of their measured asymmetries.

I would like also to thanks Francesca Giordano and Mher Aghasyan for the many fruitful discussions.

Thanks to Harut Avakian for having accepted to referee this thesis.